HBT CHARACTERIZATION AND MODELING FOR NONLINEAR MICROWAVE CIRCUIT DESIGN

ZHOU TIANSHU

(M.Eng., SOUTHEAST UNIVERSITY, P.R. CHINA)

A THESIS SUBMITTED

FOR THE DEGREE OF DOCTOR OF PHILOSOPHY

DEPARTMENT OF ELECTRICAL AND COMPUTER ENGINEERING

NATIONAL UNIVERSITY OF SINGAPORE

2003

ACKNOWLEDGEMENTS

I would like to express my most sincere gratitude to my supervisors, Professor Kooi Pang Shyan, Assistant Professor Ooi Ban Leong and Dr. Lin Fu Jiang in the Department of Electrical and Computer Engineering of the National University of Singapore, for their invaluable guidance, encouragement and very strong support through this difficult journey.

My deep appreciation is also given to Professor Leong Mook Seng, Professor Xu Qun Ji, Mrs. Ma Jing Yi, Mr. Chen Bo, Mr. Pan Shu Jun, Mr. Wu Bin and Mr. Hui So Chi for their helpful suggestions and discussions.

The encouragement I received from my friends, colleagues and lab technicians during my postgraduate program should not be left unmentioned. Without them, this dissertation could not have been successfully completed. For this, I extend my great appreciation to all of them.

I take this opportunity to express my deepest thanks to my beloved parents, wife and my younger sister for their incessant encouragement, support and endless love. Also, I would like to thank my lovely son Ziyao for the great happiness he brings to me. Frankly speaking, I owe them too much in these years and I hope that I can make all up to all of them in the near future.

Last but not least, I gratefully acknowledge the National University of Singapore for the financial support in the form of a research scholarship.

TABLE OF CONTENTS

CHAPTER 5

IMPROVED HBT LARGE-SIGNAL MODELING METHOD 86

SUMMARY

Today, one of the important technical phenomena is the rapid advance of wireless communications systems, and the sudden and great interest in microwave and radio-frequency (RF) technology. Heterojunction bipolar transistors (HBTs) are becoming the very good candidates for microwave and RF integrated circuits. The device models of HBTs implemented in computer-aided design tools, which can include small-signal model and large-signal model, are extremely important for successful design and fabrication of relevant microwave and RF integrated circuits. In this dissertation, the research project mainly involves a comprehensive investigation on the characterization and modeling of various HBTs. The objective of this research project is to develop accurate and practical HBT small-signal and large-signal models for the successful design of microwave and RF integrated circuits.

Traditionally, analytical and optimization methods are used in the HBT small-signal modeling, which usually require complex analyses or suffer from failure of convergence. In this dissertation, three new methods for the parameter extraction of HBT small-signal models are developed. The strong correlation between extrinsic and intrinsic model elements is identified and a completely new equation is derived to further reduce the number of extrinsic model parameters for optimization. In this way, the efficiency and accuracy for model parameter extraction can be improved significantly. For the first time, the HBT transistor is characterized by describing the S-parameters with a set of complex exponentials using the Generalized Pencil-of-Function (GPOF) method. The reliable initial values of some extrinsic model elements can be determined from this set of complex exponentials. This new approach can yield a good fit between measured and simulated S-parameters. A novel distributed HBT

small-signal model at millimeter-wave frequencies is also proposed. This novel approach is based on an electromagnetic simulation on the extrinsic passive part of a HBT transistor. The S-parameters of the HBT intrinsic active part are computed by using the "multi-port connection method". Following this, the values of all the HBT intrinsic model elements can be obtained by using explicit analytical expressions which have been derived. Good agreement between the measured and the simulated results has been demonstrated. This model has several unique advantages for microwave transistor optimization and synthesis.

Among the various HBT large-signal modeling methods, semi-physical compact model is emphasized. The complete procedure for the Gummel-Poon (GP) model parameter extraction is analyzed and experimental results are also presented. A SiGe HBT amplifier based on the extracted GP model has been designed and fabricated for model verification on the circuit level. Simulation results have been found to be in good agreement with the measurement data. In addition, two improvements on the Vertical Bipolar Inter-Company (VBIC) model, namely, " improved avalanche breakdown model" and " converting technique from the GP to the VBIC model based on local ratio evaluation", are proposed to enhance the performance of the VBIC model and provide the practical approach for the VBIC model development.

Finally, the future research works are proposed.

LIST OF FIGURES

LIST OF TABLES

LIST OF SYMBOLS

The bipolar transistor model parameters and symbols used in Chapter 5, as well as several intermediate variables used in derivation, are not included.

Symbol	Description
C_{bc}	internal base-collector capacitance
C_{be}	base-emitter junction capacitance
C_{ex}	external base-collector capacitance
C_{jc}	base-collector junction capacitance
C_{je}	base-emitter junction capacitance
C_{js}	substrate junction capacitance
exp	exponential
f_{max}	maximum oscillation frequency
f_T	cut-off frequency
G_m	transconductance
G_{m0}	DC transconductance
GP	Gummel-Poon
I_b	base current of a BJT transistor
I_{ce}	current from collector to emitter of a BJT transistor
IIP3	input 3^{rd} order interception point
Im(Imag)	imaginary part of a complex variable
L_B	extrinsic base inductance
L_C	extrinsic collector inductance
L_E	extrinsic emitter inductance

mA	milliampere
mV	millivolt
R_B	extrinsic base resistance
R_b	intrinsic base resistance
R_{be}	base-emitter junction resistance
R_C	extrinsic collector resistance
R_E	extrinsic emitter resistance
Re (Real)	real part of a complex variable
S	S-parameters
T	temperature in Kelvin
tol	convergence tolerance
V	volt
V_{bc} (V_{BC})	voltage between base and collector of a BJT transistor
V_{be}(V_{BE})	voltage between base and emitter of a BJT transistor
VBIC	Vertical Bipolar Inter-Company
V_{ce} (V_{CE})	voltage between collector and emitter of a BJT transistor
Y	Y-parameters
Z	Z-parameters
Z_0	characteristic impedance
α	base transport factor
α_0	common-base DC current gain
ε	objective function
μm	micrometer
τ	delay time
ω	angular frequency

CHAPTER 1

INTRODUCTION

1.1 Background

1.1.1 Heterojunction Bipolar Transistors (HBTs)

The original idea of using a wide band-gap emitter to improve the device performance was firstly proposed by Shockley in 1951 [1] . Later, the concept of HBT was further developed by Kroemer [2],[3]. However, the practical development of HBT technology only started from the early 1980s due to the growing maturity of modern epitaxial growth technology, such as molecular beam epitaxy (MBE) and metal-organic chemical vapor deposition (MOCVD).

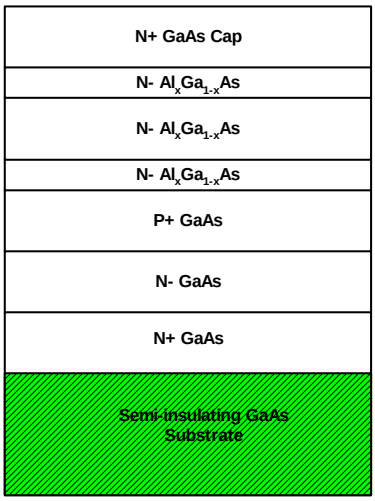

	Thickness (Angstrom)	Doping (cm^{-3})	Al Mole Fraction
N+ GaAs Cap	1500-2000	2×10^{18}	
N- $Al_xGa_{1-x}As$	200-250	5×10^{17}	0 - 0.25
N- $Al_xGa_{1-x}As$	1000	5×10^{17}	0.25
N- $Al_xGa_{1-x}As$	200-250	5×10^{17}	0.25- 0
P+ GaAs	800-1000	$>1 \times 10^{19}$	
N- GaAs	7000	1×10^{16}	
N+ GaAs	5000	$>2 \times 10^{18}$	

Figure 1.1. The schematic diagram of an AlGaAs/GaAs HBT material structure.

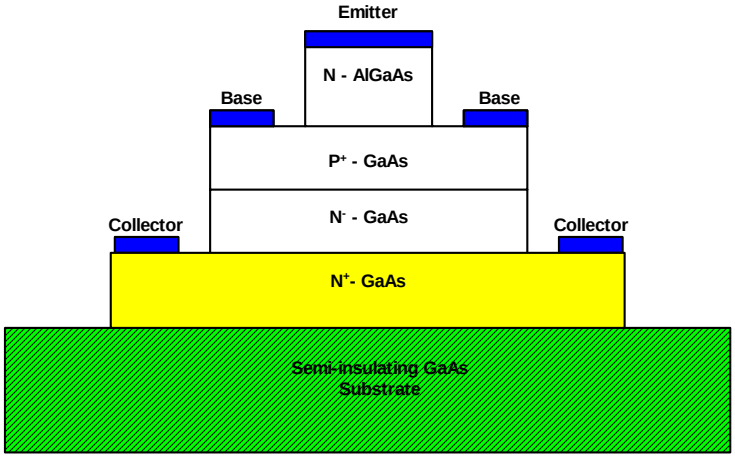

Figure 1.2. The schematic diagram of a typical AlGaAs/GaAs HBT device structure.

The material structure and the cross section of a typical AlGaAs/GaAs n-p-n HBT are shown in Figures 1.1 and 1.2. Unlike a conventional homojunction n-p-n BJT which is made of the same material, in a HBT, the emitter has a larger energy gap than those of the base and collector of the transistor. So, the energy band offsets at the heterointerface can be formed. The resulted base-emitter heterojunction makes the holes from the base meet a much larger energy barrier than those electrons from the emitter. That is, in both abrupt and graded HBTs, the different forces acting on the electrons and holes facilitate the electron injection from the emitter to the base, but retard the hole back-injection from the base to the emitter. In this way, it is possible for us to make the base doping high and the emitter doping low. This is very significant for the high frequency applications, because a high base doping allows a transistor to have a low base resistance and thus a high power gain. Also, a low emitter doping leads to a low base-emitter junction capacitance and thus an improved high-frequency performance. Thus, in a HBT, high emitter injection efficiency can be maintained

while parasitic resistances and capacitances can be lower than those in a conventional homojunction bipolar transistor [4],[5].

The advantages of HBTs over silicon BJTs are listed as follows [6],[7]:

1. Due to the wide band-gap emitter, a much higher base doping can be used to reduce the base resistance.
2. A lower emitter doping can be used and minority carrier storage in the emitter can be negligible to decrease the base-emitter capacitance.
3. Combination of high electron mobility, built-in drift fields and velocity overshoot can be applied to shorten the electron transit time.
4. Semi-insulating substrate can eliminate parasitic capacitances and allow the convenient integration of various different devices.
5. Due to the high base doping, Early voltage can be made higher and high injection effect can be made negligible.
6. Greater radiation hardness can be attainable.

The advantages of HBTs over FETs are also listed as follows [6],[7]:

1. The key distances governing the electron transit are limited by epitaxial growth, instead of lithography, allowing high cut-off frequency with modest processing requirements.
2. The entire emitter area conducts current, contributing to high current handling capability per unit area .
3. The transistor directly controls over the current flow by the input voltage, leading to exponential input-output characteristics and high transconductance .
4. Low output conductance with high transconductance results in the large value of voltage amplification factor.

5. Breakdown voltage can be directly controlled by the epitaxial structure of the device.
6. The threshold voltage is determined by the built-in potential of the base-emitter junction, showing well-matched characteristics.
7. The device is well shielded from traps in the bulk and surface regions, leading to low 1/f noise and the absence of trap-induced frequency dispersion behavior.

The comparison of MESFETs, HEMTs and HBTs [6],[7] is shown in Table 1.1.

Table 1.1 The performance comparison of MESFETs, HEMTs and HBTs (H=High, M=Medium and L=Low)

Parameter	MESFET	HEMT	HBT	Comment
Small-signal				
f_T	L	M	H	HBT has the highest speed
f_{max}	M	H	L	HEMT has the highest frequency
Gain · Bandwidth	M	H	H	HEMT is the best for wideband at high frequency
Noise Figure	M	L	H	HEMT is the best for low-noise amplifiers
Phase Noise	M	H	L	HBT is the best for voltage-controlled oscillators
g_m/g_o	L	M	H	HBT is the best for highly linear amplifiers
$IP3/P_{dc}$	H	M	H	MESFET is the best at high frequency while HBT is the best at low frequency
V_{th} Uniformity	L	M	H	HBT is the best for analog LSI circuits
Hysteresis	H	M	L	HBT is the best for sample and hold circuits
Large-signal				
Collector Efficiency	M	H	H	HBT is potentially the best for power devices
Power Density	M	M	H	HBT is potentially the best for power devices

There exist different types of heterostructures for HBTs, such as AlGaAs/GaAs, GaInP/GaAs in the GaAs-based HBTs, InP/InGaAs, InAlAs/InGaAs in InP-based

HBTs, Si/SiGe in Si-based HBTs and AlGaN/GaN in sapphire-based HBTs. AlGaAs/GaAs is the first heterostructure used in HBTs. The selection of the heterostructure of AlGaAs/GaAs is mainly due to the fact that AlGaAs and GaAs have very similar lattice constants and thermal coefficients. This can eliminate the potential problems in heterostructure device fabrications, such as lattice mismatch at the heterointerface and thermal cracking during the fabrication process [5].

InP-based HBTs can operate at higher frequencies than GaAs-based HBTs. Furthermore, they have demonstrated higher gain due to lower surface recombination, better process control due to etching selectivity, and better heat dissipation for power devices due to higher thermal conductivity. Additionally, the smaller knee and turn-on voltages of InP-based HBTs allow the use of low voltage biases and the increase of the amplifier efficiency. However, InP technology is relatively newer and the available substrates are smaller and more expensive [8].

In general, Si/SiGe HBT technology has some limitations in frequency range and breakdown voltage as compared with GaAs or InP HBT technology. However, it is compatible with silicon planar technology. Also, it has the desirable characteristics to provide higher frequency operation , better gain performance and higher power efficiency than silicon BJT devices. Therefore, this technology can offer great potential for low cost systems integrating RF, analog and digital functions on a single substrate and can perform quite well in the fast-growing wireless communications and advanced information processing application areas [9]-[15].

GaN HBTs are very promising new structures for electronic devices that require operation under high power, high temperature and high frequency conditions. Therefore, the spotlight recently has centered on GaN HBTs for use in various high-frequency applications such as radar and communications where the higher output

current and better linearity are required. However, the main limitations of these HBTs are relatively low current gain , low maximum current density and high offset voltage [16]-[20].

Since the mid 1980s, great efforts of improving reliability and reducing cost have resulted in the rapid progress of HBT technology. Because of their superior performances, HBTs have gained popularity in the high frequency and high speed applications despite of their high cost of material and processing [21]. The nature of HBTs can meet the demands of numerous microwave and millimeter-wave applications, such as power amplifiers, wideband amplifiers and microwave oscillators. Besides, they can also meet the basic requirements for high-speed digital integrated circuits (ICs), such as small propagation delay, low power dissipation and high gate-packing density. They have also found plenty of applications in high-speed digital integrated circuits, such as ultra high-speed HBT circuits for light wave communications, central processor unit (CPU), monolithic direct digital synthesizers, data buffers/ timing generator chips and ultra high-speed HBT gate arrays. For military applications such as radar, communications, electronic warfare and electro-optics, the HBT has become one of the natural candidates from microwave to millimeter-wave ranges as it can meet the principal requirements of different military systems, such as high current driving and voltage handling capabilities, high transconductance, low phase noise and uniform threshold voltage. For the civil applications, HBTs have found numerous application fields such as electronic instruments, optical fiber communications and RF chip sets for wireless communication systems [22]-[25].

1.1.2 Monolithic Microwave Integrated Circuits (MMICs)

A monolithic microwave integrated circuit (MMIC) is a microwave circuit in which the active and passive microwave components are fabricated on the same semiconductor substrate. Since the mid 1970s, the rapid advances of GaAs material, processing and related device development have brought about the feasibility of MMICs. As compared with the conventional hybrid microwave integrated circuits (HMICs) , MMICs have many potentials and important advantages for various microwave applications . For example, (a) they are small size, light weight and low cost in large quantities, (b) they always have reliable and enhanced performance , very good reproducibility and flexibility , (c) they have few parasitic elements, which means that broader bandwidth and higher frequencies can be obtained as compared with HMICs [26]. In recent years, MMICs have achieved rapid and impressive technological advances. MMICs are being used in many system applications, such as direct broadcast by satellite (DBS), phase array radars, electronic warfare, global positioning system (GPS), wireless and optical communications.

1.1.3 Computer-Aided Design (CAD)

In order to make full use of all the advantages of MMICs, it is necessary to improve the accuracy and efficiency of MMIC design and reduce the cost involved in the MMIC development significantly. It is well known that the application of modern computer-aided design (CAD) tools is able to provide an advanced approach to realize all the potentialities of MMICs. Some commercially available CAD software packages are often used to analyze and optimize the performance of many different microwave integrated circuits. They can also perform yield analysis and optimization for the statistical design of various practical MMICs [26].

Without the CAD tools, the whole process for the development and verification of a MMIC prototype would be required inevitably in each trial. Therefore, such a process for the circuit design and fabrication would be very time-consuming and labor- intensive. In contrast, the use of CAD tools in MMIC development can reduce the time and cost to raise the efficiency and performance of MMIC design, it can also link the performance of MMICs to the chip manufacturing process through the related circuit model parameters. It can provide a deeper insight into the microwave integrated circuits as well.

1.1.4 Microwave Device Models

The procedure involved in the definition of the model equations and the extraction of the model parameters is named modeling. The main objective of modeling is to find the required model parameters for the related model equations implemented in the circuit simulator, and to make full agreement between the simulated results and the measured data.

The operation of MMIC CAD tools is largely based on an accurate prediction of the device linear or nonlinear performance involved in the circuit. Based on MMIC CAD tools, the useful circuit simulation results can only be obtained with accurate device models and precisely determined model parameters. Therefore, accurate and reliable models for microwave active and passive devices are crucial. In fact, the constant progress of MMIC CAD technology has been strongly supported by the parallel development of models for microwave active and passive devices. To date, MESFET, HEMT and HBT are three major active devices used in MMICs. Because HBTs have many inherent advantages over MESFETs or HEMTs and they are also the basic building blocks in some practical MMICs, especially in today's MMICs for

wireless communication systems , it is absolutely necessary to develop reliable HBT models for the accurate performance prediction of MMICs.

1.2 Motivations and Objectives

1.2.1 Motivations

In the past several years, a variety of HBT models have been developed and a great deal of device modeling research on HBTs has been conducted. Although significant progress on HBT modeling has been made during the past years, there are still many aspects in this research field which require further study such as the small-signal modeling and large-signal modeling.

First of all, in the HBT small-signal modeling research area, researchers are still looking for practical and effective techniques to obtain reliable initial values and physically-based model parameters so as to raise the modeling accuracy and efficiency [27]-[36] . As a result, there exists a need to develop novel and more efficient model parameter extraction technique for the accurate HBT small-signal modeling. With the increase of the operating frequencies of MMICs, the accurate distributed models for the active devices are needed to take inherent electromagnetic wave coupling effects into consideration. This in turn results in the scaling capability of the active device model to be studied critically [37]-[40]. In this dissertation, it is our interest to investigate a new HBT distributed model for millimeter-wave applications.

As for the HBT large-signal modeling, till now, all the HBT modeling researchers are still trying to develop HBT large-signal models which can cover all the HBT operation regions and include some important device physical effects for practical applications, such as impact ionization, transit time and self-heating effects [41]-[48].

For this reason, it is necessary to develop more accurate and comprehensive HBT large-signal models.

Finally, SiGe HBT modeling should be highlighted because of the rapid progress of Si/SiGe BiCMOS process for modern wireless communication applications. The SiGe HBT characterization and modeling are thus essential for today's enormous RF and microwave applications.

1.2.2 Objectives

The major goal in this dissertation is to formulate and develop several HBT models to accurately simulate the small- and large- signal operations of HBTs for the linear and nonlinear HBT MMIC applications. The basic modeling principle is to achieve trade-off among novelty, accuracy, efficiency and practicality. Several detailed objectives and related research works involved in this dissertation are discussed as follows:

1. One of our main efforts is to identify the strong correlation between the intrinsic and extrinsic HBT model elements. Based on the derived analytical expressions, the extrinsic elements can be optimized individually. Then, the intrinsic elements will be synthesized from the measurement data and the extrinsic elements. The purposes of this new technique are to raise the optimization efficiency, to extract the model elements with full physical meanings and to reach a global minimum as soon as possible.
2. By applying the GPOF method [49], a set of complex exponentials derived from measurement data is used to give information on the initial values of the extrinsic elements for the iterative determination of the HBT model equivalent circuit. In addition, a new technique will be explored to determine the reliable initial values of some extrinsic model elements from the mathematical

manipulations of the set of complex exponentials. The aim of this technique is to reduce the number of unknown extrinsic model elements so as to raise the optimization efficiency and accuracy simultaneously.

3. In order to obtain a more realistic model to cover the propagation effects along the device metallization structure, the electrodes coupling, dispersion phenomena as well as many other effects related to the device passive structure, the "multi-port connection method" [50] and "electromagnetic (EM) simulation of the transistor passive structure" are adopted to establish a new distributed millimetre-wave small-signal HBT model. The main objective of this work is to raise the accuracy and completeness of the HBT small-signal model in the millimetre-wave range and to enhance the scaling capability of the HBT model.
4. The last objective of our research is to develop novel and accurate HBT large-signal models, which can account for some of the HBT's second-order effects. Both Gummel-Poon model [51]-[53] and VBIC model [54]-[56] are two basic modeling references for our new HBT large-signal model development.

1.3 Scope

Chapters 2-4 of this dissertation are devoted to a study on the HBT small-signal modeling techniques. They contain a detailed review of various methods developed for HBT small-signal modeling. Three new methods for the parameter extraction of HBT small-signal models are developed. The strong correlation between extrinsic and intrinsic model elements is clarified in Chapter 2. In Chapter 3, the Generalized Pencil-of-Function (GPOF) method is applied to determine reliable initial values of some

extrinsic model elements. The HBT small-signal modeling based on electromagnetic simulation for millimeter-wave applications is also investigated in Chapter 4.

Chapter 5 includes the classification of transistor large-signal modeling and a detailed review of numerous methods developed for HBT large-signal modeling. Methods ranging from the physical model, the semi-physical compact model, the empirical model and the behavioral model are reviewed. The principles and features of these methods are distinctly pointed out in the chapter. In addition, the basic structure and working principle of the Gummel-Poon (GP) model are discussed. The complete procedure for the GP model parameter extraction is analyzed and experimental results are also presented. A SiGe HBT amplifier is designed and fabricated for the large-signal model verification on the circuit level. Simulation results have been found to be in good agreement with the measurement data.

Chapter 5 also emphasizes the Vertical Bipolar Inter-Company (VBIC) model used for HBT large-signal modeling. The basic structure, working principle of the VBIC model and its advantages over the GP model are discussed. The complete procedure for the VBIC model parameter extraction is included. An improvement on the VBIC avalanche breakdown model is made to enhance the HBT model performance. The chapter also contributes a practical model parameter converting technique from the GP model to the VBIC model.

Chapter 6 is the concluding chapter which summarizes all the theoretical and experimental results described in this dissertation. Meanwhile, several future research areas are also proposed.

1.4 Some Original Contributions

The main contributions in this work are listed as follows:

1. In the HBT small-signal modeling, the strong correlation between extrinsic and intrinsic model elements is clearly illustrated. Relevant analytical expressions are derived and applied to extract the intrinsic model elements, which can be synthesized from the measurement data and extrinsic model elements. A completely new equation is derived to further reduce the number of extrinsic model parameters for optimization.
2. For the first time, the HBT is characterized by describing the S-parameters with a set of complex exponentials by using the Generalized Pencil-of-Function (GPOF) method. The reliable initial values of some extrinsic model elements can be determined from the set of complex exponentials. This new approach can yield a good fit between measured and simulated S-parameters.
3. A novel distributed small-signal HBT model at millimeter-wave frequencies is developed. This new approach is based on an electromagnetic simulation on the extrinsic passive part of a HBT transistor. The S-parameters of the HBT intrinsic active part are computed by using the "multi-port connection method". Then, values of all the HBT intrinsic model elements can be obtained by using explicit analytical expressions which have been derived. Good agreement between the measured and the simulated results has been demonstrated. This model has several unique advantages for microwave transistor optimization and synthesis.
4. A new parameter extraction methodology – "local ratio evaluation" is proposed which is suitable for converting the parameters of one model to those of another one . An example is given for the VBIC model extraction by going through the GP model. It is based on the fact that the VBIC model is a direct enhancement and extension of the GP model. This method can provide an

accurate and practical way to extract some VBIC model parameters from the known GP model data sets.

5. An improved compact bipolar transistor model for avalanche breakdown of HBTs is presented. Based on various device electrical characterizations that are classified into three groups, a modified VBIC avalanche multiplication model is developed. By simply replacing one constant avalanche model parameter with a linear current dependent parameter, the new model predicts the transistor breakdown behavior well from weak avalanche region up to high injection region.

The contributions made in the various sub-areas as mentioned above are reported in the following publications:

(a) Journals

1. B.L.Ooi, T.S.Zhou, and P.S.Kooi, " AlGaAs/GaAs HBT model estimation through the generalized pencil-of-function method," IEEE Transaction on Microwave Theory and Techniques, MTT-49 , pp.1289-1294, 2001.
2. T.S.Zhou, B.L.Ooi, F.J.Lin and P.S.Kooi, " A novel approach for determining the AlGaAs/GaAs HBT small-signal equivalent circuit elements," Microwave and Optical Technology Letters, pp.278-282, 2001.
3. B.L.Ooi, T.S.Zhou, and P.S.Kooi, "An efficient method for HBT Model parameter extraction based on the correlation between extrinsic and intrinsic elements, " International Journal of RF and Microwave CAE, vol.12, pp.311-319, 2002.
4. F.J.Lin, T.S.Zhou , B.Chen, B.L.Ooi, and P.S.Kooi, "SiGe HBTs model converting technique from SGP Model to VBIC Model," Microelectronics Journal, vol.33, pp.45-54, 2002.

5. F.J.Lin, B.Chen, T.S.Zhou , B.L.Ooi, and P.S.Kooi, " A study on the avalanche multiplication in HBTs," Microelectronics Journal, vol.33, pp.39-43, 2002.

6. B.L.Ooi, T.S.Zhou, P.S.Kooi , "A distributed millimeter-wave small-signal HBT model based on electromagnetic simulation," Submitted to IEEE Transaction on Microwave Theory and Techniques , 2003.

(b) Conferences

1. T.S.Zhou , B.L.Ooi, F.J.Lin and P.S.Kooi, "A novel approach for HBT model parameter extraction," Progress in Electromagnetics Research Symposium, 2000, pp.1055.

2. F.J.Lin, T.S.Zhou , B.Chen, B.L.Ooi, and P.S.Kooi, "Extraction of VBIC model for SiGe HBTs model made easy by going through Gummel-Poon model, "Proceeding of SPIE, vol.4228, 2000, pp. 249-258.

3. F.J.Lin, B.Chen, T.S.Zhou, B.L.Ooi, and P.S.Kooi, " Characterization and modeling of avalanche multiplication in HBTs, " Proceeding of SPIE, vol.4228, 2000 , pp.158-163.

4. B.L.Ooi, T.S.Zhou, F.J.Lin and P.S.Kooi, " A distributed small-signal HBT model for millimeter-wave applications," International Conference on Microwave and Millimeter Wave Technology, Beijing, China, 2002.

CHAPTER 2

HBT SMALL-SIGNAL MODELING

Microwave circuit CAD requires microwave device models with excellent accuracy, especially for the active devices. The equivalent circuit modeling approach has commonly been used to characterize microwave active devices. The extensive investigation of the high frequency performance of various microwave devices using the equivalent circuit models and the appropriate parameter extraction techniques is a powerful tool for device characterization and performance optimization. When HBT models are classified according to the device operating condition, they can be grouped into small-signal and large-signal models. Among these models, an accurate characterization of the small-signal model is extremely important since an accurate HBT small-signal model not only is essential for the accurate MMIC design, but also is the stepping stone for accurate HBT large-signal modeling.

This chapter will discuss the issue of HBT small-signal modeling. The HBT small-signal modeling methods are classified into two groups and many different methods reported in the literature are reviewed. A new technique will be adopted to develop accurate and efficient HBT small-signal model. In this proposed technique, the strong correlation between extrinsic and intrinsic HBT small-signal model elements will be derived in explicit forms and will be used to enhance the accuracy and efficiency of the model optimization.

2.1 Historical Background

Different methods for the determination of the HBT small-signal models were presented in the past and numerous improvements on the characterization techniques have been proposed [27]-[36] & [57]-[74] . Generally speaking, HBT small-signal modeling methods can be classified into two groups. They include analytical extraction method and numerical optimization method.

Some authors have applied the analytical extraction method as described in [27]-[36] & [57]-[71] . Costa *et al.* [27], [57] first described a novel analytical modeling method, in which some special layouts and device structures were used to extract most of the parasitic model parameters. In their method, the intrinsic model elements were calculated analytically after de-embedding the related parasitic components. Unlike [27],[57], Wei *et al.* [58] did not use special test patterns or numerical optimization techniques. Instead, they proposed an approach in which all the HBT model elements were obtained analytically from the small-signal S-parameters measured at different frequencies or under different bias conditions such as "open-collector" condition. During the model parameter extraction, the distributed nature of the HBT base region could be analyzed naturally. A more physical HBT equivalent circuit with a simple π-RC circuit, which could be used to analyze the physical operation of the HBT, was developed by Gobert *et al.* [29] . The main feature in [29] is that the parasitic model elements, particularly, the parasitic capacitances, were determined by a direct extraction method. References [59] and [28] may be useful for the derivation of the analytical expressions in the HBT small-signal model. To extract the model elements, Li *et al.* [59] had applied some basic simplifications and approximations based on the wide range of frequencies (low, medium and high). Consequently, a fully analytical model element extraction procedure was established based on those simplifications and approximations. Similarly, in [28], Schaper *et al.* had adopted some reasonable

assumptions and approximations to derive extrinsic elements analytically. As a result, a pure analytical modeling method could be developed. In [34], a set of closed form equations was derived without any approximations. Therefore, in this method, all the intrinsic model elements with unique and physically meaningful values could be determined from the measured S-parameters. Li *et al.* [60] , Samelis *et al.* [30] and Rios *et al.* [31] had introduced new sets of parameter extraction approaches for HBT small-signal modeling. In their semi-analytical approaches , the analytical approach and empirical optimization procedure were combined. In order to improve the optimization performance, it should be noted that the initial values of those uncertain elements were obtained from special measurements and some analytical approaches. Spiegel *et al.* [61] introduced the HBT small-signal equivalent circuit which included the extrinsic base-collector capacitance and extrinsic base resistance. Their work provided a more complete HBT small-signal equivalent circuit, which is more closely related to the physical structure of the device. In consequence, a better fitting between the simulated and the measured S-parameters was obtained in a wide frequency range. Maas, *et al.* [62] adopted the hybrid-T small-signal equivalent circuit in their work and separated the parasitic emitter resistance from the base-emitter junction resistance. The most important contribution of their work is that they emphasized a very useful fact , that is, the HBT's impedance parameter Z_{12} is nearly real and constant with frequency. Therefore, based on this fact, an additional equation in terms of all the HBT small-signal extrinsic model elements can be found which may help to reduce the number of unknowns for the following optimized extraction of model parameters [63].

Meanwhile, some authors had applied numerical optimization modeling method to determine the model parameters by minimizing the difference between measured

data and simulated results [72]-[74]. Generally speaking, the major steps in the conventional optimization modeling method are (a) setting the initial values for all the model parameters, (b) selection of error functions and (c) adoption of reliable numerical iteration algorithm. Many additional test structures and measurements are not needed in this method and some extra simplifications and approximations are totally omitted. Therefore, the model fitting performance is greatly improved. However, this method is sensitive to the selection of initial values, which can strongly affect the final numerical convergence. Also, it is difficult to use this method to find the suitable model parameters with physical meanings and to reach the global minimum in the optimization iteration process. To improve the optimization modeling method, Menozzi *et al.* [72]-[73] employed the " genetic algorithm" to eliminate the need of carefully choosing an initial solution as a starting point for the conventional optimization method. Meanwhile, Bilbro *et al.* [74] had adopted the method of "tree annealing" to prevent the traps in local minima during the optimization.

2.2 Correlation between Extrinsic and Intrinsic HBT Model Elements

As discussed above, in order to determine the model parameters, some of the conventional methods require some extra measurements at DC, very low frequencies, "cold state" or some special test structures. They also require some low and high frequency approximations [59]. The other conventional methods for the determination of the HBT's equivalent circuit are through the minimization of the difference between the measured and computed S-parameters. However, it is relatively difficult for this procedure to produce unique element values for an equivalent circuit and the great number of variable elements produces an equivalent circuit which is strongly

dependent on the initial values. In addition, the correlation between the intrinsic and the extrinsic model parameters is unclear.

Thus, one can conclude that the key problem of obtaining a good physical equivalent circuit lies in the derivation of the strong correlation between intrinsic and extrinsic model elements and the accurate determination of the extrinsic elements or, equivalently, in the reduction of the number of unknowns for optimization so that a smaller search space exists. In the field of MESFET modelling, Shirakawa *et al.* [75] and Ooi *et al.* [76] have shown the dependence of the intrinsic parameters on the extrinsic parameters. In this section, a modified technique is described to determine an AlGaAs/GaAs HBT equivalent circuit, which requires no additional measurements except S-parameters. This proposed method is an extension of [75] and [76] in that an additional equation is derived to further reduce the number of extrinsic model parameters for optimization and only five unknowns are required for optimization . For the first time in HBT modelling, the dependence of one of the extrinsic parameters on the other extrinsic parameters is illustrated clearly. The derived expression shows that the value of extrinsic base inductor L_B can be obtained based on such a dependence.

2.2.1 Equivalent Circuit Model of the HBT Transistor

A typical equivalent circuit for the AlGaAs/GaAs HBT is adopted in the parameter extraction technique, in which seven intrinsic elements and six extrinsic elements are included.

The adopted equivalent circuit is shown in Figure 2.1. The distributed base is represented by a combination of internal base-collector capacitor C_{bc}, external base-collector capacitor C_{ex} and intrinsic base resistance R_b . The base-emitter junction impedance is represented by C_{be} and R_{be} . The extrinsic collector, base and emitter

impedances are denoted by R_C / L_C , R_B / L_B and R_E / L_E . The base transport factor α is expressed in terms of a current gain α_0 and a delay time τ . $\alpha = \alpha_0 \exp(-j\omega\tau)$, where ω is the angular frequency.As indicated in the figure, the intrinsic part of the HBT transistor is the part which excludes the elements R_E, L_E, R_B, L_B, R_C and L_C . The respective intrinsic Z-parameters Z_{int} are described as:

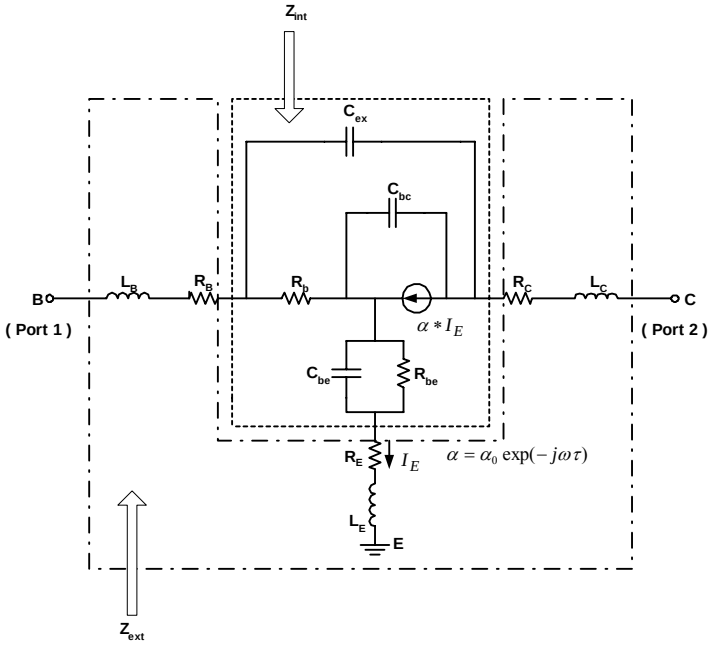

Figure 2.1. Equivalent circuit of an AlGaAs/GaAs HBT . Inside the dashed-line denotes the intrinsic part and the outside is the extrinsic part.

$$Z_{\text{int}} = \begin{bmatrix} Z_{11} & Z_{12} \\ Z_{21} & Z_{22} \end{bmatrix}, \tag{2.1}$$

where

$$Z_{11} = \frac{[(1-\alpha)Z_{bc} + Z_{ex}]R_b}{Z_{bc} + Z_{ex} + R_b} + Z_{be} \ , \tag{2.2}$$

$$Z_{12} = \frac{(1-\alpha)Z_{bc}R_b}{Z_{bc}+Z_{ex}+R_b} + Z_{be} \ , \tag{2.3}$$

$$Z_{21} = \frac{[-\alpha Z_{ex} + (1-\alpha)R_b]Z_{bc}}{Z_{bc}+Z_{ex}+R_b} + Z_{be} \ , \tag{2.4}$$

$$Z_{22} = \frac{(1-\alpha)Z_{bc}(Z_{ex}+R_b)}{Z_{bc}+Z_{ex}+R_b} + Z_{be} \ , \tag{2.5}$$

$$Z_{be} = \frac{R_{be}}{1+j\omega R_{be}C_{be}} \ , \tag{2.6}$$

$$Z_{bc} = \frac{1}{j\omega C_{bc}} \ , \tag{2.7}$$

and

$$Z_{ex} = \frac{1}{j\omega C_{ex}} . \tag{2.8}$$

The extrinsic part of the transistor, which is located outside the range of intrinsic part, is related to the intrinsic part through the following expressions:

$$Z_{\text{int}} = Z_{total} - Z_{ext} \ , \qquad Z_{total} = \begin{bmatrix} Z_{11}^{total} & Z_{12}^{total} \\ Z_{21}^{total} & Z_{22}^{total} \end{bmatrix}, \tag{2.9}$$

and

$$Z_{ext} = \begin{bmatrix} R_E + R_B + j\omega L_E + j\omega L_B & R_E + j\omega L_E \\ R_E + j\omega L_E & R_E + R_C + j\omega L_E + j\omega L_C \end{bmatrix} , \tag{2.10}$$

where Z_{total} is the overall Z-parameters and Z_{ext} is the extrinsic Z-parameters.

2.2.2 Analytical Determination of the Equivalent Circuit Elements

The conventional optimizer programs often assume that all the elements have the same accuracy and correlation, and that the extrinsic parameters can fluctuate widely about their initial values. However, at microwave frequencies, it is noted that with a slight change in any of the extrinsic elements' values, some drastic changes in some of the intrinsic elements' values are noted [76].

Therefore, the extrinsic parameters cannot be assumed to have a wide range of initial values. There must exist a strong correlation between extrinsic and intrinsic elements. The main effort here is to identify the strong correlation between the intrinsic and extrinsic elements. Once this kind of correlation is obtained, the extrinsic elements can be optimized individually. The intrinsic elements can then be synthesized from both the measurement data and the extrinsic elements. This new technique can reduce the search space and establish a sharp bend of the search boundary close to the object node, which yields an increased possibility in finding the model elements with physical meanings and the global minimum of the optimization target.

The overall measured S-parameters are first converted to Z-parameters, and by using equations (2.9) and (2.10), the intrinsic Z-parameters are obtained. The intrinsic elements at each frequency point are derived based on the equivalent circuit which we have adopted. The detailed expressions, which show the strong dependence of any one of the intrinsic elements on the extrinsic elements and the measured data, are given as follows :

$$\alpha_0 = \frac{\mathrm{Re}(a)}{\cos(\omega\tau)} \ , \tag{2.11}$$

$$\tau = \frac{-1}{\omega} \tan^{-1}\left[\frac{\mathrm{Im}(a)}{\mathrm{Re}(a)}\right] , \tag{2.12}$$

$$C_{ex} = \frac{\mathrm{Re}(c)}{\omega[\mathrm{Re}(d)\,\mathrm{Im}(c) - \mathrm{Im}(d)\,\mathrm{Re}(c)]} , \tag{2.13}$$

$$C_{bc} = \frac{\mathrm{Re}(e)}{\omega[\mathrm{Im}(d)\,\mathrm{Re}(c) - \mathrm{Re}(d)\,\mathrm{Im}(c)]} , \tag{2.14}$$

$$R_b = \frac{\mathrm{Re}(b)[\mathrm{Re}(d)\,\mathrm{Im}(c) - \mathrm{Im}(d)\,\mathrm{Re}(c)]}{\mathrm{Re}(d)} , \tag{2.15}$$

$$R_{be} = \frac{[\mathrm{Re}(f)]^2 + [\mathrm{Im}(f)]^2}{\mathrm{Re}(f)} , \tag{2.16}$$

and

$$C_{be} = \frac{\mathrm{Im}(f)}{\omega\{[\mathrm{Re}(f)]^2 + [\mathrm{Im}(f)]^2\}} , \tag{2.17}$$

where

$$a = \frac{Z_{12} - Z_{21}}{Z_{22} - Z_{21}} , \tag{2.18}$$

$$b = \frac{Z_{11} - Z_{12}}{Z_{22} - Z_{21}} , \tag{2.19}$$

$$c = Z_{22} - Z_{21} , \tag{2.20}$$

$$d = Z_{22} - Z_{21} + Z_{11} - Z_{12} \ , \tag{2.21}$$

$$e = \left(\frac{Z_{12} - Z_{22}}{Z_{22} - Z_{21}} \right) \frac{\mathrm{Re}(Z_{22} - Z_{21} + Z_{11} - Z_{12})}{\mathrm{Re}(Z_{22} - Z_{21})} Z_{11} \quad , \tag{2.22}$$

and $$f = Z_{12} + \left(\frac{Z_{12} - Z_{22}}{Z_{22} - Z_{21}} \right) \frac{\mathrm{Re}(Z_{22} - Z_{21} + Z_{11} - Z_{12})}{\mathrm{Re}(Z_{22} - Z_{21})} (Z_{12} - Z_{11}) \, . \tag{2.23}$$

Normally, the HBT's impedance parameter Z_{12} is nearly real and constant with frequency, i.e., the imaginary part of Z_{12} of the HBT tends towards zero [62]. It has also been proved that this fact is valid for our studied HBT devices and the measurement frequency range. Therefore, an additional equation in terms of the extrinsic elements can be found based on this fact, which is reproduced here as:

$$L_B = \omega^{-1} \cdot \frac{\left(\mathrm{Im}\left(Z_{12}^{total}\right) - \omega L_E + \mathrm{Im}(g)\right) \cdot \left| Z_{12}^{total} - R_E - j\omega L_E + g \right|^2}{\left(\mathrm{Re}\left(Z_{12}^{total}\right) - R_E + \mathrm{Re}(g)\right)} \ ,$$

where

$$g = \left(\frac{Z_{12}^{total} - Z_{22}^{total} + R_C + j\omega L_C}{Z_{22}^{total} - Z_{21}^{total} - R_C - j\omega L_C} \right) \left(\frac{\mathrm{Re}\left(Z_{22}^{total} - Z_{21}^{total} + Z_{11}^{total} - Z_{12}^{total}\right) - R_B - R_C}{\mathrm{Re}\left(Z_{22}^{total} - Z_{21}^{total}\right) - R_C} \right) \left(Z_{22}^{total} - Z_{11}^{total}\right) \tag{2.24}$$

.

Equations (2.11) to (2.23) indicate that there is a strong correlation between the extrinsic and intrinsic elements and the change in the intrinsic elements is solely

governed by equations (2.11) to (2.23). Therefore, extrinsic elements cannot assume wide initial values as they will cause some of the intrinsic elements' values to be non-physical or eventually a termination to a local minimum.

From equation (2.24), we also see that at least one of the extrinsic elements can be expressed in terms of the other extrinsic elements. For clarity and simplicity in demonstration, we choose to express L_B in terms of R_E, L_E, R_B, R_C and L_C, i.e.,

$$L_B = f_0(\omega_i, R_E, L_E, R_B, R_C, L_C), \tag{2.25}$$

where ω is the angular frequency, and i ($i = 0,\ldots, N-1$) is the number of sampling frequency points.

Once the values of R_E, L_E, R_B, R_C, L_C are known, all the other elements, $L_B, C_{bc}, C_{ex}, R_b, C_{be}, R_{be}, \alpha_0$ and τ can be determined.

2.2.3 The Motivation of the Proposed Algorithm

The conventional optimization algorithms begin with an initial value vector for all variables and gradually approach the objective within the large searching domain. Therefore, the conventional method cannot always establish satisfactory results in the model parameter extraction [77].

The adoption of equations (2.11) to (2.24) allows the physically based parameters' values to be extracted. The bound generated by equations (2.11) to (2.24) will constrain the search space to the physical domain and as such, non-physical values for the parameters are greatly reduced. The resultant solution from the new form of optimization will have a better physical meaning for the parameter values as compared to the conventional method. The likelihood of trapping at a local minimum has been reduced. Meanwhile, the probability to escape from the local minima has been

increased in that only permissible values based on the correlation of the model elements can be generated. The bounds for the eight model parameters (R_{be}, C_{be} ,C_{ex} ,C_{bc} ,R_b ,α_0 , τ , and L_B) have been physically constrained by the bounds of the remaining five unknown model parameters, namely, L_E , L_C , R_E ,R_B , and R_C .

Besides, our proposed method has a lesser degree of freedom as it has now five unknowns for optimization. In contrast to the conventional method, which has thirteen unknowns, the proposed method has a greater degree of convergence as the present search space is drastically reduced. The sensitivities of these five unknown element parameters are independent as compared to the conventional thirteen unknown model elements where they are all interrelated. Through a judicious selection of the five elements for optimization, one can make the sensitivity of these five elements change in descending order. In doing so, the process of optimization can be greatly improved and the complexity of the optimization can be greatly simplified.

2.2.4 The Proposed Algorithm

For brevity, we substitute equation (2.25) into equations (2.11) to (2.23). Thus, we can express the above correlation as a set of functions of the remaining five unknown extrinsic elements. They are namely,

$$\alpha_0 = f_1(\omega_i, R_E, L_E, R_B, R_C, L_C) \ , \tag{2.26}$$

$$\tau = f_2(\omega_i, R_E, L_E, R_B, R_C, L_C) \ , \tag{2.27}$$

$$R_{be} = f_3(\omega_i, R_E, L_E, R_B, R_C, L_C) \ , \tag{2.28}$$

$$C_{be} = f_4(\omega_i, R_E, L_E, R_B, R_C, L_C), \tag{2.29}$$

$$R_b = f_5(\omega_i, R_E, L_E, R_B, R_C, L_C), \tag{2.30}$$

$$C_{bc} = f_6(\omega_i, R_E, L_E, R_B, R_C, L_C), \tag{2.31}$$

and $$C_{ex} = f_7(\omega_i, R_E, L_E, R_B, R_C, L_C). \tag{2.32}$$

We use the function names f_0 to f_7 for convenience in the following discussions of our proposed method.

Although the Figure 2.1 has been adopted for our analysis, our method can be extended to some other equivalent circuits. As an example, by substituting

$$[Z] = \left(\begin{bmatrix} Y_{11}^{total} & Y_{12}^{total} \\ Y_{21}^{total} & Y_{22}^{total} \end{bmatrix} - \begin{bmatrix} j\omega C_{pbe} & 0 \\ 0 & j\omega C_{pce} \end{bmatrix} \right)^{-1} \tag{2.33}$$

into equations (2.1) to (2.5), the equivalent circuit with pad capacitors C_{pbe} and C_{pce} can be adopted. Here, the first term of the enclosed bracket of equation (2.33) is the total measured Y-parameters, C_{pbe} and C_{pce} are two added base and collector parasitic pad capacitors of the HBT transistor.

In our proposed method, the intrinsic elements as well as one of the extrinsic elements are used as an optimization criterion. The first objective function for our approach is presented as:

$$\varepsilon_1^{\,k}(R_E, L_E, R_B, R_C, L_C) =$$

$$\frac{1}{N-1}\sum_{i=0}^{N-1}\left|\rho_k f_k(\omega_i, R_E, L_E, R_B, R_C, L_C) - \overline{\sum_{i=0}^{N-1}\rho_k f_k(\omega_i, R_E, L_E, R_B, R_C, L_C)}\right|^2, \qquad (2.34)$$

where k varies from one to seven, N is the total number of frequency points, ρ_k is a normalizing factor to make f_k vary between zero and one, and the overbar indicates the mean value. For stable calculations, the discrepancy between the measured and calculated S-parameters must also be checked. For this reason, the second objective function is selected as:

$$\varepsilon_2(R_E, L_E, R_B, R_C, L_C) =$$

$$\sum_{p=1}^{2}\sum_{q=1}^{2}\sum_{i=0}^{N-1}\sigma_{pq}\left|\frac{S_{pq}^{m}(\omega_i, R_E, L_E, R_B, R_C, L_C) - \overline{S}_{pq}^{c}(\omega_i, R_E, L_E, R_B, R_C, L_C)}{S_{pq}^{m}(\omega_i, R_E, L_E, R_B, R_C, L_C)}\right|^2, \qquad (2.35)$$

where superscripts c and m denote, respectively, the calculated and measured S-parameters. σ_{pq}, which is arbitrarily selected at 0.5 and is the weighting factor. The overbar indicates that the mean values of f_0 to f_7 are used to compute the S-parameters. Taking the mean values of f_0 to f_7 implies that the global solution occurs at the mean values of these functions. The extended error vector is thus expressed as:

$$\varepsilon(R_E, L_E, R_B, R_C, L_C) = \begin{bmatrix} \varepsilon_1^{k}(R_E, L_E, R_B, R_C, L_C) \\ \varepsilon_2(R_E, L_E, R_B, R_C, L_C) \end{bmatrix}. \qquad (2.36)$$

By selecting the appropriate values for the five remaining unknown extrinsic elements, $L_B, C_{bc}, C_{ex}, R_b, C_{be}, R_{be}, \alpha_0$ and τ can then be chronologically evaluated from equations (2.25) to (2.32). A flowchart of the iterative process is shown in Figure 2.2.

First, S-parameter measurement is conducted on a chosen HBT transistor and total S-parameters can be obtained. Then, total S-parameters need to be converted to the total Z-parameters. Using an appropriate set of initial values for R_E, L_E, R_B, R_C and L_C, which are obtained by specialized measurements or GPOF method in the next chapter, L_B can be determined by equation (2.24) . In the next step, the intrinsic Z-parameters can be extracted from the total Z-parameters based on the equations (2.9) and (2.10). Then, all the intrinsic model elements can be calculated based on equations (2.11)-(2.23). After the extraction of all the model parameters, the two objective functions can be evaluated in comparison with the set error tolerance. If the objective functions are larger, the values of R_E, L_E, R_B, R_C and L_C must be updated by using Levenberg-Marquardt method. The whole iterative optimization process can only be terminated if the objective functions are less than the pre-assigned error tolerance.

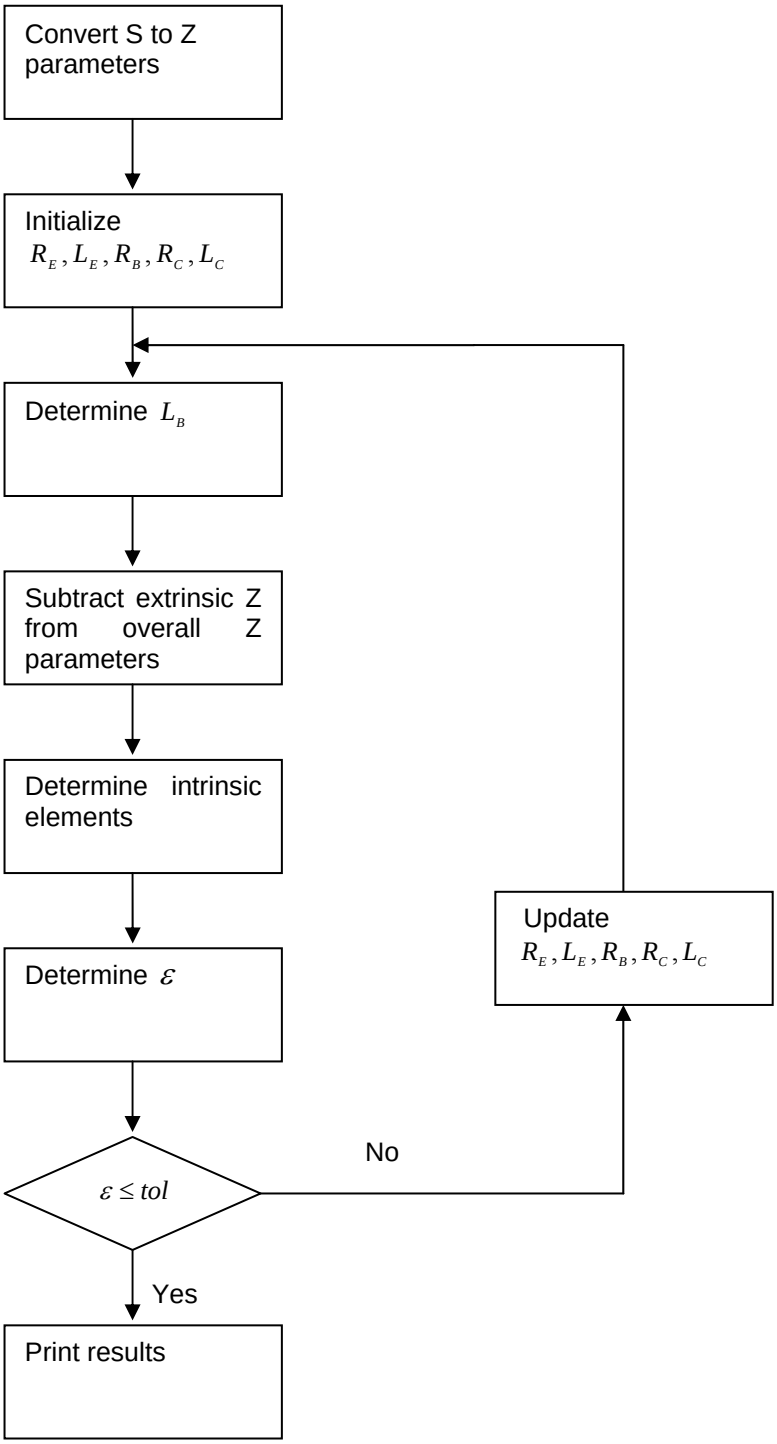

Figure 2.2. The algorithm.

2.2.5 Experiments, Results and Discussions

A MATLAB program has been developed based on the flowchart given in Figure 2.2. The values of R_E, L_E, R_B, R_C and L_C are initially generated by the method of [29]. The values of these five remaining extrinsic elements are updated by Levenberg-Marquardt method [78], [79].

Our modeled AlGaAs/GaAs HBT contains 2 emitter fingers, each of which is 2 μm wide and 10 μm long. The biasing condition is: I_C=15 mA , V_{CE}=3V, and the frequency range is from 0.2GHz to 18.0 GHz. The element values extracted using our technique are shown in Table 2.1. The comparison between the measured and calculated S-parameters under the proposed technique for the AlGaAs/GaAs HBT

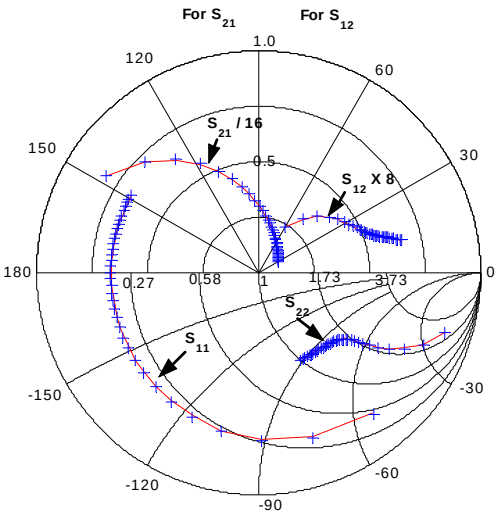

Figure 2.3. Comparison of S-parameters between measured and simulated data. Crosses indicate measured values and solid lines indicate simulated values.

is presented in Figure 2.3. A close agreement between the measured and calculated S-parameters is noted from the figure. It is noted also that the fitting effect is the best for

the parameter of S_{12} , whose RMS error is calculated as 0.9%. Meanwhile, the RMS error is lower than 1.2% for the other remaining S-parameters. Measurement setup is shown in Figure 2.4.

Table 2.1 The extracted values of extrinsic and intrinsic elements

$R_E(\Omega)$	$L_E(pH)$	$R_B(\Omega)$	$L_B(pH)$	$R_C(\Omega)$	$L_C(pH)$
5.134	10.890	8.183	45.360	9.290	50.140
$R_{be}(\Omega)$	$C_{be}(pF)$	$C_{ex}(pF)$	$C_{bc}(pF)$	$R_b(\Omega)$	α_0	$\tau(ps)$
4.148	0.646	0.026	0.048	8.568	0.954	4.817

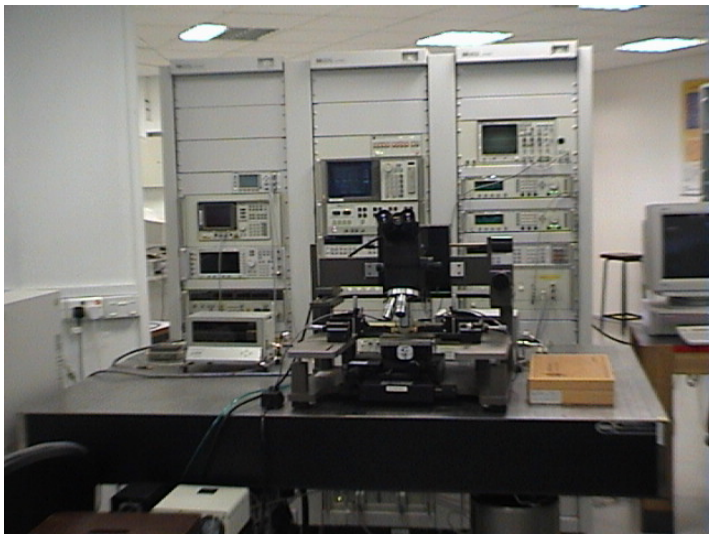

Figure 2.4. Measurement setup for S-parameters

The HF measurement has been performed using the HP8510C network analyzer and 8515A S-Parameter test set connected to the HP4156 parametric dc analyzer. System calibration has been performed using the LRRM calibration. Subsequently open (Y) and short (Z) de-embedding was performed to obtain S-parameters from raw measurements to eliminate the influence of the probe pads. The devices have been in the 2-port GSG layout configuration for the base and collector terminals. The emitter

terminal has been pulled out separately and ac grounded using a GSG probe. The models have been verified for various frequencies by varying the Vbe voltage and the Vce voltage. The measurement temperature is 25°C.

It is noted that an applicable extraction method should have a unique solution which is independent of the starting vector, i.e., for a given data set, the optimization routine should yield consistent results. The problem of uniqueness for the proposed technique is examined by carrying out 80 individual extractions with randomly generated starting vectors. A total of 80 starting vectors have been varied within ± 50% on the basis of the initial values in [29] for the inductances, and within ± 100% for the resistances. These starting vectors are then optimized by the Levenberg-Marquardt method.

For comparison of the uniqueness or uncertainty of the extracted model elements, Table 2.2 is used to summarize the results obtained in the form of mean values P_0 and standard deviation σ for three different methods (methods A, B and C). In method A, we applied our newly proposed approach , whose initial values of extrinsic elements were obtained with the method of [80] ; In method B, we also applied the same approach as that in method A, but the initial values of extrinsic elements were obtained with the method of [29]; In method C, the conventional modeling method with straight optimization algorithm was adopted. As noted from Table 2.2, methods A and B with our newly proposed approach have smaller deviations σ as compared with the conventional modeling method with straight optimization algorithm. Hence, our newly proposed approach is much better than the conventional modeling method with straight optimization algorithm, as the uncertainty of the final extracted model elements has been reduced through a narrow search space.

Table 2.2 A comparison of mean values (P_0) and standard deviations (σ) between the proposed new approach (method A, B) and the conventional straight optimization method (method C)

ELEMENT	Method A		Method B		Method C	
	P_0	σ	P_0	σ	P_0	σ
$R_E(\Omega)$	5.145	0.028	5.169	0.013	5.003	0.106
$L_E(pH)$	10.703	0.012	11.012	0.018	11.971	0.169
$R_B(\Omega)$	8.210	0.065	8.157	0.009	8.688	0.101
$L_B(pH)$	45.311	0.007	44.066	0.075	43.977	0.511
$R_C(\Omega)$	9.286	0.009	9.037	0.013	9.867	0.125
$L_C(pH)$	50.210	0.017	51.350	0.007	54.009	0.307
$R_{be}(\Omega)$	4.138	0.039	4.441	0.059	4.656	0.341
$C_{be}(pF)$	0.652	0.035	0.765	0.024	0.861	0.111
$C_{ex}(pF)$	0.031	0.001	0.036	0.001	0.054	0.020
$C_{bc}(pF)$	0.043	0.001	0.061	0.002	0.077	0.012
$R_b(\Omega)$	8.498	0.017	8.711	0.057	8.015	0.561
α_0	0.944	0.027	0.938	0.009	0.901	0.045
$\tau(ps)$	4.818	0.009	4.671	0.030	4.463	0.084

For comparison of the accuracy and the efficiency of several different modeling methods, Table 2.3 is used to compare RMS error contributed from the difference between simulated and measured HBT S-parameters. The adopted RMS error *RMSerr* is given as:

$$RMSerr = \sqrt{\sum_{i=1}^{N}\left[(sim_i - meas_i)^2\right] \Big/ \sum_{i=1}^{N} meas_i^{\,2}} \quad , \tag{2.37}$$

where sim_i is the *i* th simulated data point, $meas_i$ is the *i* th measured data point, and N is the total number of data points.

Table 2.3 A comparison of the RMS error & CPU time taken between the proposed new approach (method A, B) and the conventional straight optimization method (method C)

ITEM	Method A	Method B	Method C
RMS ERROR	0.95%	1.11%	3.57%
CPU TIME TAKEN	2.5 min	3.8 min	30.2 min

The CPU time consumed by methods A, B, and C is also included in the table. As noted from Table 2.3, our newly proposed modeling approach (method A and B) has a lower RMS error as compared with the conventional modeling method with straight optimization algorithm. In addition, our newly proposed modeling approach (method A and B) has a faster rate of convergence and takes about 3 minutes for completion, while the conventional modeling method with straight optimization algorithm takes about 30 minutes for completion.

It should be mentioned that our method can also be extended to multi-bias extraction. As noted, once the unknowns R_E, L_E, R_B, R_C and L_C are known at all biases, the corresponding iterative elements, i.e., $L_B, C_{bc}, C_{ex}, R_b, C_{be}, R_{be}, \alpha_0$ and τ at all bias points can be found. For brevity , the multi-bias extraction is not presented here.

2.3 Conclusion

In this chapter, a simple and efficient technique for the small-signal HBT equivalent circuit parameter extraction has been introduced. The strong correlation between extrinsic elements and intrinsic elements is analyzed in depth and the detailed expressions are obtained. The intrinsic elements are described as the functions of the extrinsic elements. Assuming that the equivalent circuit is valid over the whole frequency range of the measurements, the extrinsic elements are iteratively determined by using the variance of the intrinsic elements as an optimization criterion. Also, for the first time in HBT modeling, an explicit equation on the total extrinsic elements, which results in a reduction of the number of optimization variables, is derived. It is shown that the modeling algorithm based on the above correlation and derived equations can help to improve the modeling accuracy and efficiency. Although the technique is based on an iterative calculation, the elimination of additional measurements in our proposed method is certainly a big advantage, for example, in yield estimation.

CHAPTER 3

THE HBT SMALL-SIGNAL MODEL ESTIMATION THROUGH THE GPOF METHOD

In this chapter, another new technique is applied to develop the more accurate and efficient HBT small-signal models. The generalized pencil-of-function (GPOF) method [49] is adopted and studied for the microwave device modeling. This method is an effective way to describe the high frequency performance of microwave devices. It can provide a good approach to extract some reliable initial values of HBT small-signal model elements for optimization. By applying the generalized pencil-of-function (GPOF) method, we can approximate the S-parameters of the AlGaAs/GaAs HBT with only a few sets of complex exponentials. This approach can provide less data manipulation and storage, and can approximate the measured S-parameters with excellent accuracy, as it is very robust in eliminating statistical noise. Reliable initial values of the extrinsic model elements in the HBT small-signal equivalent circuit by using the sets of complex exponentials can also be obtained.

3.1 The Generalized Pencil-of-Function (GPOF) Method

The generalized pencil-of-function (GPOF) method has been described in detail in [81]-[85], and has been demonstrated to be very robust to statistical noise and efficient in computation.

In the GPOF method, the objective is to fit a complex function by the sum of damped complex exponentials, that is :

$$y_k \cong \sum_{i=1}^{M} R_i (z_i)^k \ , \tag{3.1}$$

where $k = 0,1,...,N-1$ is the number of sampling data, M is the number of complex exponentials and determined by the ratio of the various singular values to the largest one, R_i s are the residues and z_i s denote the poles. The basic idea of the GPOF method is to formulate an eigenvalue problem for the determination of the poles z_i s.

Following the GPOF method as in [49] , we define matrices Y_1 and Y_2 as :

$$Y_1 = \begin{bmatrix} y_0 & y_1 & \cdots & y_{L-1} \\ y_1 & y_2 & \cdots & y_L \\ \vdots & \vdots & \vdots & \vdots \\ y_{N-L-1} & y_{N-L} & \cdots & y_{N-2} \end{bmatrix} \text{, and} \quad Y_2 = \begin{bmatrix} y_1 & y_2 & \cdots & y_L \\ y_2 & y_3 & \cdots & y_{L+1} \\ \vdots & \vdots & \vdots & \vdots \\ y_{N-L} & y_{N-L+1} & \cdots & y_{N-1} \end{bmatrix}, \tag{3.2}$$

where $M \le L \le N-M$. For the efficient noise filtering, the parameter L is chosen between $N/3$ and $N/2$.

One can use the singular value decomposition (SVD) [86] of Y_1 as follows:

$$Y_1 = UDV^H \ , \tag{3.3}$$

where the superscript H denotes the conjugate transpose of a matrix, D is a diagonal matrix containing the singular values, U and V are matrices of left and right singular vectors, respectively.

The singular value decomposition (SVD) is the algorithm for computing the singular value decomposition of an arbitrary matrix . The objective of the algorithm is to find orthogonal matrices U and V so that : $U^T AV = \Sigma$, where T denotes the transpose of a matrix and Σ is a diagonal matrix. There are two steps in the algorithm.

The first step is the reduction of A to a bidiagonal form, which is a matrix whose only nonzero elements are on the diagonal and the first superdiagonal. In the second step, an iterative process is needed to reduce the superdiagonal elements to a negligible size and attain the desired diagonal matrix [87].

Then, the poles z_i s can be determined by the eigenvalue problem for the asymmetric $M \times M$ matrix Z_E, which means that z_i s contain the eigenvalues of matrix Z_E:

$$\mathrm{Z_E} = \mathrm{D^{-1}U^H Y_2 V} \quad . \tag{3.4}$$

Once M and z_i s are known, the residues R_i s are solved from the following least-squares problem:

$$\begin{bmatrix} y_0 \\ y_1 \\ \vdots \\ y_{N-1} \end{bmatrix} = \begin{bmatrix} 1 & 1 & \cdots & 1 \\ z_1 & z_2 & \cdots & z_M \\ \vdots & \vdots & \vdots & \vdots \\ z_1^{N-1} & z_2^{N-1} & \cdots & z_M^{N-1} \end{bmatrix} \begin{bmatrix} R_1 \\ R_2 \\ \vdots \\ R_M \end{bmatrix} . \tag{3.5}$$

M is determined by the ratio of the various singular values to the largest singular value. Those singular values beyond M are set equal to zero. The details for determination of M are as follows :

The singular value σ_c is selected based on the following equation: $\frac{\sigma_c}{\sigma_{\max}} \geq 10^{-p}$, where p is the number of significant decimal digits in the data. If the data is accurate up to 3 significant digits, then set p=3. On the other hand, if $\frac{\sigma_c}{\sigma_{\max}}$ is not a decreasing function, it is not appropriate to model the given data by a sum of complex exponentials. Hence, the magnitude of the singular values provides a sanity check.

For efficient noise filtering, the parameter L is chosen between $N/3$ to $N/2$. For these values of L, the variance due to noise in the parameter of z_i, has been found to be minimum. In our method, N=80 and L is selected as 30.

3.2 Determination of Extrinsic Element Values from the Set of Complex Exponentials

Similar to [88], the set of complex exponentials is used to approximate the initial values of the extrinsic elements for the iterative determination of the equivalent circuit. The measurement frequency range is from 0.2GHz to 18GHz. The frequency step (Δf) is taken as 0.2GHz. The total sampled data number is 90, and the angular frequency is related to the sampling point by

$$\omega_k = 2\pi \cdot \Delta f \cdot k \ , \tag{3.6}$$

where k denotes the k th sampling point, and ω_k is the k th sampling point in the angular frequency.

Following the GPOF method, we obtain various residues and poles to express the S-parameters as the sum of complex exponentials. Figures 3.1 to 3.4 show the comparison between the measured and calculated S-parameters. The solid lines indicate the measured values and circles indicate the calculated values by the sum of complex exponentials by using GPOF method. From our observations, the selection of M is very important, because it determines the differences between measured and calculated values. With suitable values for M , the GPOF method can provide a good fit to the measured S-parameters. For clarity, Table 3.1 is given to show the RMS error between measured and calculated S-parameters by using the GPOF method.

Table 3.1 The RMS error between measured and calculated S-parameters by using the GPOF method

	RMS Error (%)
Real (S_{11})	1.28
Imag (S_{11})	1.03
Real (S_{12})	1.20
Imag (S_{12})	1.18
Real (S_{21})	1.21
Imag (S_{21})	1.11
Real (S_{22})	1.26
Imag (S_{22})	1.01

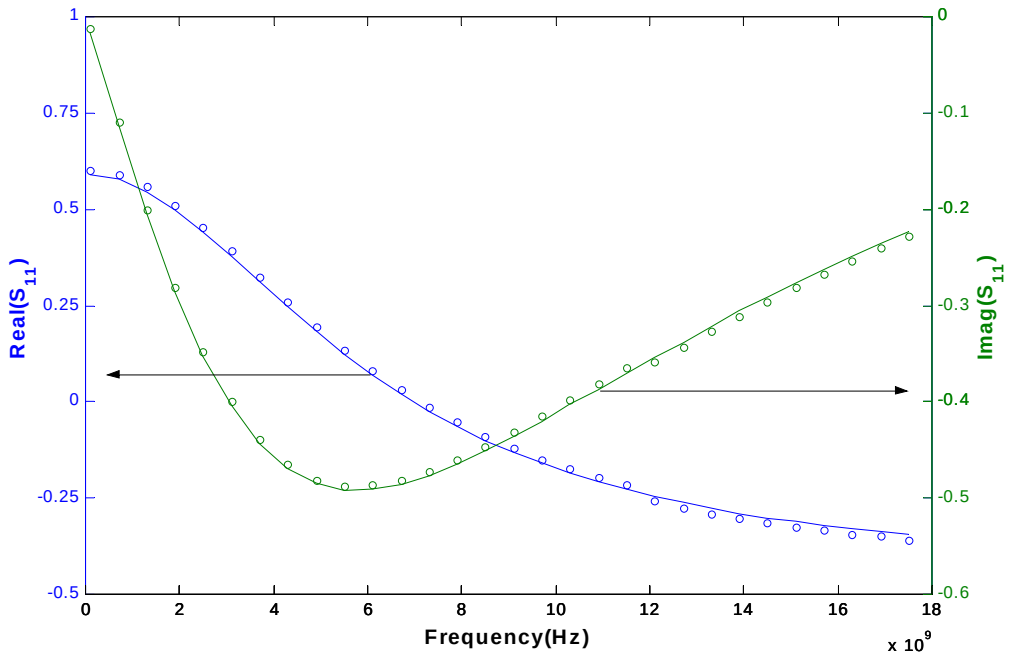

Figure 3.1. Real and imaginary parts of S_{11} . Solid lines indicate measured values and circles indicate calculated values using GPOF method.

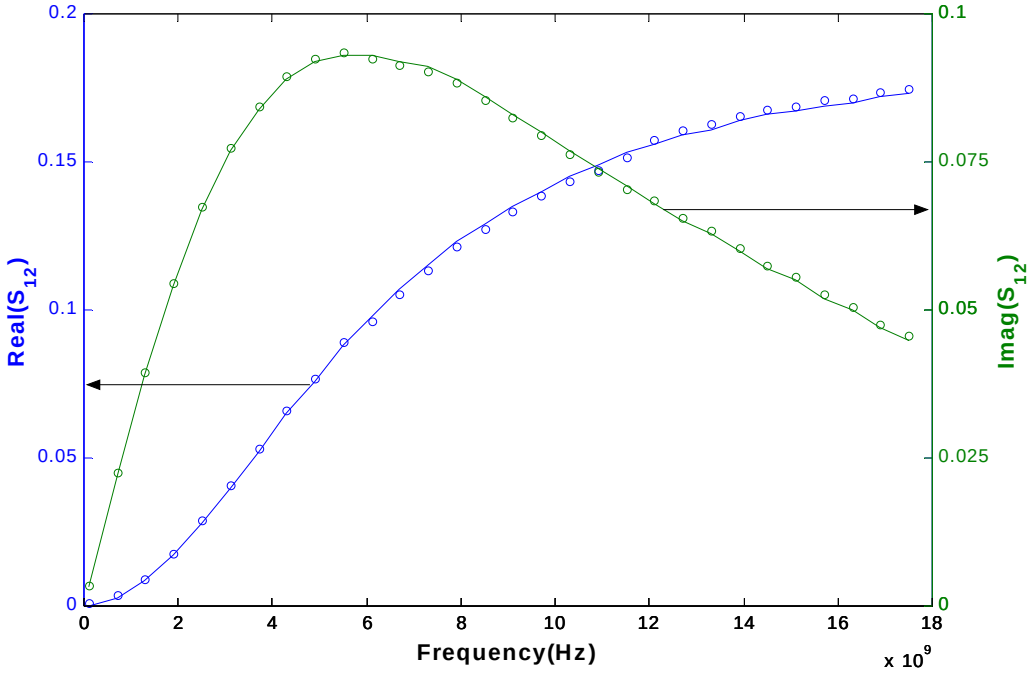

Figure 3.2. Real and imaginary parts of S_{12} . Solid lines indicate measured values and circles indicate calculated values using GPOF method.

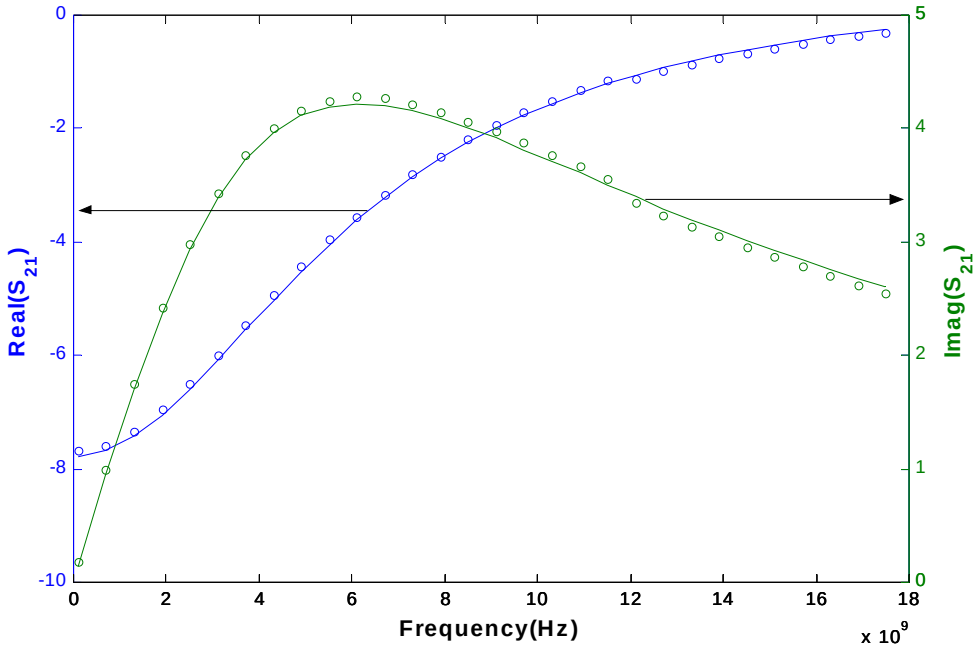

Figure 3.3. Real and imaginary parts of S_{21} . Solid lines indicate measured values and circles indicate calculated values using GPOF method.

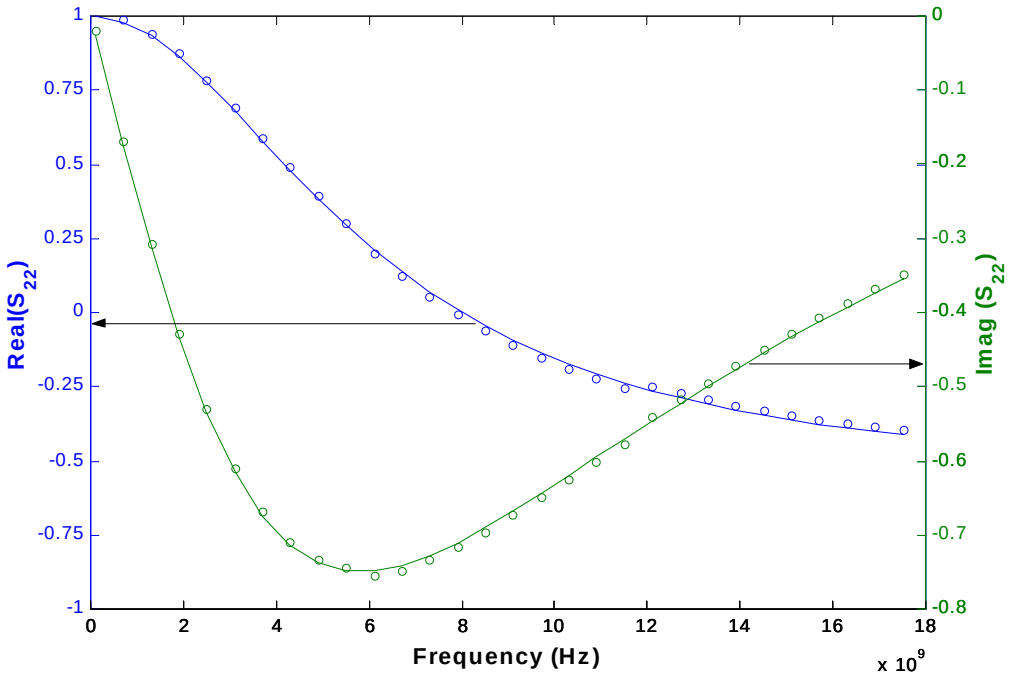

Figure 3.4. Real and imaginary parts of S_{22} . Solid lines indicate measured values and circles indicate calculated values using GPOF method.

The total S-parameters are then converted to the Z-parameters. According to equations (2.1) to (2.10), the expressions for $\mathrm{Re}(Z_{11}^{total} - Z_{12}^{total})$, $\mathrm{Im}(Z_{11}^{total} - Z_{12}^{total})$ and $\mathrm{Re}(Z_{22}^{total} - Z_{21}^{total})$ are given as:

$$\mathrm{Re}(Z_{11k}^{total} - Z_{12k}^{total}) = g_1(\omega_k) = \frac{(C_{ex} + C_{bc})R_b C_{bc}}{(C_{ex} + C_{bc})^2 + \omega_k^2 (R_b C_{bc} C_{ex})^2} + R_B \ , \qquad (3.7a)$$

$$\mathrm{Im}(Z_{11k}^{total} - Z_{12k}^{total}) = g_2(\omega_k) = \frac{-\omega_k R_b^2 C_{bc}^2 C_{ex}}{(C_{ex} + C_{bc})^2 + \omega_k^2 (R_b C_{bc} C_{ex})^2} + \omega_k L_B \ , \qquad (3.7b)$$

$$\mathrm{Re}(Z_{22k}^{total} - Z_{21k}^{total}) = g_3(\omega_k) = \frac{-R_b C_{bc} C_{ex}}{(C_{ex} + C_{bc})^2 + \omega_k^2 (R_b C_{bc} C_{ex})^2} + R_C \ . \qquad (3.7c)$$

By approximating $\mathrm{Re}(Z_{11k}^{total} - Z_{12k}^{total})$, $\mathrm{Im}(Z_{11k}^{total} - Z_{12k}^{total})$ and $\mathrm{Re}(Z_{22k}^{total} - Z_{21k}^{total})$ individually as the sum of complex exponentials , namely, $f_1(k), f_2(k)$ and $f_3(k)$, we have :

$$\mathrm{Re}(Z_{11k}^{total} - Z_{12k}^{total}) = f_1(k) = \sum_{i=1}^{M_1} R_i z_i^k \quad , \tag{3.8a}$$

$$\mathrm{Im}(Z_{11k}^{total} - Z_{12k}^{total}) = f_2(k) = \sum_{i=1}^{M_2} R_i z_i^k \quad , \tag{3.8b}$$

$$\mathrm{Re}(Z_{22k}^{total} - Z_{21k}^{total}) = f_3(k) = \sum_{i=1}^{M_3} R_i z_i^k \quad , \tag{3.8c}$$

where $M_1 = 11$, $M_2 = 10$ and $M_3 = 9$. The values of R_i and z_i for $f_1(k), f_2(k)$ and $f_3(k)$ are respectively given in Table 3.2.

Table 3.2 The calculated residues and poles for f_1, f_2 and f_3

Function	R_i	z_i
$f_1(k)$	1.3728×10	1.1521
	$1.1666\times10^{-1} \pm j1.1759\times10^{-1}$	$-8.1170\times10^{-1} \pm j2.0312\times10^{-1}$
	$-1.2312\times10^{-2} \pm j4.2263\times10^{-2}$	$-7.5074\times10^{-1} \pm j6.0473\times10^{-1}$
	$-2.9241\times10^{-1} \pm j2.9501\times10^{-1}$	$-5.0857\times10^{-1} \pm j8.5048\times10^{-1}$
	$-7.8010\times10^{-2} \pm j2.0519\times10^{-2}$	$6.5129\times10^{-1} \pm j4.2674\times10^{-1}$
	$8.8420\times10^{-1} \pm j3.3534\times10^{-2}$	$2.5667\times10^{-1} \pm j5.8600\times10^{-1}$
$f_2(k)$	2.3323	1.0253
	-2.2143	9.5853×10^{-1}
	$-9.9984\times10^{-2} \pm j4.4485\times10^{-2}$	$-1.0178 \pm j1.9442\times10^{-1}$
	$1.8587\times10^{-1} \pm j5.1330\times10^{-1}$	$5.7463\times10^{-1} \pm j9.8801\times10^{-1}$
	$3.9099\times10^{-2} \pm j7.5629\times10^{-2}$	$6.6298\times10^{-1} \pm j5.5764\times10^{-1}$
	$-8.4096\times10^{-2} \pm j9.1394\times10^{-2}$	$-4.9938\times10^{-1} \pm j4.7516\times10^{-1}$
$f_3(k)$	7.1000	1.0011
	-2.6449×10	-6.4959×10^{-1}
	7.9217	-1.3274×10^{-1}
	$2.3445\times10^{-1} \pm j2.2112\times10^{-2}$	$8.0385\times10^{-1} \pm j4.2205\times10^{-1}$
	$5.0916\times10^{-1} \pm j4.7298\times10^{-2}$	$3.7975\times10^{-1} \pm j8.0370\times10^{-1}$
	$3.4947 \pm j3.8626$	$-1.7745\times10^{-1} \pm j7.4907\times10^{-1}$

Equating equations (3.7a) to (3.7c) with equations (3.8a) to (3.8c), and assuming up to the third-order derivative continuity, the following simultaneous equations are obtained:

$$g_i(\omega_k)|_{k=0} = f_i(k)|_{k=0}\ , \qquad i=1, 2, 3 \tag{3.9a}$$

$$\frac{\partial^2 g_1(\omega_k)}{\partial^2 k}|_{k=0} = \frac{\partial^2 f_1(k)}{\partial^2 k}|_{k=0}\ , \tag{3.9b}$$

$$\frac{\partial^3 g_2(\omega_k)}{\partial^3 k}|_{k=0} = \frac{\partial^3 f_2(k)}{\partial^3 k}|_{k=0}, \tag{3.9c}$$

$$\frac{\partial^2 g_3(\omega_k)}{\partial^2 k}|_{k=0} = \frac{\partial^2 f_3(k)}{\partial^2 k}|_{k=0}. \tag{3.9d}$$

In order to obtain a high-order derivatives of $f_1(k), f_2(k)$ and $f_3(k)$, we apply the central-difference approximation method [89] with an error of order h^4. The truncation error for the first-order central-difference approximation is thus $1/30h^4 f_i^{(5)}$. Similarly, the truncation error for the second-order central-difference approximation is $1/90h^4 f_i^{(6)}$, and the truncation error for the third-order central-difference approximation is $7/120h^4 f_i^{(7)}$, where h is the step size, and $f_i^{(n)}$ (n=5,6,7) denotes the nth-order derivative of the function f_i (i=1,2,3).

Based on the equations (3.9a) to (3.9d) , by using the appropriate Taylor series expansions and the numerical differentiation approximation to obtain the high-order derivatives of $f_1(k), f_2(k)$ and $f_3(k)$, the values of R_B, L_B and R_C can be obtained. The values of R_B, L_B and R_C are found to be: $R_B = 8.012\Omega$, $L_B = 44.895pH$ and $R_C = 8.990\Omega$.

3.3 Results and Discussions

In our method, the iterative algorithm is the same as that in [76] and the analytical method for determination of intrinsic model elements is the same as that in Section 2.2. The initial values of R_B, L_B and R_C are determined as in Section 3.2 . The initial values of the three remaining extrinsic elements R_E, L_E and L_C are arbitrarily selected as: $R_E = 1.0\Omega$, $L_E = 10\,pH$ and $L_C = 20\,pH$. All the element values are updated by Levenberg-Marquardt method in the iterations.

Table 3.3 The extracted values of extrinsic and intrinsic elements

$R_E(\Omega)$	$L_E(pH)$	$R_B(\Omega)$	$L_B(pH)$	$R_C(\Omega)$	$L_C(pH)$
5.346	11.180	8.753	45.534	9.576	50.410
$R_{be}(\Omega)$	$C_{be}(pF)$	$C_{ex}(pF)$	$C_{bc}(pF)$	$R_b(\Omega)$	α_0	$\tau(ps)$
4.203	0.649	0.023	0.047	8.673	0.951	4.809

Our modeled AlGaAs/GaAs HBT contains two emitter fingers , each of which is 2μm wide and 10 μm long. The biasing condition is : I_C=15 mA , V_{CE}=3V, and the frequency range is from 0.2GHz to 18GHz. In the numerical differentiation approximation, we select the step size (h) as 0.01. The element values extracted using our technique are shown in Table 3.3. The comparison between the measured and simulated S-parameters using the proposed technique for the AlGaAs/GaAs HBT is presented in Figure 3.5. A close agreement between the measured and simulated S-parameters is noted from the figure. In the figure, crosses indicate measured values and solid lines indicate simulated values. The RMS error between simulated and measured data is found as 0.98%.

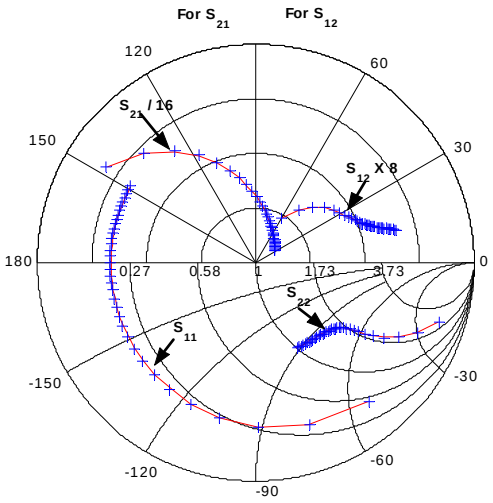

Figure 3.5. Comparison of S-parameters between measured and simulated data. Crosses indicate measured values and solid lines indicate simulated values.

In the conventional methods, the selection of the initial values sometimes affects the final results. In our new method, the reliable initial values of some extrinsic elements are determined automatically from the set of complex exponentials. Therefore, the optimization efficiency and accuracy are improved greatly. As compared with a pure optimization process, our optimization process based on the GPOF method can result in less data manipulation and storage. Moreover, it can also lead to faster computation.

It is observed that M and *h* have some effects on the final equivalent circuit parameters and simulation results. If unsuitable M values are used, the simulation results will be poor. Table 3.4 shows the RMS errors between measured and simulated S-parameters with the different values of M and *h*. Figures 3.6 to 3.9 show the

comparison of the S-parameters between the measured and simulated data with the same values of M (M_1=11,M_2=10 and M_3=9) and the different step size (h). From these figures, it is noted that the selection of the step size has a great effect on the final simulation results. For h=0.01 and h=0.001, the extracted model element values are almost the same and excellent agreement between simulated and measured data can be obtained. However, for h=0.0001, the extracted model element values are different and the final simulation results are also different. From the observation, it is noted that the choice of a finer step size h of 0.0001 gives rise to less favorable agreement between measurement data and simulation results. The step size h has the effects on the round-off and truncation errors, which would indicate a range of h where round-off errors and truncation errors cross over and lead to an optimum value of h. The experiment results clearly show that " a finer step size h leads to less truncation errors but with increased round-off errors, and conversely".

Table 3.4 Comparison of the RMS errors (%) between simulated and measured S-parameters with the different values of M and h

	***h*=0.01**	***h*=0.001**	***h*=0.0001**
M_1=8, M_2=10, M_3=9	2.02	1.99	2.53
M_1=13, M_2=10, M_3=9	1.48	1.52	1.61
M_1=11, M_2=8, M_3=9	1.56	1.57	1.66
M_1=11, M_2=12, M_3=9	2.03	2.01	2.34
M_1=11, M_2=10, M_3=7	1.98	1.98	2.06
M_1=11, M_2=10, M_3=11	1.91	1.92	2.07
M_1=11, M_2=10, M_3=9	0.98	1.01	1.31

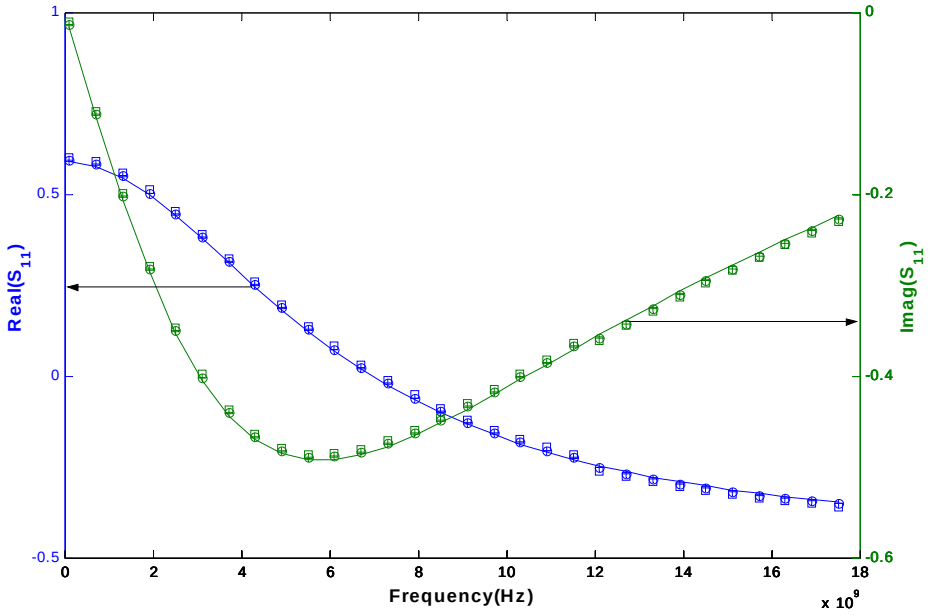

Figure 3.6. Comparison of S_{11} between measured and simulated data. Solid lines indicate measured values and others indicate calculated values using our new technique(crosses: h=0.01, circles: h=0.001 and squares: h=0.0001).

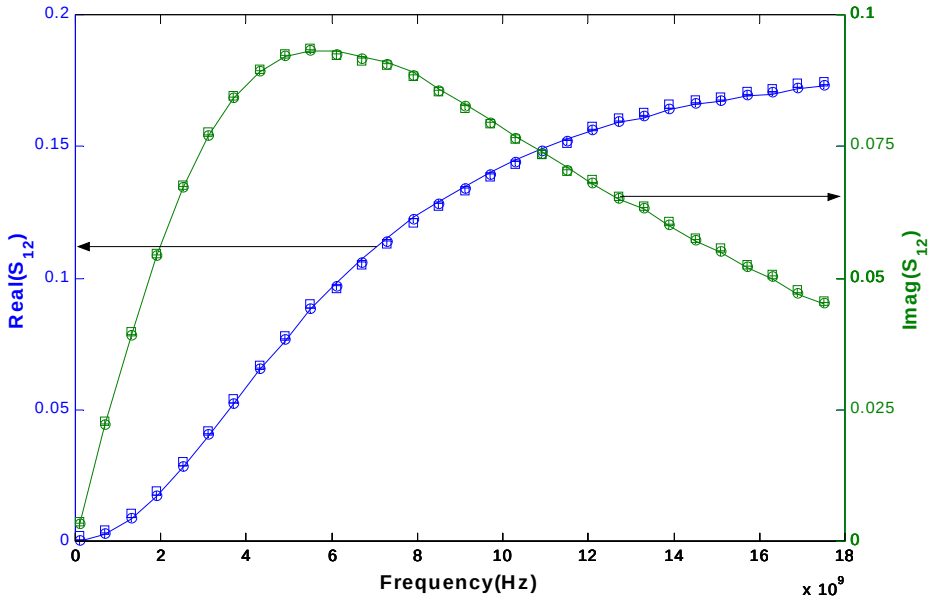

Figure 3.7. Comparison of S_{12} between measured and simulated data. Solid lines indicate measured values and others indicate calculated values using our new technique(crosses: h=0.01, circles: h=0.001 and squares: h=0.0001).

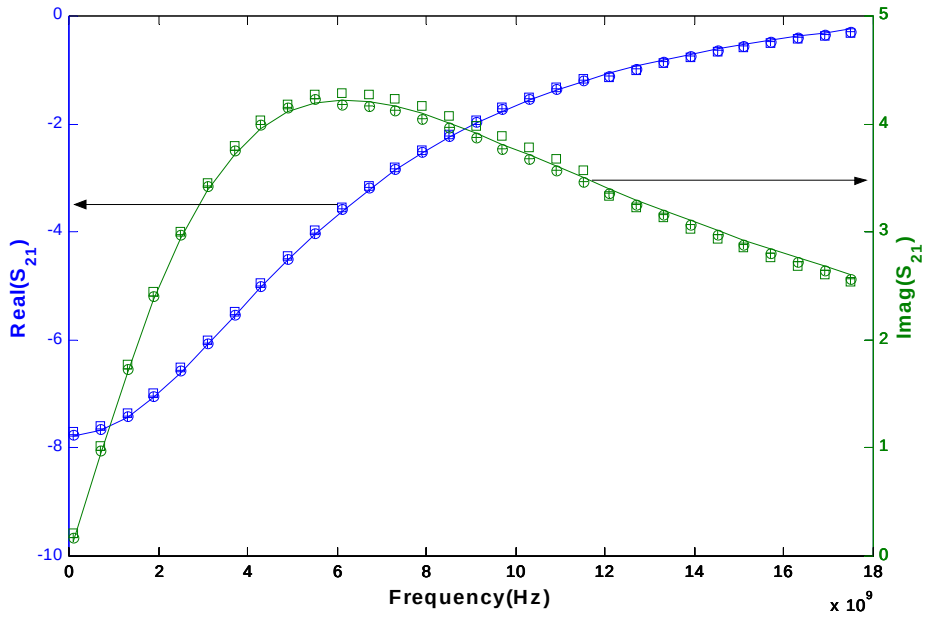

Figure 3.8. Comparison of S_{21} between measured and simulated data. Solid lines indicate measured values and others indicate calculated values using our new technique(crosses: h=0.01, circles: h=0.001 and squares: h=0.0001).

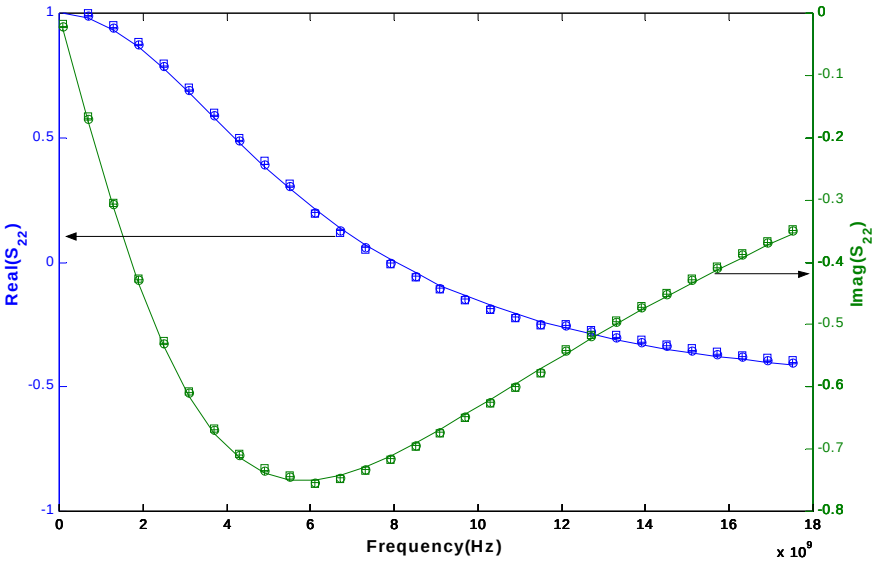

Figure 3.9. Comparison of S_{22} between measured and simulated data. Solid lines indicate measured values and others indicate calculated values using our new technique(crosses: h=0.01, circles: h=0.001 and squares: h=0.0001).

3.4 Conclusion

A novel approach for the HBT small-signal equivalent circuit parameters extraction has been introduced. A new technique for describing the high-frequency behaviour of microwave devices by using a set of complex exponentials based on the generalized pencil-of-function (GPOF) method is proposed. An excellent agreement between the measured and simulated values has been achieved. The GPOF method has also been applied to give approximate initial values of the extrinsic elements for the iterative determination of the equivalent circuit. Reliable extrinsic element values have been successfully extracted.

CHAPTER 4

THE DISTRIBUTED HBT SMALL-SIGNAL MODEL

In recent years, the increasing demands for high performance communication systems require MMICs to operate at higher frequencies. With a continuous pressure toward low cost microwave communication products, this has eventually led to a continuous increase of integration density of MMICs. Meanwhile, with this increase of operating frequencies for MMICs, a more complete and accurate millimeter-wave active device modeling is thus needed. The increase of operating frequencies will make the geometry of the millimeter-wave active devices more compatible with the wavelength. As such, wave propagation and electromagnetic interaction must be included in the model in order to account for their important influences on the device's electrical performance [37]. The increase in integration density of MMICs also adversely affects the device's normal electrical performance. The unwanted effects, such as the electromagnetic coupling and the unintended radiation, must be accurately modeled at higher frequencies.

In practical MMIC design, the task to accurately predict actual behaviors of these microwave active devices with large layout structure and operating at millimeter-wave frequencies is very crucial and challenging. A distributed characterization of the active device geometry is thus inevitable . In addition, the robust scaling ability of the microwave active devices should be investigated in order to provide the accurate

behaviors of the microwave active devices as a function of their layout sizes and finger numbers. The reduction of cost and time in MMIC development is imperative and always requires that the MMIC performance be optimized efficiently to meet the circuit specifications in a reasonably short time. Therefore, a good active device modeling method for MMIC design should provide the designers the ability to optimize the metallic layouts or finger numbers of the active devices without any geometric limitations.

Different distributed microwave active device models were proposed in the literature to take into account the inherent electromagnetic wave effects. Several global microwave active device models have been proposed, which have robust prediction and optimization capabilities. Some authors [90]-[91] have developed distributed semiconductor device models which have combined complex semiconductor transport models with full-wave solution of Maxwell's equations. The key aspect of such a modeling method is how to couple Maxwell's equations with the semiconductor hydrodynamic equations. Several techniques such as FDTD method [92] have been adopted to solve this problem. Another approach for the distributed model is to present the active device area studied as a cascade of elementary cells, which are connected with lumped passive networks [93]-[94]. This method is applicable to MMIC CAD and can include electromagnetic signal propagation along the device passive structure. A hybrid method that consists of the integration of the equivalent circuit model and the full-wave model has also been proposed in [38]-[40], [95]-[96]. In such a method, a commercial electromagnetic simulator is adopted to analyse the complex electromagnetic phenomena of the device extrinsic passive part, while the equivalent circuit is used to describe the linear or nonlinear behavior of the device intrinsic active part. The most important aspect of this method is that the

measured data, the electromagnetic simulation results and the scattering parameters of the intrinsic active part are linked through matrix manipulations.

With the continuous improvements of MMICs, one of the new trends for the simulation of complex microwave structures is the “global approach” [92], [97], which couples an electromagnetic analysis and a microwave circuit simulation. Similarly, a new concept, termed the “global modeling”[90], which is related to the active device modeling for MMIC design, has been highlighted and studied continuously. In order to overcome the dilemma brought by various conventional device modeling methods and apply the new concept of “ global modeling”, we propose a global and complete approach to characterize the small-signal performance of HBTs. Regarding the trade-off between simulation accuracy and program development efficiency, we use MoM method in a commercial software, such as IE3D, to rigorously characterize the HBT extrinsic domain. A “multi-port connection method” [50] is subsequently applied to link the scattering parameters of the extrinsic and intrinsic domains. Next, an equivalent circuit element extraction technique for determining the intrinsic small-signal model elements is developed. A comparison of the S-parameters between the measured and simulated data has shown good agreement by using our proposed technique. Moreover, it has been proven that our new method is able to accurately predict the unknown electrical responses of the other new HBT transistors which differ in device geometry.

The main objectives of our proposed model are to enhance model synthesis capability and to raise accuracy of model fitting performance. The accuracy of our modeling method should enable the inclusion of actual HBT transistor metallic topology, material parameters and the losses in the dielectric and metallization. Due to the scaling capability of our model, the actual performance of some new large-sized

HBT transistors can be predicted. Furthermore, optimization ability of our method should provide MMIC designers more freedoms to choose HBT transistors with arbitrary device geometry, which can be separately adjusted and simulated without any geometric limitation.

4.1 Basic Structure of the HBT Distributed Model

According to Figure 4.1, the distributed HBT small-signal model is divided into extrinsic passive and intrinsic active parts. Extrinsic part includes all the HBT metallic structure. The intrinsic part refers to several active elementary cells to model the semiconductor electrical behaviors of the device fingers. The intrinsic part is interconnected with the extrinsic part by means of some internal ports , i.e., "local access points" [38]. In our method, the extrinsic passive structure of a HBT transistor is characterized in terms of multi-port S-parameters, instead of the conventional lumped element approach, by means of a global full-wave electromagnetic simulation. For the first time, through the "multi-port connection method" [50], the S-parameters of each active elementary cell can be derived. Finally, based on a hybrid-π HBT small-signal equivalent circuit , all the HBT's small-signal model elements can be extracted by using various analytical expressions as shown from equations (4.8) to (4.24).

4.2 Electromagnetic Analysis of Extrinsic Part of the HBT

Similar to [39]-[40], in our method, IE3D has been used to obtain the S-matrix for the extrinsic part of the HBT structure, which can replace the lumped extrinsic elements. In this way, both parasitic capacitances and inductances related to the internal access points and connection lines have been naturally taken into account. As in Figure 4.1,

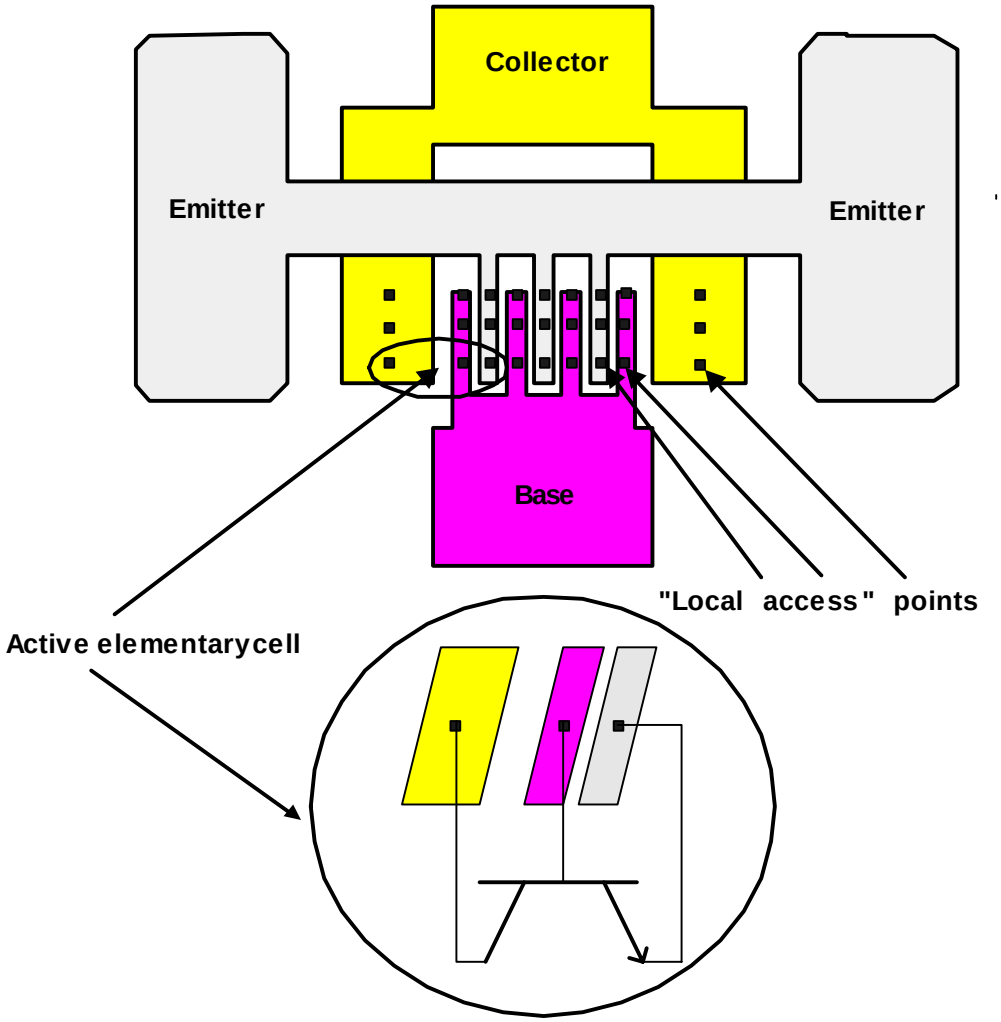

Figure 4.1. A typical HBT transistor layout ,active elementary cell and local access points.

each active elementary cell (AEC) is formed by three " local access points" placed on the emitter, base and collector electrodes for the same transistor finger group. Moreover, each of the AECs is characterized by the same lumped-element equivalent circuit model. In order to connect the electromagnetic simulation results with the small-signal model of the active elementary cell, "local access points" in each device finger must be included in the device layout for electromagnetic simulation. Therefore, the S-matrix calculated by electromagnetic simulation must include the general input

/output terminals and all the "local access points". In Figure 4.2, ports 1 and 2 are the general input and output terminals for the whole HBT transistor. Ports 3, 3' … and 2n+2, 2n+2' are different "local access points" for the following analysis procedures, where n is the number of AECs.

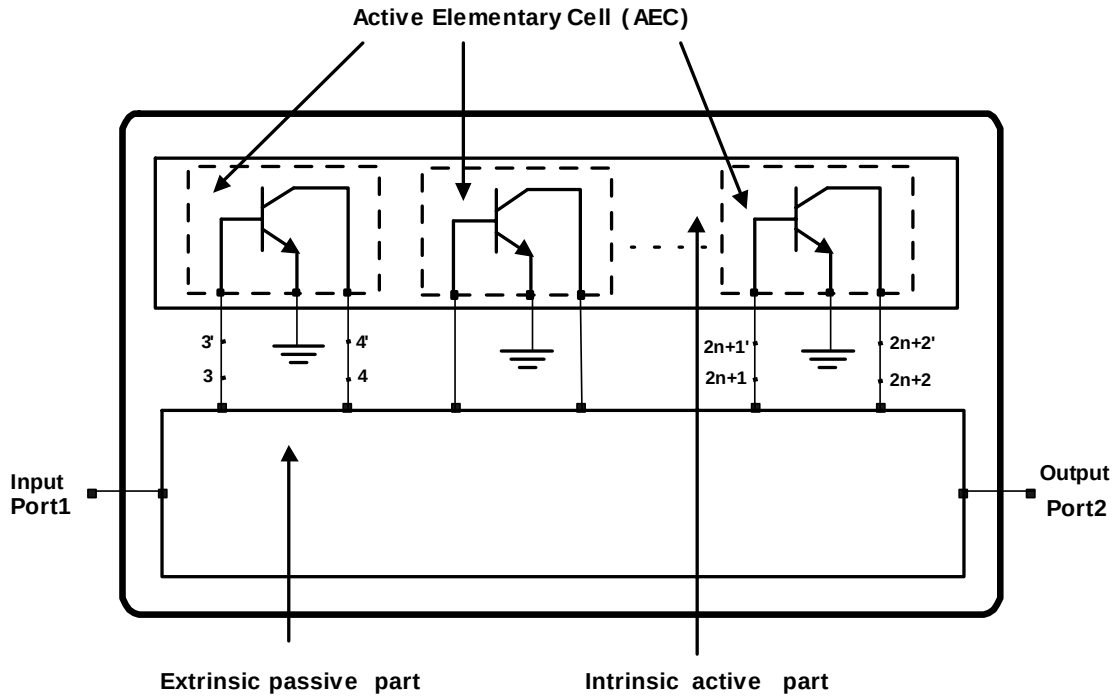

Figure 4.2. A HBT transistor with n active elementary cells (AECs) representing n emitter fingers.

In our method, the HBT passive structure is characterized through its scattering matrix S_{EM} , which is computed by means of electromagnetic simulation on the basis of device geometry and material parameters. Thus, electromagnetic propagation and coupling effects are considered for the passive structure. All the active elementary cells are described by the same scattering matrix S and the same electrical model, which can be identified once the HBT transistor total scattering matrix S_M has been measured. So, if a_i and b_i are the incident and reflected waves at the ith port (i = 1, 2 …, 2n+1, 2n+2 , 3',4'…, 2n+1', 2n+2') , we have:

$$\begin{bmatrix} b_1 \\ b_2 \\ : \\ : \\ b_{2n+1} \\ b_{2n+2} \end{bmatrix} = S_{EM} \begin{bmatrix} a_1 \\ a_2 \\ : \\ : \\ a_{2n+1} \\ a_{2n+2} \end{bmatrix}, \qquad \begin{bmatrix} b_1 \\ b_2 \end{bmatrix} = S_M \begin{bmatrix} a_1 \\ a_2 \end{bmatrix}, \quad \begin{bmatrix} b_{(2n+1)'} \\ b_{(2n+2)'} \end{bmatrix} = S \begin{bmatrix} a_{(2n+1)'} \\ a_{(2n+2)'} \end{bmatrix}, \qquad (4.1)$$

where

$$S_{EM} = \begin{bmatrix} S_{EMA} & S_{EMB} \\ S_{EMC} & S_{EMD} \end{bmatrix}, S_M = \begin{bmatrix} S_{M11} & S_{M12} \\ S_{M21} & S_{M22} \end{bmatrix}, \quad \text{and } S = \begin{bmatrix} S_{11} & S_{12} \\ S_{21} & S_{22} \end{bmatrix}. \qquad (4.2)$$

The matrices S_{EMA} , S_{EMB} , S_{EMC} and S_{EMD} are obtained by the matrix decomposition of S_{EM} . The dimension of S_{EMA} is 2 by 2, S_{EMB} is 2 by 2n , S_{EMC} is 2n by 2 and S_{EMD} is 2n by 2n.

Through the "multi-port connection method" [50], we have :

$$\begin{bmatrix} b_p \\ b_c \end{bmatrix} = \begin{bmatrix} S_{pp} & S_{pc} \\ S_{cp} & S_{cc} \end{bmatrix} \begin{bmatrix} a_p \\ a_c \end{bmatrix}, \qquad (4.3)$$

where

$$b_p = \begin{bmatrix} b_1 \\ b_2 \end{bmatrix}, \qquad b_c = \begin{bmatrix} b_3 \\ : \\ b_{2n+2} \\ b_{3'} \\ : \\ b_{(2n+2)'} \end{bmatrix}, \qquad a_p = \begin{bmatrix} a_1 \\ a_2 \end{bmatrix}, \qquad a_c = \begin{bmatrix} a_3 \\ : \\ a_{2n+2} \\ a_{3'} \\ : \\ a_{(2n+2)'} \end{bmatrix}, \qquad (4.4)$$

$$S_{pp} = S_{EMA}, \quad S_{pc} = \begin{bmatrix} S_{EMB} & 0 \end{bmatrix}, \quad S_{cp} = \begin{bmatrix} S_{EMC} \\ 0 \end{bmatrix}, \quad S_{cc} = \begin{bmatrix} S_{EMD} & 0 \\ 0 & S_T \end{bmatrix}, \tag{4.5}$$

and

$$S_T = \begin{bmatrix} S & & & & & \\ & \ddots & & & & \\ & & S & & & \\ & & & S & & \\ & & & & \ddots & \\ & & & & & S \end{bmatrix}, \quad \begin{bmatrix} b_3 \\ \vdots \\ b_{(2n+2)} \\ b_{3'} \\ \vdots \\ b_{(2n+2)'} \end{bmatrix} = \Gamma \begin{bmatrix} a_3 \\ \vdots \\ a_{(2n+2)} \\ a_{3'} \\ \vdots \\ a_{(2n+2)'} \end{bmatrix}, \quad \Gamma = \begin{bmatrix} 0 & I \\ I & 0 \end{bmatrix}, \tag{4.6}$$

in here, I is an identity matrix with dimension of 2n by 2n.

Finally, we have

$$S_p = S_M = S_{pp} + S_{pc}(\Gamma - S_{cc})^{-1} S_{cp} \ . \tag{4.7}$$

Based on equations (4.1) to (4.7), we can derive the scattering matrix, S, for the intrinsic active part of the HBT at each frequency point.

4.3 Extraction Methodology for Intrinsic Active Part of the HBT Transistor

A standard hybrid-π equivalent circuit for bipolar transistor small-signal modeling is modified to describe the electrical response of the intrinsic active part of a HBT transistor . Several explicit analytical expressions are derived, which can be used to determine all the intrinsic model elements.

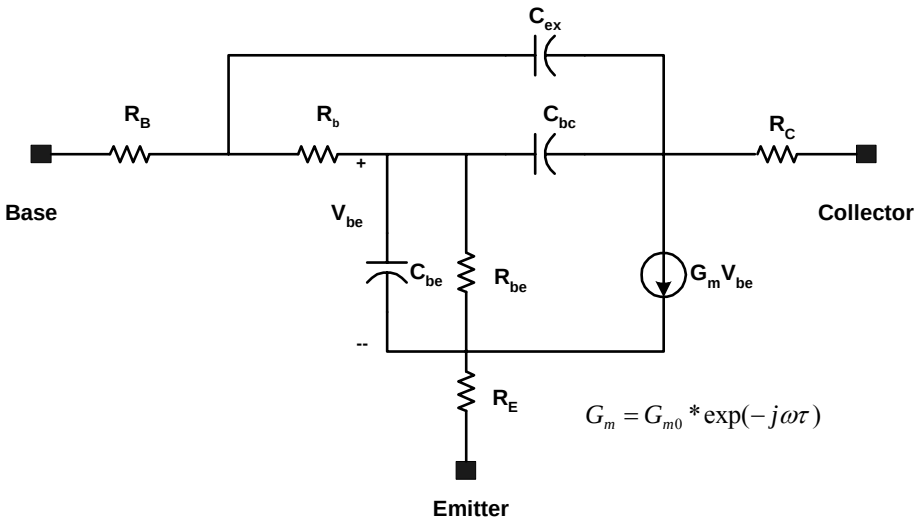

Figure 4.3. A hybrid -π equivalent circuit for HBT small-signal modeling.

Figure 4.3 shows the typical hybrid-π equivalent circuit for HBT small-signal modeling. In the equivalent circuit, only emitter resistance R_E, external base resistance R_B and collector resistance R_C have been included as extrinsic model elements. The other parasitic inductances and capacitances in the conventional equivalent circuit have been fully taken into account by full-wave electromagnetic simulation [38]. Based on the equivalent circuit we have adopted, we can determine all the Z-parameters as follows [68]:

$$Z_{11} = \frac{R_b Z_1}{R_b + Z_1 + Z_2} + \frac{R_b Z_2}{(1 + G_m Z_3)(R_b + Z_1 + Z_2)} + \frac{Z_3}{1 + G_m Z_3} + R_B + R_E , \qquad (4.8)$$

$$Z_{12} = \frac{R_b Z_2}{(1 + G_m Z_3)(R_b + Z_1 + Z_2)} + \frac{Z_3}{1 + G_m Z_3} + R_E \quad , \qquad (4.9)$$

$$Z_{21} = \frac{R_b Z_2 - G_m Z_3 Z_1 Z_2}{(1 + G_m Z_3)(R_b + Z_1 + Z_2)} + \frac{Z_3}{1 + G_m Z_3} + R_E \ , \qquad (4.10)$$

$$Z_{22} = \frac{R_b Z_2 + Z_1 Z_2}{(1 + G_m Z_3)(R_b + Z_1 + Z_2)} + \frac{Z_3}{1 + G_m Z_3} + R_C + R_E \ , \qquad (4.11)$$

where

$$Z_1 = \frac{1}{j\omega C_{ex}} \quad , \qquad Z_2 = \frac{1}{j\omega C_{bc}} \qquad \text{and} \quad Z_3 = R_{be}\left(\frac{1 - j\omega C_{be} R_{be}}{1 + \omega^2 C_{be}^2 R_{be}^2}\right). \tag{4.12}$$

Let

$$A = Z_{11} - Z_{12} \ , \qquad B = Z_{22} - Z_{21}, \qquad C = Z_{11} + Z_{22} - Z_{12} - Z_{21} \ ,$$

and

$$D = Z_{11} + Z_{21} - Z_{12} - Z_{22}\,. \tag{4.13}$$

Thus,

$$\mathrm{Re}(C) - R_B - R_C = (R_B - \mathrm{Re}(D) - R_C) + 2\omega R_b C_{bc}\ \mathrm{Im}(D)\,, \tag{4.14}$$

$$\mathrm{Im}(C) = -2\omega R_b C_{bc}\,(\mathrm{Re}(D) + R_C - R_B) - \mathrm{Im}(D)\,, \tag{4.15}$$

$$\mathrm{Re}(A) - R_B = -\omega\,\mathrm{Im}(B) R_b C_{bc}\,, \tag{4.16}$$

$$\mathrm{Im}(A) = [\mathrm{Re}(B) - R_C][\omega R_b C_{bc}]\,, \tag{4.17}$$

$$[\mathrm{Re(C)} + \mathrm{Re(D)} - 2\mathrm{R_B}][\mathrm{Re(D)} - \mathrm{R_B} + \mathrm{R_C}] = -\mathrm{Im(D)}[\mathrm{Im(C)} + \mathrm{Im(D)}], \tag{4.18}$$

and

$$R_B = \mathrm{Re}(A) + \frac{\mathrm{Im}(A)\cdot \mathrm{Im}(B)}{\mathrm{Re}(B) - R_C}\ . \tag{4.19}$$

From equation (4.14) to (4.19), we can obtain the values of R_B and R_C .

In addition, we have :

$$\frac{C_{bc} R_b}{(C_{ex} + C_{bc})} + R_B = \mathrm{Re}(A) \ , \qquad \frac{-\omega R_b^2 C_{ex} C_{bc}^2}{(C_{ex} + C_{bc})^2} = \mathrm{Im}(A)\,, \tag{4.20}$$

and

$$\frac{-C_{bc} C_{ex} R_b}{(C_{bc} + C_{ex})^2} + R_C = \mathrm{Re}(B) \ , \qquad \frac{-1}{\omega(C_{bc} + C_{ex})} = \mathrm{Im}(B)\,. \tag{4.21}$$

From equations (4.20) and (4.21), we can obtain the values of R_b, C_{ex} and C_{bc} .

In the small-signal transistor operating condition, we have from [4]:

$$G_{m0} = \frac{qI_c}{KT} \quad , \qquad R_{be} = \frac{\beta}{G_{m0}} \quad . \tag{4.22}$$

Therefore, we can obtain the values of C_{be}, G_m and R_E, then

$$G_m = G_{m0} \exp(-j\omega\tau), \tag{4.23}$$

and

$$\tau = -\frac{1}{\omega} tg^{-1}[\frac{\mathrm{Im}(G_m / G_{m0})}{\mathrm{Re}(G_m / G_{m0})}]. \tag{4.24}$$

The relation between extracted G_{m0} and frequencies is shown in Figure 4.4.

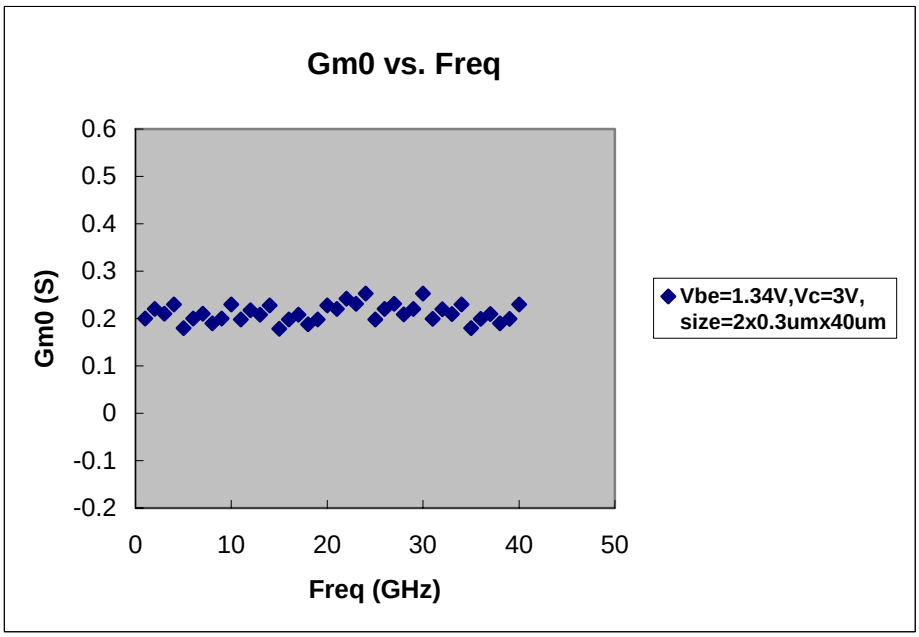

Figure 4.4. The relation between extracted G_{m0} and frequencies.

4.4 Model Verifications and Discussions

AlGaAs/GaAs HBTs with different structures were measured and simulated to validate the proposed approach. The S-parameters of HBTs were measured directly on-wafer at frequencies up to 40GHz using a pulse modulated measurement and modeling system and the biasing condition is V_{BE}=1.34V , V_{CE}=3V. Through the geometric

parameters of the device GDS files provided by the foundry, the scattering matrices of the extrinsic passive structures were computed by using the IE3D electromagnetic simulator. In order to calculate the S-matrix of each active elementary cell, MATLAB programs have been developed by using the calculation method in Section 4.2. The analytical equations in Section 4.3 have been used to derive the values for all the small-signal model elements. Finally, the simulation in the frequency domain was implemented by using the Agilent-ADS simulator.

First, in order to check the fitting performance of our distributed model, we chose HBT transistors with two different structures, whose emitter sizes are 2×3μm×20μm and 2×3μm×40μm. Figures 4.5 to 4.6 are the comparisons between the measured S-parameters and the simulated results. From these figures, it can be seen that a relatively good agreement between measured and simulated data can be achieved. However, it can be observed that the differences between simulated and measured values of S_{11} and S_{22} are larger than those of S_{12} and S_{21}. Several possible reasons for such discrepancies will be discussed in the following paragraph of this section.

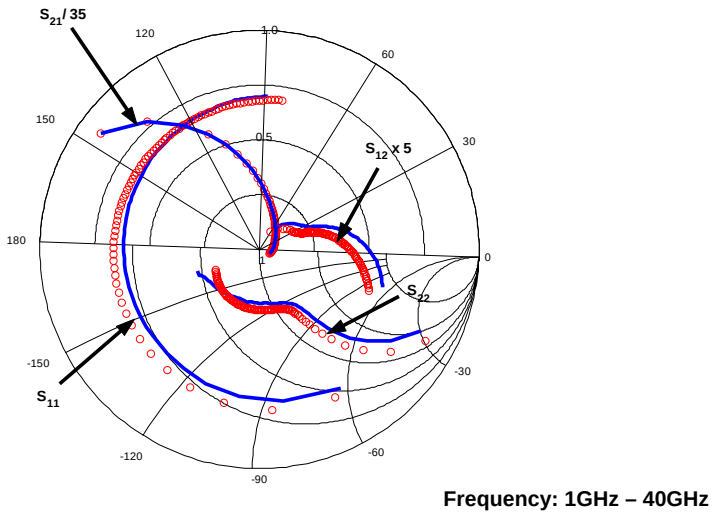

Figure 4.5. Measured (circle) and simulated(solid) S-parameters for HBT(2×3μm×20μm).

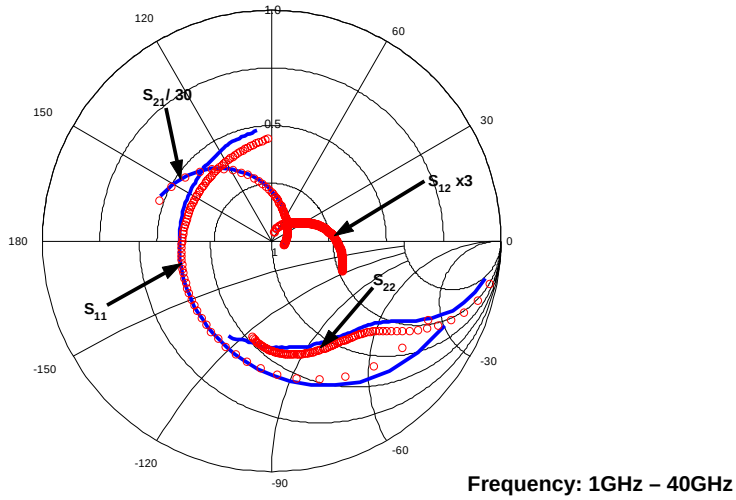

Figure 4.6. Measured (circle) and simulated(solid) S-parameters for HBT(2×3μm×40μm).

In order to check the actual scaling capability of our proposed modeling method, the model was adopted to predict the actual electrical behaviors of various HBT transistors, which are different from those used in the previous steps. The prediction was carried out on the basis of the model element values of active elementary cells which are already known. Figures 4.7 to 4.8 show the measured and predicted S-parameters for the HBTs (4×3μm×40μm and 6×3μm×40μm). The prediction above was carried out on the basis of known active elementary cell of the HBT whose size is 2×3μm×40μm. From these figures, the prediction and synthesis capabilities of our proposed model can be verified.

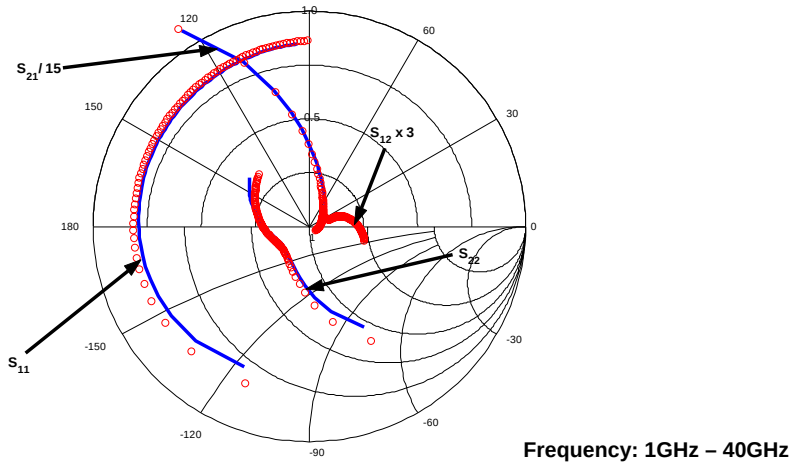

Figure 4.7. Measured (circle) and simulated(solid) S-parameters for HBT (4×3μm×40μm).

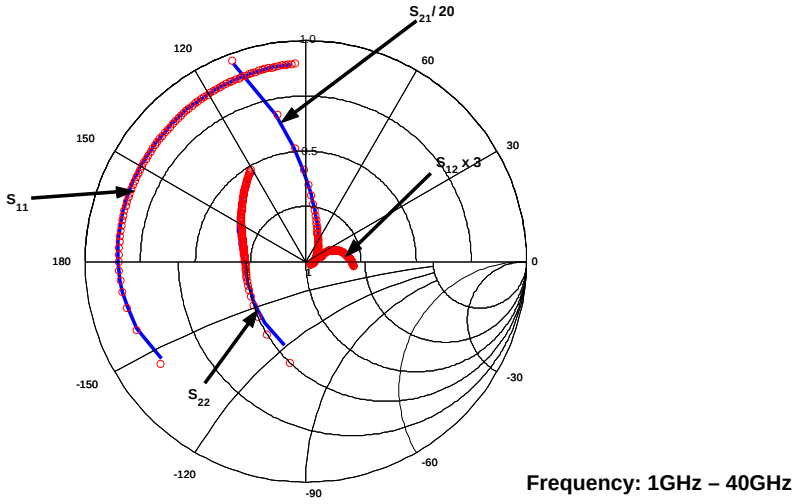

Figure 4.8. Measured (circle) and simulated (solid) S-parameters for HBT(6×3μm×40μm).

In short, the model is simplified. Factors not considered are as follows: (a) It is assumed that an isotropic semi-insulating GaAs substrate is located under the transistor metal structure; (b) The effect of current flow on the electromagnetic field distribution under the transistor passive structure has been omitted; (c) The effects of emitter grounding via holes and metal losses on the simulation results need to be investigated further; (d) One reference plane for AECs has been assumed and the finger structure of

the transistor has been simplified [39], [40]. One of the reasons for selecting one "local access point" along the device finger is for simplicity in our analysis. Besides, for those studied HBTs, the transverse dimension of the finger is generally small and the longitudinal length of the finger is short compared with the wavelength.

Our proposed method is based on the electromagnetic simulation of metallic parts of the device and biased S-parameter measurements of a HBT transistor. Then, without any optimization procedures , the S-parameters of the intrinsic part of the transistor are calculated by using an analytical method and relevant derived equations (4.8) to (4.24) . In general, our method is useful especially for those large-sized HBT devices at millimeter-wave frequencies. The proposed method can provide attractive information about the transistor with arbitrary metallizations. The need for any additional database is omitted and design flexibility for the device has been enhanced. So, it is very useful for those MMIC designers to obtain accurate predictions for their various designs. Based on electromagnetic simulation, this method can be used to include complex coupling effects in the device layouts and to predict the electrical characteristics of unconventional device structures for better MMIC performance. Also, this method can be accurate enough to describe many full-wave effects which cannot be covered by the conventional admittance parasitic networks. Therefore, this method can be regarded as a preliminary step for the global and fully layout / process oriented design approach. In our proposed modeling method, actually, any linear or nonlinear description of a HBT transistor, which includes lumped or distributed equivalent elements, can be adopted.

4.5 Conclusion

In this chapter, a novel approach for the distributed modeling of millimeter-wave HBTs has been proposed, with the purpose of taking into account the various wave-effects related to transistor metallic geometry. The modeling method is based on an accurate electromagnetic simulation of the metallizations of a HBT transistor. Meanwhile, the intrinsic active part of a HBT transistor is characterized by a modified small-signal model for the bipolar transistor. The significance of our proposed modeling method is that it can provide a more comprehensive and efficient tool for transistor optimization and a more accurate performance prediction for various transistors with different layout structures.

CHAPTER 5

IMPROVED HBT LARGE-SIGNAL MODELING METHOD

The rapid advancement on MMIC CAD technology has been made in recent years. The great progress of MMIC CAD technology is strongly supported by the parallel development of accurate and practical microwave component models, especially for those microwave active device models. In Chapters 2-4, HBT small-signal modeling methods have been discussed and analyzed. In this chapter, HBT large-signal modeling will be studied. Unlike the small-signal model, only the large-signal model can include the nonlinearity information of the microwave devices. So, the large-signal model is very important in the accurate large-signal performance prediction for microwave nonlinear circuits such as power amplifiers, mixers and oscillators. In this chapter, the HBT large-signal model is classified into four groups and literature review on this issue is made. The focus in this chapter is on two of the commercial semi-physical compact HBT models: Gummel-Poon (GP) model and Vertical Bipolar Inter-Company (VBIC) model. The working principle and model parameter extraction method of the GP model will be discussed. Some improved model parameter extraction techniques will be adopted in the model development. The practical modeling experience, experimental results and the GP model verification on a single device level will be included. Based on the developed HBT GP large-signal model, a SiGe HBT high gain and high linearity amplifier will be designed, fabricated and

tested. The GP model verification on the microwave integrated circuit level will be presented.

With the constant advancement of modern bipolar transistor technology, some more advanced and comprehensive semi-physical compact models, such as VBIC, HICUM and MEXTRAM models, have been proposed. In this chapter, the objectives, advantages, major model structure and model parameter extraction methods of the VBIC model will be discussed. A new technique, namely, "local ratio evaluation", will be developed to convert some of the GP model parameters to the corresponding VBIC model parameters. Furthermore, an improved avalanche breakdown model will be recommended to describe HBT avalanche breakdown characteristics better than the conventional VBIC model.

5.1 Literature Review

When HBT models are classified according to the device operating condition, they can be grouped into small-signal and large-signal models. A number of different HBT large-signal models have existed and they can be further classified into several different categories. According to the main model development methods, large-signal models can be classified into: physical model, semi-physical compact model, empirical model and behavioral model.

5.1.1 Physical Model

The derivation of the equations in a physical model is usually based on semiconductor device physics and in the explicit forms. Physical models often involve the solution of a set of equations, such as Poisson's equation, the continuity equation and the drift-diffusion equation related to the current density. The main objective of a physical

model is to simulate the relation between the geometrical and constitutive properties of the device and its output characteristics. In a physical model, material and process variation can be considered simply by changing the values of the corresponding model parameters. The advantages of a physical model include (a) the model parameters usually have certain physical meanings, which can be used to check the correctness of the parameter extraction procedure, (b) the model has the prediction ability for the given device doping profiles and dimensions, (c) the geometrical scaling rule can be applied to the model with confidence, (d) the simulated small- and large- signal quantities can be correlated through the mutual dependence of several large- signal equations on the same physical and geometric parameters, (e) the model can be adopted to evaluate the effects of process variation on the device characteristics, and (f) the model can provide a deeper insight into the physical mechanisms of the semiconductor devices and a better understanding of the device performances. However, the discontinuities in the analytical expressions sometimes may cause numerical instability. Some analytical expressions derived from semiconductor device physics are only valid in a certain operating condition. Furthermore, developing a physical model often requires the complex computations and derivations of analytical expressions, which are very time and labor consuming [98].

Many authors [42], [99]-[110] have made contributions by adding the physical analyses to the HBT models. Andersson *et al.* [99] have introduced a physical but compact model for SiGe HBTs. In their model, the heterojunction device physics and the material properties of the SiGe base region were added. In this way, valence band discontinuity, heavy doping and high collector current effects could be included and the additional built-in field due to the germanium concentration gradient was also taken into account. The model only required the material and device processing

parameters, such as doping concentrations, device geometry and layer thickness. Therefore, the number of model parameters was reduced. Also, this model was comprehensive for SiGe device design and circuit simulation, because they combined the analytical model of Graaff and Kloosterman [100] with physics of SiGe material. Similar to [99], Hong *et al*. have [101] proposed a physical SiGe HBT model, which described the carrier transport and its explicit dependence on nonuniform doping density and energy gap in the HBT base region . Most of their model parameters were structure dependent and could be obtained from the device geometry and the doping profile. Because the model has been implemented in SPICE2, it was useful for predictive device simulation and circuit design. In [102] and [103], the AlGaAs/GaAs HBT's current gain, cutoff and maximum oscillation frequency versus the collector current density were analyzed and calculated. The physical-based and analytical model developed by Liou *et al.* [103] has included high current and thermal effects. Also, their model parameters are only device configuration and material properties, such as layer thickness, doping concentration and free-carrier mobility. Therefore, this model could be defined as a "pure" HBT physical model. Parikh and Lindholm [104] have analyzed the transport of carriers across the heterojunction interface and proposed a new charge-control model for single and double AlGaAs/GaAs HBTs. Their model could be applied for arbitrary doping profiles and for all levels of injection in the base region . All the authors in [105]-[107] have developed their HBT physical models in the traditional way which is similar to that in Gummel-Poon homojunction bipolar transistor model. So, their physical models are suitable for the circuit simulations. But, most of their model parameters are based on the device make-up such as the device geometry, doping concentration and layer thickness and the material parameters such as energy band gap, electron affinity and carrier diffusion coefficients. Their important

contributions to compound semiconductor materials and heterojunction device physics are the space charge region width modulation effect and the base-widening effect at large collector current.

5.1.2 Semi-Physical Compact Model

The features of the semi-physical compact model are as follows: (a) The equivalent circuit consists of some lumped elements. (b) Each element in the equivalent circuit always involves the related analytical equations , physical constants and model parameters . (c) The analytical equations can be obtained either from derivations based on semiconductor device physics , or from some empirical descriptions . (d) Most of the model parameters can be determined from device measurement [111]. Therefore, the accuracy of this model depends not only on the analytical equations , but also on the values of the model parameters. The development of this model mainly includes two objectives: one is to define the model analytical equations and the other is to extract the model parameters in a reasonable procedure. This model should be self-consistent and suitable for CAD applications. Also, important physical effects should be incorporated. The procedure for the model parameter extraction should be chosen judiciously [98].

There are some commercial models which can be classified as semi-physical compact models. Ebers-Moll model was introduced in 1954 [52]-[53], Gummel-Poon model was developed in 1970 [51], MEXTRAM model was established in 1985 [98],[112], HICUM model was proposed in 1987 [44] and VBIC was adopted in practice in 1995 [54]-[56]. Originally, the industry standard bipolar transistor model is based on the Gummel-Poon (GP) model. Though several limitations exist for the GP model, until now, no widely accepted alternative is available to replace it. Several

advanced bipolar models, such as VBIC, HICUM and MEXTRAM models have been proposed and currently under evaluation by the Compact Model Council (CMC) of Electronic Industries Association (EIA) in USA. The VBIC model, proposed by a group of people from widely representative industries, is the direct extension of GP model, while the other two models are developed independently and consistently by dedicated developers in conjunction with bipolar process developments [54]-[56].

Although the commercial semi-physical compact models have been used to simulate HBT's performance, the simulation results are not satisfactory enough, because they cannot cover and model all the complex operation phenomena and physical mechanisms of HBTs. To improve the modeling performance of all the commercial semi-physical compact modeling methods, extensive research has been done in recent years [43]-[47], [113]-[129].

Extended EM models have been used to describe the complicated performance of HBTs in [47], [113] and [114], such as transit time effect [113] and self-heating effect [47],[114]. Meanwhile, some authors have developed several improved models based on the GP model to include various important physical phenomena in HBTs, such as soft breakdown, collector transit time delay effect [127], impact ionization and kirk effect [45], [115]-[117], nonideal leakage current, thermal behavior [115]-[116], and surface recombination current [118]. Besides, [46] should be noted in that the authors combined the GP model with some elements of the VBIC and HICUM models as well as with specific extensions for the accurate modeling of SiGe HBTs. Also, efforts have been made in [43] and [45] to develop the scalable and statistical HBT large-signal models based on the GP model.

5.1.3 Empirical Model

The equations which are defined in an empirical model are also some analytical expressions, but the main purpose of their applications is curve-fitting, that is, to obtain analytical formulas that approximate existing measurement data with good accuracy and minimal complexity. Therefore, an empirical model is usually developed based on measured DC and AC characteristics. Also, an empirical model uses one set of equations to represent the most important device characteristics concisely. Each equation consists of the parameters whose values can be extracted from the existing measurement data, but these parameters may not have any physical meanings. The advantages of an empirical model include (a) it is sometimes flexible enough due to the possible adoption of some numerical optimization techniques, (b) it is compact enough and suitable for CAD applications, (c) it can provide efficient approximations and interpolations, (d) the development of it usually costs less time as compared with the physical model and requires smaller data storage as compared with the behavioral or tabular model [98]. However, an empirical model cannot provide physical insight, predictive capabilities, geometrical scaling, proper correlation between model parameters and the encapsulation of theoretical knowledge .

In the large-signal HBT empirical model of [130], the additional diodes, voltage sources and the empirical expressions for the capacitance calculation were included in the equivalent circuit. In this way, several important HBT effects, such as leakage current, thermal effect, dependence of junction depletion capacitance and transit time on collector current and variation of the effective electron barrier in an emitter heterojunction, have been taken into account for the better fit of device performance. Meanwhile, Wei *et al.* [131]-[132] have introduced the HBT large-signal empirical model with the additional voltage and current sources to include self-heating , collector transit time and RF-breakdown effects . Also, in the HBT large-signal empirical

models developed by Lu *et al.* [133]-[135], the additional temperature dependent diodes and nonlinear resistors were implemented to include the self-heating and non-uniform gain effects. Besides, the thermal interaction between emitter fingers in a multi-cell power HBT could be modeled. In addition, various other HBT large-signal empirical models have been explored, some of which can accurately model high current operation effect [48], self-heating effect [136], carrier transit and avalanche breakdown phenomena [137].

5.1.4 Behavioral Model

This type of model is based on the storage of all the measurement data or the numerical simulation results related to the electrical characteristics of a device. It is different from both physical model and empirical model which are completely based on the model "parameters". In the behavioral model, some interpolation procedures and empirical functions are still needed to ensure the data continuity . It is able to provide a curve fit even when the other physical or empirical models fail due to their fixed and predefined equations. Besides, this model can be developed in a relatively short time. But, there are some drawbacks in it. Most of behavioral models are only valid in the measurement range. Sometimes, they also require the large computer memory. Moreover, it is difficult for most of them to have the abilities of performance forecast and geometrical scaling [138], [98]. Meanwhile, this type of model is unsuitable for CAD applications.

One method in the behavioral modeling is to accurately express the measured behavior of a linear or nonlinear object with a set of equations generated from table or chart form data . Its main objective is to formulate a single closed form equation to represent a measured parameters. In this way, the measured parameter can be

expressed as a function of multiple independent variables which control the behavior of the object simultaneously. Curve fitting techniques are usually adopted to convert the measured data to the equations. The conventional curve fitting techniques are linear, logarithmic, power function, exponential and polynomial curve fitting methods. However, when these methods are used, problems often arise if the behavior of an objective is abruptly modified due to some nonlinear characteristics. So, they are inadequate for the purpose of modeling the behavior that exhibits sharp discontinuity. Spline method sometimes is used for curve fitting. But, the lack of a single equation to represent the data over the entire range of independent variables makes this technique unacceptable for behavioral modeling. Recently, "left- and right- hand functions" method [138] and "neural networks" [139]-[140] method have been developed as more efficient tools for the behavior modeling.

In recent years, "neural networks"[139]-[140] has received much attention to take the place of the conventional behavioral modeling methods such as polynomial regression and look-up table models. Furthermore, the introduction of "neural networks" method to the RF and microwave field leads to some unconventional alternatives for device modeling and circuit design problems in RF and microwave CAD applications. The applications in this field consist of microstrip circuit design, passive component and active device modeling [141]-[154].

Neural networks, also called artificial neural networks, are information processing systems inspired by the ability of the human brain to learn from observations and to generalize by abstraction. The typical applications of neural networks include control, biomedical, pattern recognition and communications, etc. The advantages of the modeling methods with neural networks are as follows [140]:

(a) Neural networks models are more accurate or flexible than polynomial regression and look-up table models . (b) It can provide multiple outputs with a single model . (c) In neural networks, no prior knowledge about the input and output mapping is required for the model development. Instead, the inherent relations between inputs and outputs can be deduced by training from the data. (d) With the neural networks, the functions for the model fitting usually can be represented by the network structures instead of the explicit definitions. (e) Because of the generalization capacity of a neural network, the new responses can be made from the new input data which have not been used for the model development . (f) A neural network is capable of providing a close approximation to any continuous linear or nonlinear mapping. This is very significant for a neural network model to be applied for an accurate and efficient RF and microwave CAD, because it can ensure the accuracy in a circuit simulator environment.

The model developed by using the neural network always involves two main parts. The first part is to establish the architectures used for constructing the neural network. A neural network has two basic components, namely, the processing element (neuron) and the connection between neurons (link). The common neural network configurations for RF and microwave modeling and design include [140] multilayer perceptrons (MLP), radial basis function (RBF) network, wavelet neural network, self-organizing maps (SOM), arbitrary structure and recurrent networks. Actually, different neural network structures are constructed by using different neurons and links. The second part is the training, which is related to the data generation, range and distribution of the samples, data splitting, data scaling, initialization of the weighting parameters and the quality measures. But the training process actually involves the algorithms for finding values of weights associated with various neurons and can be

regarded as an optimization process. The common algorithms are backpropagation, conjugate gradient, quasi-Newton, Levenberg-Marquardt, genetic algorithm and simulated annealing.

In general, when a neural network is constructed to model a microwave active device, any type of parameters can be used as inputs, such as physical, geometrical or bias parameters, as long as training data can be generated. This makes it possible to adjust many of the device parameters in RF and microwave CAD applications. Two approaches are usually used to model a microwave active device by using the "neural networks" method [140]: direct modeling approach and indirect modeling approach through a known equivalent circuit model. In the direct modeling approach, neural networks are used to model the external behavior of the devices directly. Because a neural network can learn directly from the measurement data, this model not only can cover all the practical effects, including those semiconductor effects which are not covered in the available commercial models, but also can be developed even before the relevant theory and experience are available. Also, such a model includes no or fewer assumptions than those equivalent circuit models. As for the indirect modeling approach, neural networks always work through those known equivalent circuit models, which are easily compatible with CAD tools. But, such models are limited by the various assumptions of the equivalent circuit models.

5.2 Gummel-Poon (GP) Model

5.2.1 Overview of the GP model

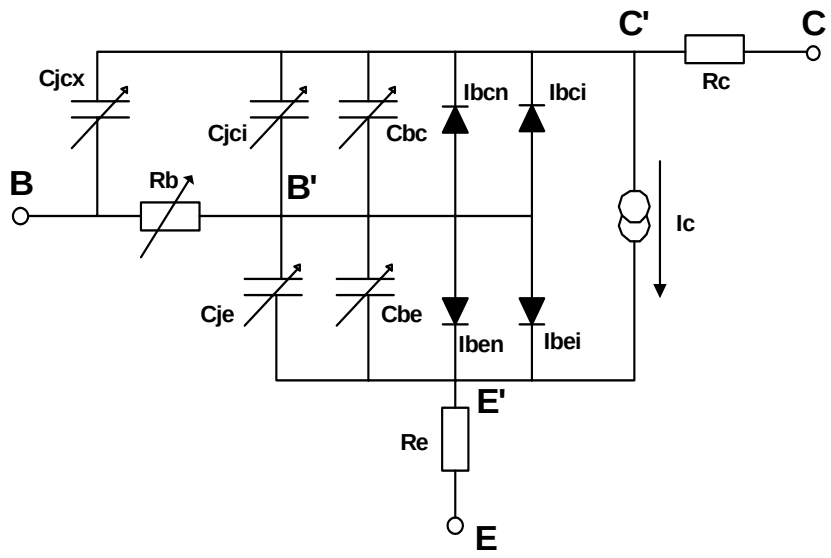

Figure 5.1. The complete equivalent circuit for GP model.

The EM model, which was introduced by Ebers and Moll in 1954, is the first compact model for bipolar transistors. To overcome the limitations of the EM model, a more advanced bipolar transistor model was introduced by Gummel and Poon in 1970, which is called GP model [51]. Figure 5.1 is the complete equivalent circuit for the GP model. Three points should be highlighted in this figure [52]. First, two additional non-ideal diodes I_{ben} and I_{bcn} have been added in the GP model to include the additional components of base current in the low current region such as leakage currents . Second, the expression of a single current generator has been modified to account for high-injection effect. Finally, the base-collector junction capacitance(C_{JC}) in the EM model has been split into two parts. While the intrinsic part (C_{jci}) remains at the original location, the extrinsic part (C_{jcx}) bypasses the base resistance and directly connects the base to the collector terminal.

In general, the derivation of the GP model assumes a one-dimensional bipolar transistor structure. Basically, there are three major steps in the derivation of the GP model [4]. First, a new expression of the saturation current I_S is obtained based on a

careful examination of the current density equations in a bipolar transistor. This new I_S expression inherently incorporates some different bipolar transistor effects, such as base-width modulation, high-level injection and dependence of the total forward transit time on the collector current. At this stage, the most significant point is that the new importance is given to the majority carrier (hole in a NPN bipolar transistor) concentration profile in the base. Second, those effects above are artificially separated into different components so that they can be understood and modeled independently. In this way, the performance of the integration can be controlled and the dependence of the integration limits on junction voltages has been avoided. A careful examination of the physical meaning of each of these components can improve the understanding of the bipolar transistor operation. In here, each of the artificial components is modeled in terms of measurable parameters. Finally, In order to describe more second-order effects of a bipolar transistor, the GP model has made some improvements on the EM model, among which the most important improvement is the introduction of the parameter of q_b , namely, a normalized base charge.

5.2.2 Extraction Methods for the GP Model Parameters

5.2.2.1 General GP Model Extraction and Optimization Strategy

Although there are many possible model extraction strategies, the following sequence is still recommended, because a reasonable model extraction sequence can raise efficiency and accuracy of the model extraction. In a reasonable model extraction sequence, the measurement and extraction procedures should be arranged in the most logical sequence to allow earlier measured data or extracted parameters to be used as a basis for later measurements or extractions. Also, the sequence requires the least number of measurement configuration modifications [155]. There are three important

points which should be specially remembered during model extraction procedure. (a) In the extraction procedure, the effects of individual parameters or small groups of related parameters should be isolated, and their values can be determined with reasonable certainty. In this way, a list of realistic parameters can be created that should be used in a model to predict the transistor performance accurately. (b) Because of the interdependence of the parameters, the extraction procedure is extremely iterative and involves many personal subjective judgments. So, the validity of the extracted parameters must be checked repeatedly. (c) Because the GP model parameters are very interdependent due to the inherent coupling of the model equations, the purpose of the different measurement setups is to decouple the GP model equations as much as possible.

The following is the general procedure for the GP model extraction . All the related GP model parameters and equations can be referred to Appendix A. The first step in the GP model extraction is to extract the parasitic resistors RE , RBM , RC from " flyback" and the other DC measurement. Then, VAF can be extracted from the forward output characteristic plot and IS , NF , ISE , NE and BF can be extracted from the forward Gummel plot .After the extraction of IKF from the forward DC current gain β vs. I_C curve , BF and IKF should be optimized in the forward DC current gain β vs. I_C curve , IS , NF , ISE and NE should be optimized in the forward Gummel plot, RE and RBM should be optimized in the high-current region of the forward Gummel plot and VAF should be optimized in the forward output characteristic plot. Next, VAR is extracted from the reverse output characteristic plot , NR , ISC , NC and BR are extracted from the reverse Gummel plot and IKR is extracted from the reverse DC current gain β vs. I_C curve . The following steps include optimizing BR and IKR in the reverse DC current gain β vs. I_C curve

,optimizing NR, ISC and NC in the reverse Gummel plot and optimizing VAR in the reverse output characteristic plot . Then, all the capacitance parameters are extracted and optimized, the base resistor parameters RB, IRB and RBM are extracted and transit time parameters TF, XTF, ITF, TR and PTF are extracted. Finally, RB, IRB and RBM should be optimized with biased S-parameters and fine-tuning by using optimization should be performed.

5.2.2.2 Extraction Methods for the GP Model Parameters

In a semi-physical compact model, most of the model parameters can be determined from the device measurements. Therefore, many model extraction methods have been developed to obtain model parameters based on various specially designed measurements. However, it should be mentioned that some of the extracted parameter values can be only regarded as initial values for the following optimization or fine-tuning procedures.

1. *VAF* and *VAR*

The simplest method of obtaining VAF is from the slope of the I_C vs. V_{CE} curve in the linear region [52] , that is , VAF can now be calculated as the intersection of the extrapolated I_C curve with the V_{CE} axis. Actually, VAF is the mean value of the V_{CE} axis intersections of the tangents fitted to the linear region of the transistor output characteristics plot. An alternative method [53] is to determine VAF out of the difference of the two I_C vs. V_{BE} curves for two different base-collector voltages. Then, VAF is determined by the ratio of two I_C values at the same V_{BE}:

$$\frac{I_C(V_{BC1})}{I_C(V_{BC2})} = \frac{1+V_{BC2}/VAF}{1+V_{BC1}/VAF} \quad , \tag{5.1}$$

where V_{BC1} and V_{BC2} refer to the two different base-collector voltages.

After the extraction of the other forward DC parameters, optimization is still needed to get the more accurate value of *VAF* . In the reverse operation region, *VAR* can be obtained by using the similar method above.

2. R_B (*RB* , *IRB* and *RBM*)

The value of R_B strongly depends on the measurement method and the operating condition of the bipolar transistor [52]. R_B should be determined by the method closest to the present operation state of the bipolar transistor studied. If R_B is being measured to verify its effect on the transistor noise performance, the noise measurement method should be used. If the transistor is for the switching application, the pulse measurement technique is the useful method to get the most appropriate value. For small-signal analysis, several measurement methods can be adopted, such as the " input impedance circle method", the " phase cancellation method", the " two-port network method" and the "H-Y ratio technique". After obtaining the R_B vs. I_B curve, the base resistor parameters *RB* , *IRB* and *RBM* can be found by fitting the equations (A.5)-(A.7). It should be noted that *RBM* can be determined by the method of " R_E flyback" [155], with the additional measurement of V_{BE}.

3. *CJE* , *VJE* , *MJE* , *CJC* , *VJC* , *MJC* , *CJS* , *VJS* , *MJS* , *FC* and *XCJC*

In general, there are two ways to measure C_{be} , C_{bc} and C_{cs} . First, these three capacitances can be measured by using a capacitance meter like HP 4284. Second, we propose a more accurate new method to measure S-parameter at a fixed frequency in the "cutoff" mode. In this case, we convert the de-embedded S-parameters into Y-parameters and the three capacitances are given by their functions in the equivalent circuit:

$$C_{be} = \frac{\mathrm{Im}(Y_{11} + Y_{21})}{\omega}, \qquad C_{bc} = \frac{\mathrm{Im}(-Y_{21})}{\omega}, \tag{5.2}$$

and

$$C_{cs} = \frac{\mathrm{Im}(Y_{22} + Y_{21})}{\omega} . \tag{5.3}$$

After the obtaining C_{be}, C_{bc} and C_{cs}, CJE, CJC and CJS can be directly selected from the figures of capacitor vs. voltage. The other capacitance parameters can be determined by optimization.

4. *TF*, *XTF*, *VTF* and *ITF*

The extraction of the parameters above is based on the equation in Appendix A:

$$T_f = TF \cdot \left\{ 1 + XTF \cdot \left[\frac{IS \cdot \left[\exp(\frac{V_{BE}}{NF \cdot V_t}) - 1 \right]}{ITF + IS \cdot \left[\exp(\frac{V_{BE}}{NF \cdot V_t}) - 1 \right]} \right]^2 \cdot \exp(\frac{V_{BC}}{1.44 \cdot VTF}) \right\} . \tag{5.4}$$

First, we measure S-parameters of a bipolar transistor. Then, we transform S to h parameters and determine the frequency of f_{-20dB} from the –20dB/decade range of h_{21}. Now, we measure S-parameters again with the constant frequency of f_{-20dB} and sweep the collector current I_C, then extract TF, XTF and ITF from the figure of T_f vs. I_C. We need to perform the measurement again which is similar to the steps above, but now, V_{CE} is swept with a fixed value of I_C. Then, VTF can be extracted. Finally, we need to optimize VTF, TF, XTF and ITF with biased S-parameters.

5. *PTF*

The excess phase parameter PTF can be found by measuring the phase at unity-gain bandwidth of the bipolar transistor. PTF is the difference between the actual phase at f_T and 90° [53]. Also, PTF can be extracted by using the method of "T.Zimmer" [155]. In his method, the phase of h_{21} vs. V_{BE} should be plotted. As a limitation of the

method, the measurable range only covers a small part of the curve. Therefore, it is advisable to use an optimization method to get PTF .

It has already shown that the extraction of many model parameters is needed in GP model. The method of Ning and Tang [156] is a classical DC method to extract the base resistance R_B and emitter resistance R_E . Nakadai and Hashimoto [157] developed a method to extract R_B at all current levels. They adopted a hybrid-π equivalent circuit to account for both the external and internal base-collector capacitances and applied a method which is similar to the "input impedance circle method" to overcome the "overestimated R_B " problem brought by the method of "two-port network" and the "underestimated R_B " problem brought by the method of "input impedance circle". Linder *et al.* [158], Jo and Burk [159] have introduced DC modeling and extraction methods for base resistance R_B , which could take into account the current crowding, conductivity modulation and base push-out in the base region of a bipolar transistor. The study of Kloosterman, Paasschens and Klaassen [160] has shown that improvement is still necessary for "small-signal high frequency admittance" method to extract base and emitter resistances. Also, the modified "impedance circle method" can be applied to Y-parameters at only one frequency together with the DC Gummel plot. Several special bipolar transistor structures were used to determine the base resistance R_B in the method of Weng, Holz and Meister [161]. Also, their method has been demonstrated to be able to get an accurate estimation of R_B under high forward condition. Thomann and Knorr [162] developed a noise measurement method for the bipolar transistor in a common emitter configuration. Their method has applied the analog computational technique to extract the base spreading resistance. In order to improve the "open–collector method", Gabl,

Reisch and Pohl [163] have derived a more accurate analytical expression for the collector-emitter saturation voltage that is valid in the high-level injection region. Then, a more effective procedure has been proposed to extract the emitter resistance from "open-collector" measurement. A technique of obtaining base and emitter resistances of AlGaAs/GaAs HBTs has been found by Prasad [164], which is based on S-parameters measurement at a single frequency and a given bias. Actually, this method adopted a π-type equivalent circuit and S-parameters must be transferred to h-parameters. R_B and R_E can be calculated from their relations with various h-parameters. Neither special structures nor additional measurements are required in the method and it can be applied to the many different types of bipolar transistors. It is not easy to extract the GP model parameter $XCJC$, which can be used to evaluate the partition of the base-collector junction capacitance through the base resistance. Therefore, the work of Berger, Gambetta, Céli, and Dufaza [165] is very important, because they proposed a high-frequency measurement method to get the parameter $XCJC$. It was demonstrated by them that $XCJC$ can be directly extracted from the real part of the high-frequency small-signal admittance Y_{12} in the common emitter configuration. A hybrid-π equivalent circuit was selected in their method. The extraction method is fast and reliable and does not need any optimization process. Some researchers have also developed extraction methods for the base-collector capacitance. They either modified the bias dependence of the base-collector junction capacitance [166], or utilized physical assumptions about the bias dependence of the small-signal parameters to simplify the extraction of intrinsic and extrinsic base-collector capacitances [167].

5.3 Experiments and Results

5.3.1 Useful Experience for the GP Model Extraction

Some important modeling issues and useful experience in our practical GP model extraction are listed here.

1. It should be noted that the ability to discern reasonable values from questionable ones will only come from the good knowledge of semiconductor device physics, familiarity with the device characteristics and individual practical experience. In a sense, the model parameter extraction sometimes is just like an art.
2. Before the actual measurement, the stability of the transistor should be checked. It must be ensured that the performance of the transistor is repeatable. During the actual measurement, the operation mode of the transistor cannot be changed frequently to make the transistor work in a stable condition. If a chip-formed transistor is used for measurement, any high-intensity light sources must be removed before the actual measurement. This is particularly important if the currents in the nano-ampere range need to be measured.
3. When DC measurements (forward & reverse Gummel plots) are made, the attenuators, which are more than 50 dB , are needed for the setup of vector network analyzer to isolate possible RF power. In order to increase the accuracy of the Gummel measurements, the “integrate time” in the HP4142 DC source/monitor instrument should be set to “long” to reduce the noise at the low current values.
4. In the setting up for the Gummel measurements, the starting value should be low enough so that the base current can bend up at the low end due to the recombination in the base-emitter depletion region. The stopping value should be large enough so that the collector current begins to bend down at the high

end due to high-level effects. But, it should be noted that the current cannot exceed the maximum current limitation of the transistor. In the forward and reverse Gummel measurements, ICCAP's "synchronized sweep with an offset" function should be used to eliminate the need for a switching adapter.

5. The procedure of "Early voltage" extraction is very iterative. The values of Early voltages are strongly dependent on the transport saturation current. Meanwhile, the transport saturation current is also affected by the Early voltages. Therefore, the practical procedure begins with a rough extraction of the transport saturation current, which can be initially used in the extraction of both Early voltages. After the values of Early voltages are extracted and optimized, the transport saturation current will have to be adjusted again.
6. Because accurate capacitance measurements are extremely difficult at the high frequencies, a CV meter cannot be used for the capacitance measurements at the high frequencies. Instead, we analyzed the equivalent circuit of the transistor under the special bias condition and computed the junction capacitances from the measured S-parameters. The frequency in the capacitance measurement should be in the range of MHz to eliminate the effects of test set at the low frequencies and to eliminate the effects of parasitic inductances.
7. Besides the standard calibration of " vector network analyzer" for the swept frequency S-parameter measurements, two additional calibrations of "vector network analyzer" are still needed at a single frequency for the CW S-parameter measurements, that is, the measurements of " junction capacitances" and "h_{21} vs. V_{BE}". The input power and attenuation factor of the vector

network analyzer should be set up judiciously, because these parameters will affect the S-parameters considerably.

8. During the model parameter extraction, the “tune fast”, “tune slow” and “optimize” functions should be applied reasonably together to speed up the extraction procedure.

5.3.2 Experimental Results

Because the packaged transistors are used in our measurement, the general problem involved in S-parameter measurement is the calibration of a vector network analyzer (VNA). The primary reference plane in such a measurement is generally at some points within the VNA itself. So, the measurement will include losses and phase delays caused by the effects of the connectors, cables and transitions that must be used to connect the device under test (DUT) to the VNA. These parasitic effects can be lumped together in a two-port error box placed at each port between the actual measurement reference plane and the desired reference plane for the two-port DUT. Therefore, a calibration procedure is needed to characterize the error boxes before the formal measurement of the DUT. After the calibration, the error-corrected S-parameters can be determined from the measurement data. Considering the structure of the DUTs, the Thru-Reflect-Line (TRL) technique is selected in the experiments [26]. The advantage of TRL calibration is: this calibration procedure does not rely on the standard loads, which are always imperfect to some degree and may introduce significant errors at the higher frequencies or as the quality of the measurement system improves. Instead, TRL uses three connections to allow the error boxes to be characterized completely. Figure 5.2 shows the pictures of TRL calibration and measurement test fixtures.

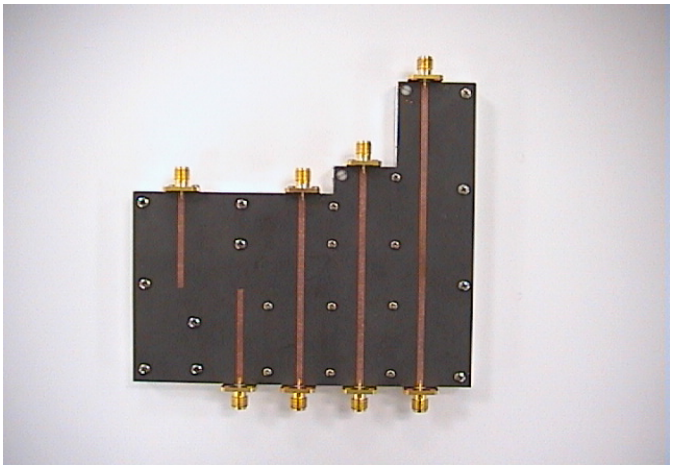

(a)

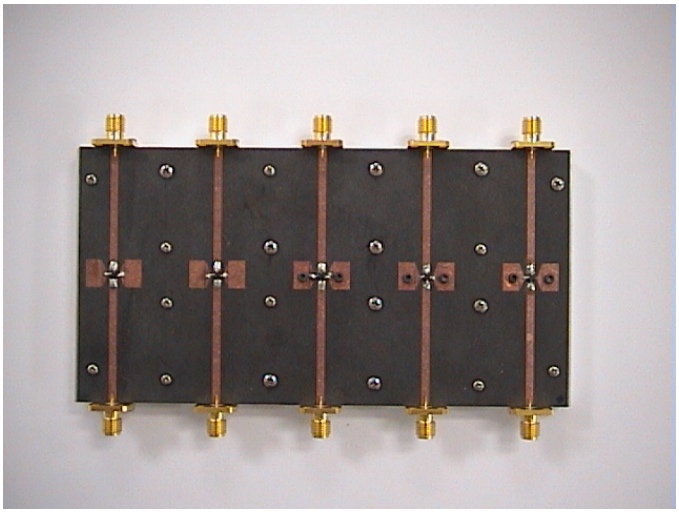

(b)

Figure 5.2. The pictures of TRL calibration (a) and measurement (b) test fixtures.

The TRL test fixture is designed and fabricated according to the frequency range in the experiment, which is from 0.5GHz to 8.0 GHz. The specifications of TRL test fixture are listed as follows:

1. Substrate : ε_r =2.2, H= 31 mil, Tang = 0.001 and T=0.01778 mm, where ε_r is the substrate dielectric constant, H is the substrate thickness, Tang is the dielectric loss tangent and T is the conductor thickness .
2. Width of line: W=2.4 mm.
3. Length of "through line": L_1= 7.5 cm.
4. Length of " first delay line": L_2=11.88 cm.
5. Length of " second delay line": L_3 =8.59 cm.

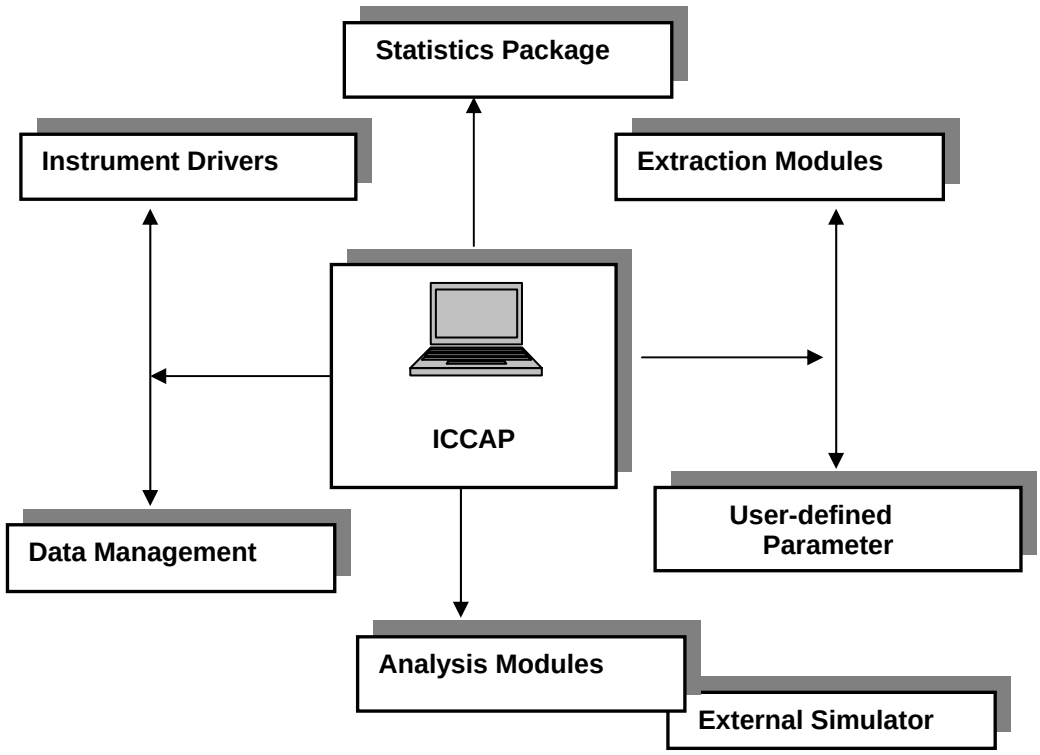

Figure 5.3. General organization of the ICCAP system.

The measurement and model parameter extraction are performed in the environment of ICCAP. ICCAP (Integrated Circuits Characterization and Analysis Program), which was introduced in 1990, is a commercially available software for modeling electronic components [168]. Its link to external simulators has paved the way for the modeling of many different types of electronic components with any desired combinations. In general, ICCAP is capable of accurately determining the

model parameters for all devices and circuits which can be described by a simulator. Figure 5.3 shows the general organization of an ICCAP modeling system [169]. The advantages above have made it possible to model various devices, such as packaged or chip-formed MOS, BJT, MESFET,HEMT or HBT etc., to describe the high-frequency behavior of passive components such as resistors, inductors or capacitors, etc., and also to combine these devices together in macro models. The other advantages of the ICCAP modeling system include its support for the user-defined models in the simulator, the convenient implementation of corresponding extraction procedures using a BASIC-like language – "Parameter Extraction Language"(PEL) and the availability of user-defined C-code routines.

The general ICCAP operating procedure is as follows [168]-[169]:

1. Install the device under test (DUT) and connect the instruments with the control computer and ICCAP via the HP-IB bus;
2. Open ICCAP main window and load an existing model or create a new model;
3. Execute ICCAP's *Measure* command and control the corresponding instruments to obtain various device characteristics;
4. Edit programs and execute ICCAP's *Extract* command to extract model parameters from the measured data;
5. Send the circuit definition and the extracted model parameters to the simulator to determine the simulated data;
6. Compare the measured and simulated data and execute ICCAP's *Optimize* command to achieve the best possible fit between the measured and simulated data;
7. Display or print results in graphic and tabular forms.

Figures 5.4 – 5.20 are some of the measurement results during the GP model extraction procedure. All the figures above are very useful for the GP model extraction or optimization as shown in Table 5.1.

Table 5.1 The applications of some experimental results for the GP model extraction

Figure series number	**Applications for the model extraction**
5.4	*BF* and *IKF* can be optimized.
5.5	*IS*,*NF*,*ISE*,*NE* and *BF* can be extracted and all the above parameters except *BF* can be optimized. Also, optimization of *RE* and *RBM* can be performed.
5.6	*IKR* can be extracted and *BR*,*IKR* can be optimized.
5.7	*ISC*,*NR*,*NC* and *BR* can be extracted and *ISC*,*NR*,*NC* can be optimized.
5.8-5.9	*VAF* can be extracted and optimized.
5.10-5.11	the initial values of *RE* and *RC* can be extracted
5.12-5.13	all the capacitance-related model parameters can be extracted and optimized.
5.14-5.16	transit time-related model parameters can be extracted and optimized.
5.17-5.20	to optimize *RB*,*IRB* , *RBM* and are frequently used in the optimization or fine-tuning at the final stage of model extraction.

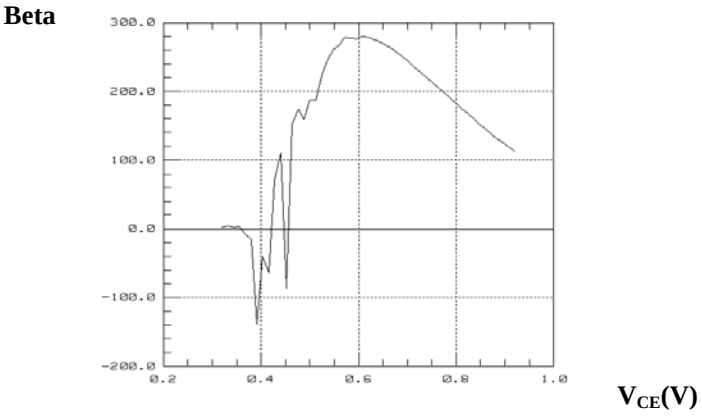

Figure 5.4. Forward beta vs. V_{CE} .

I_B (I_C) (A)

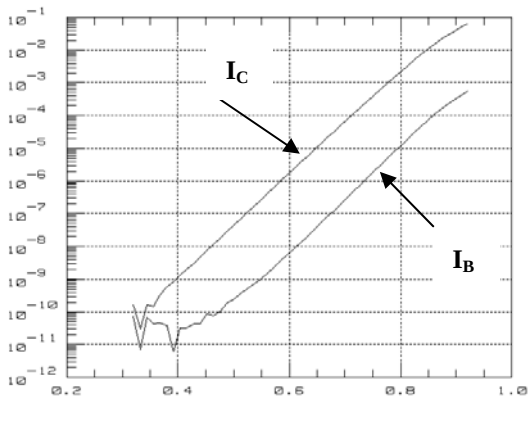

V_{BE}(V)

Figure 5.5. Forward Gummel plot.

Beta (E3)

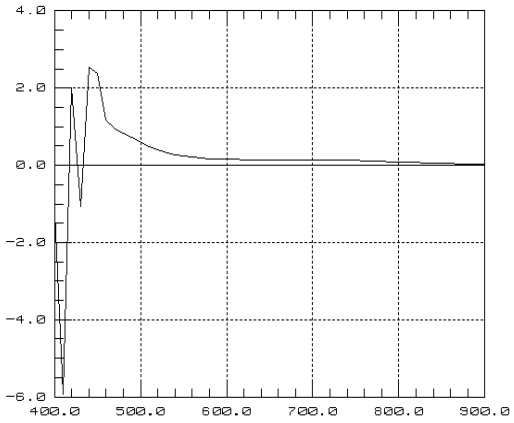

V_{EC}(mV)

Figure 5.6. Reverse beta vs. V_{EC}.

I_B(I_E) (A)

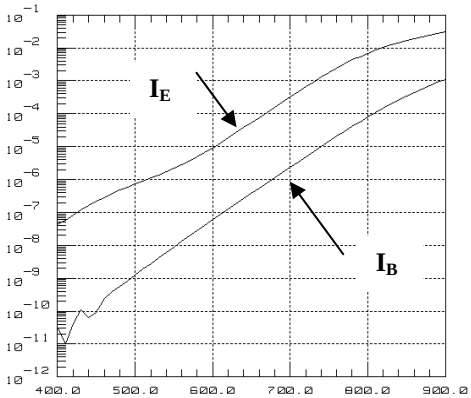

V_{BC}(mV)

5.7. Reverse Gummel plot.

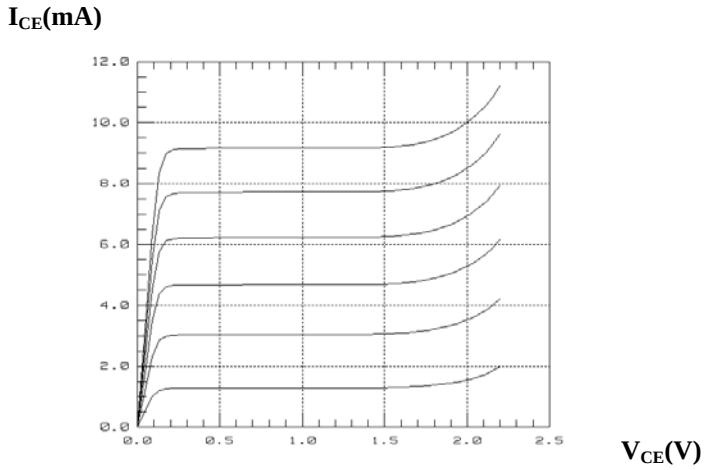

Figure 5.8. I_{CE} vs. V_{CE} ((I_B: 5uA – 45uA, step: 8uA).

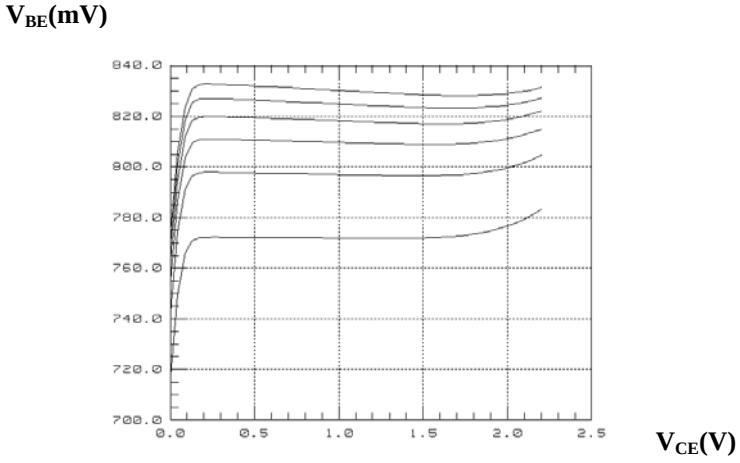

Figure 5.9. V_{BE} vs. V_{CE} (I_B: 5uA – 45uA, step: 8uA) .

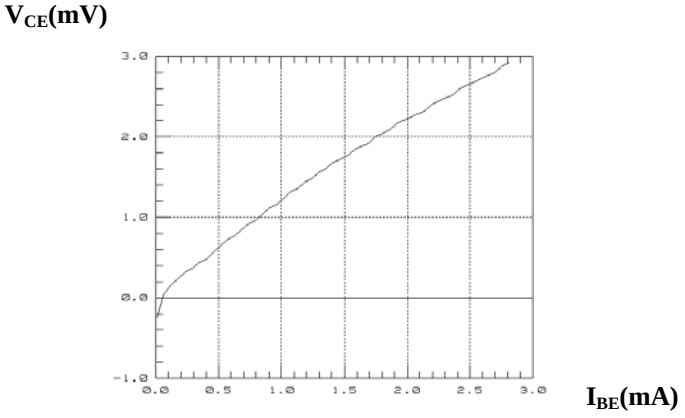

Figure 5.10. "R_E flyback" measurement .

V_{EC}(mV)

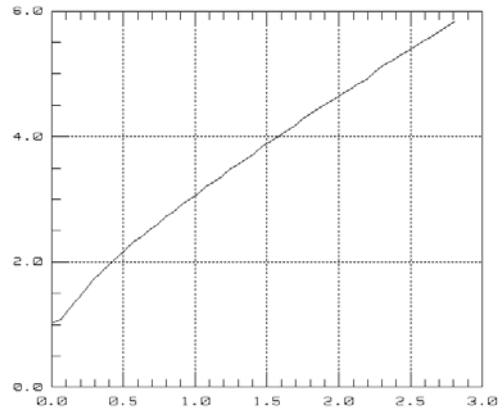

I_{BE}(mA)

Figure 5.11. "R_C flyback" measurement.

C_{be}(pF)

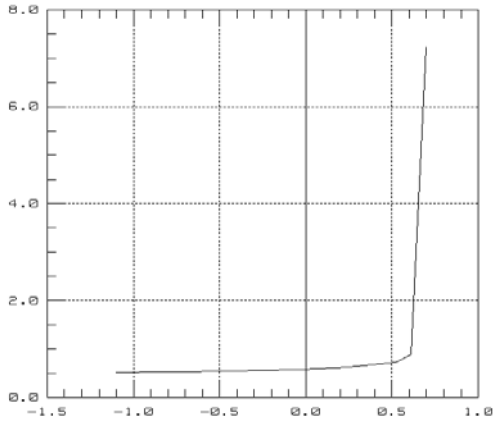

V_{BE} (V)

Figure 5.12. C_{be} vs. V_{BE} .

C_{bc}(pF)

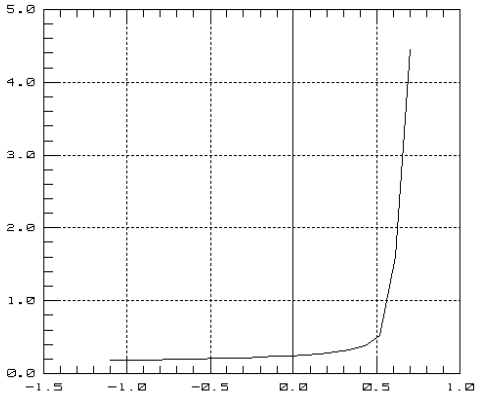

V_{BC}(V)

Figure 5.13. C_{bc} vs. V_{BC} .

T_f (us)

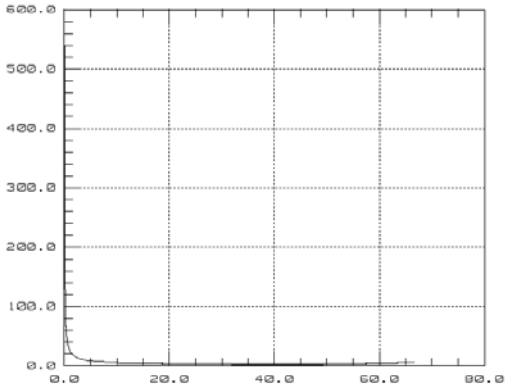

I_{CE}(mA)

Figure 5.14. T_f vs. I_{CE}.

f_T(GHz)

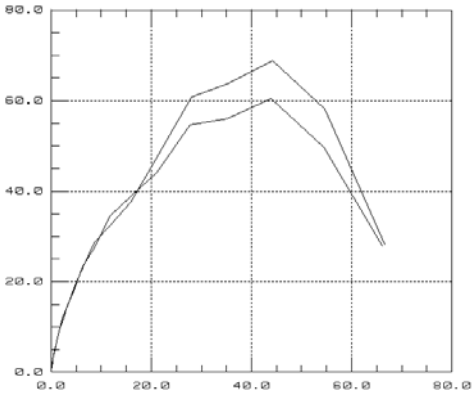

I_{CE}(mA)

Figure 5.15. f_T vs. I_{CE} .

Mag(h_{21})

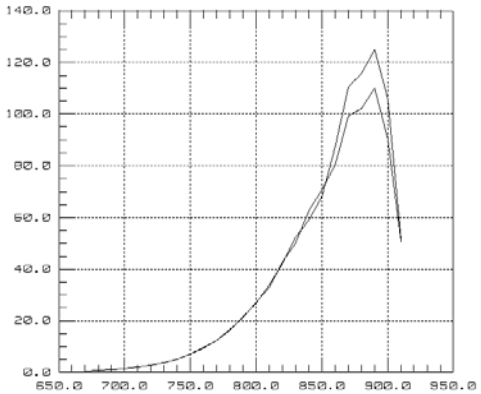

V_{BE}(mV)

Figure 5.16. Mag(h_{21}) vs. V_{BE} .

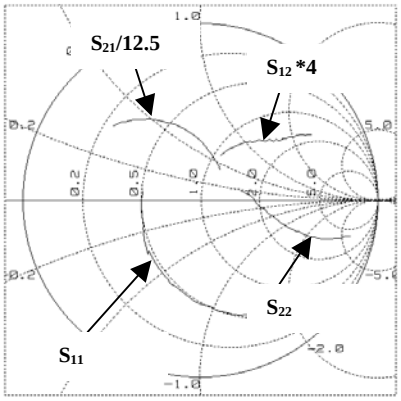

Figure 5.17. S-parameters (Freq: 0.5-3 GHz, Bias: V_{BE}=0.8V and V_{CE}=1.0V).

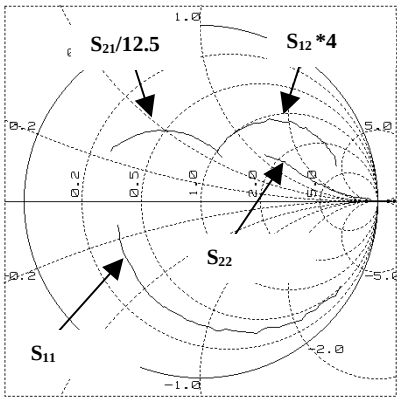

Figure 5.18. S-parameters (Freq: 0.5-3 GHz, Bias: V_{BE}=0.77V and V_{CE}=1.0V).

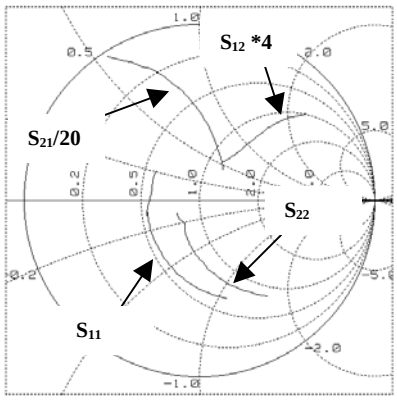

Figure 5.19. S-parameters (Freq: 0.5-3 GHz, Bias: V_{BE}=0.83V and V_{CE}=1.0V).

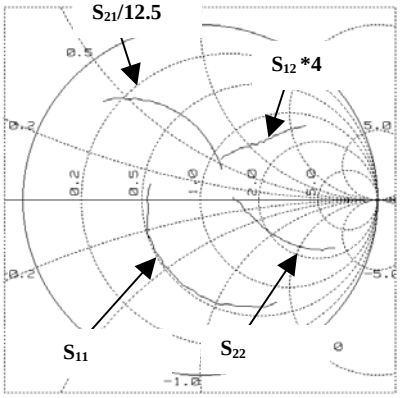

Figure 5.20. S-parameters (Freq: 0.5-3 GHz, Bias: V_{BE}=0.81V and V_{CE}=1.0V).

Table 5.2 shows the GP model parameters which are extracted with the methods discussed in Section 5.2.2.

Table 5.2 The extracted GP model parameters

Model Parameter	Value	Model Parameter	Value	Model Parameter	Value
IS	0.309 fA	*IKR*	7.04 mA	*MJS*	0.48
ISC	18.59 fA	*RB*	2.684 Ω	*FC*	0.791
BF	580.2	*IRB*	17.45 uA	*XCJC*	0.95
BR	105.3	*RBM*	2.507 Ω	*TF*	1.506 ps
VAF	995 V	*RE*	0.865 Ω	*XTF*	2.67
VAR	2.1 V	*RC*	2.367 Ω	*VTF*	0.508 V
NF	1.086	*CJE*	367.4 fF	*ITF*	2.554 A
NR	1.08	*VJE*	0.905 V	*PTF*	0.45 deg
NE	3.118	*MJE*	0.334	*TR*	0.402 ns
NC	2.533	*CJC*	256.9 fF		
ISE	3.045 pA	*VJC*	0.801 V		
MJC	0.3389	*CJS*	54.84 fF		
IKF	2.333 A	*VJS*	0.61 V		

5.3.3 Model Verification on the Device Level

After the model parameter extraction, model verification is carried out on a single device level. Figures 5.21-5.28 are the comparisons between measured and simulated

data. From these comparisons, it is noted that the simulated results fit the measured data quite well. Furthermore, as shown in Table 5.3, RMS errors between measured data and simulated results have been calculated to show the fitting performance of the extracted GP model. It is observed that calculated RMS errors are acceptable for practical applications, which means that good agreement between measured data and simulated results can be obtained by the extracted GP model. However, it should be mentioned that RMS error is larger for "I_{ce} vs.V_{ce}" (Figure 5.24, V_{ce}<2.5V), especially in the range of breakdown. This issue will be discussed and a new improved model will be proposed in the next section.

Table 5.3 RMS errors to show the comparisons between measured data and simulated results

Measurement data	RMS error (%)
C_{jc} vs. V_{bc}	1.21
C_{je} vs.V_{be}	1.18
I_{ce} vs.V_{ce} (V_{ce}<1.0V)	1.54
S-parameters (V_{be}=0.83V, V_{ce}=1.0V)	4.67
S-parameters (V_{be}=0.80V, V_{ce}=1.0V)	4.01
S-parameters (V_{be}=0.77V, V_{ce}=1.0V)	4.12
S-parameters (V_{be}=0.81V, V_{ce}=1.0V)	4.35

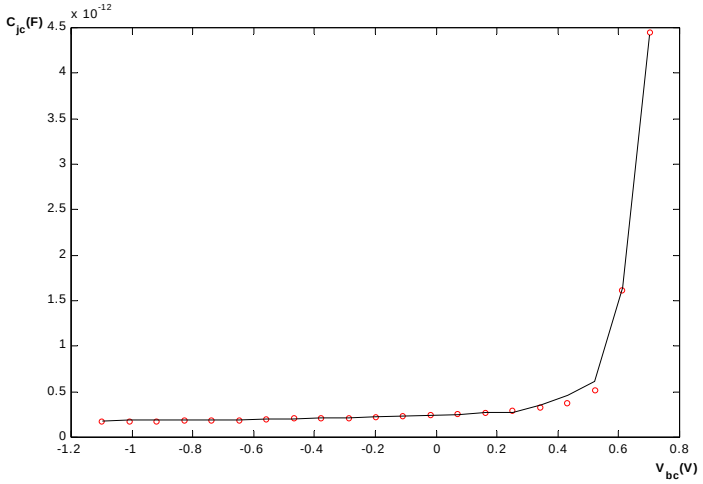

Figure 5.21. The comparison between simulated and measurement data in the curve of " C_{jc} vs. V_{bc}". Circles indicate measured values and solid lines indicate simulated values.

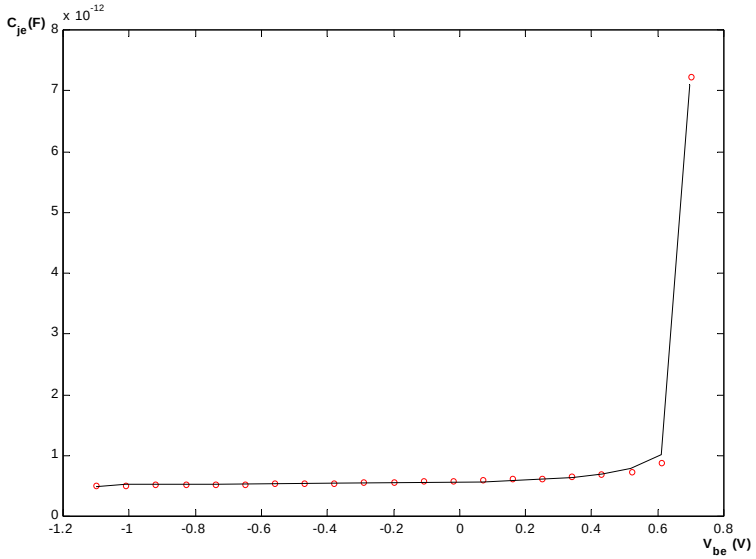

Figure 5.22. The comparison between simulated and measurement data in the curve of " C_{je} vs. V_{be}". Circles indicate measured values and solid lines indicate simulated values.

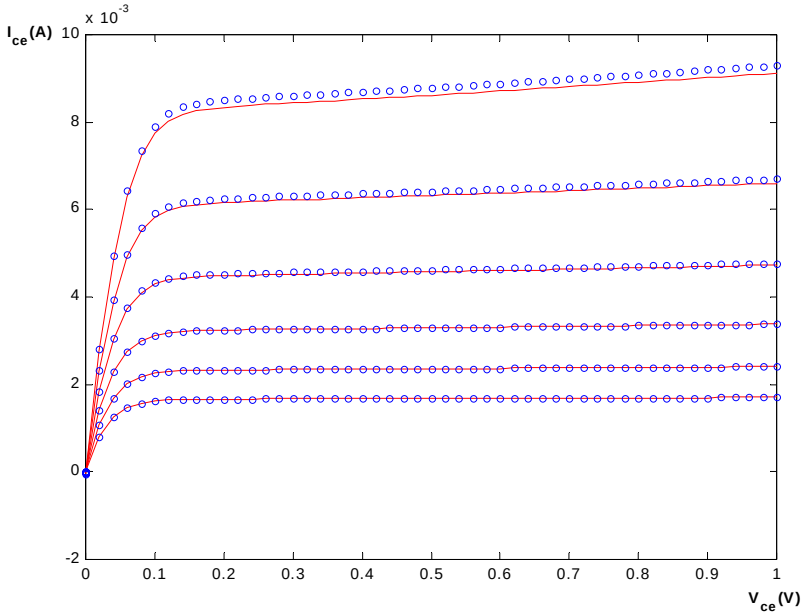

Figure 5.23. The comparison between simulated and measurement data in the curve of " I_{ce} vs. V_{ce}" (1). Solid lines indicate measured values and circles indicate simulated values.

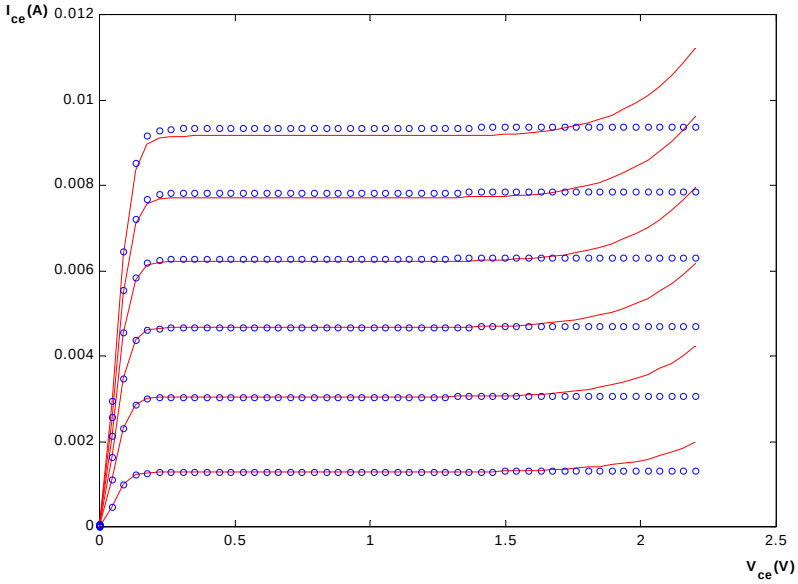

Figure 5.24. The comparison between simulated and measurement data in the curve of " I_{ce} vs. V_{ce}" (2). Solid lines indicate measured values and circles indicate simulated values.

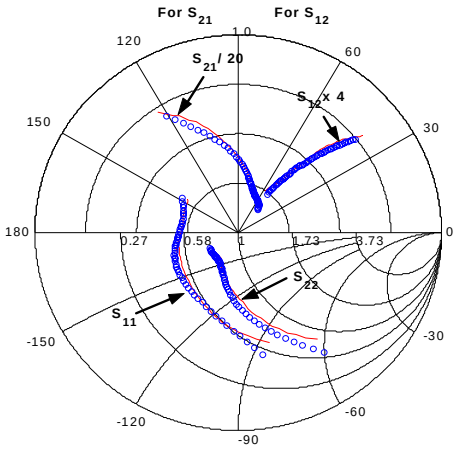

Frequency: 0.5GHz-3GHz

Figure 5.25. The comparison between simulated and measurement data in the curve of " S-parameters (Freq: 0.5-3 GHz, Bias: V_{be}=0.83V and V_{ce}=1.0V)". Solid lines indicate measured values and circles indicate simulated values.

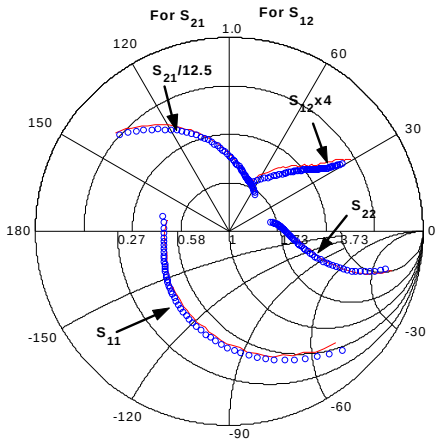

Figure 5.26. The comparison between simulated and measurement data in the curve of " S-parameters (Freq: 0.5-3 GHz, Bias: V_{be}=0.80V and V_{ce}=1.0V)". Solid lines indicate measured values and circles indicate simulated values.

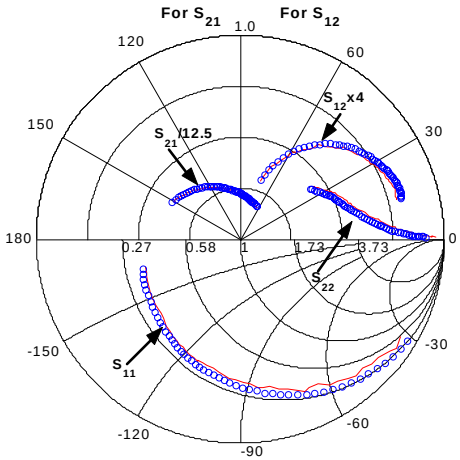

Figure 5.27. The comparison between simulated and measurement data in the curve of " S-parameters (Freq: 0.5-3 GHz, Bias: V_{be}=0.77V and V_{ce}=1.0V)". Solid lines indicate measured values and circles indicate simulated values.

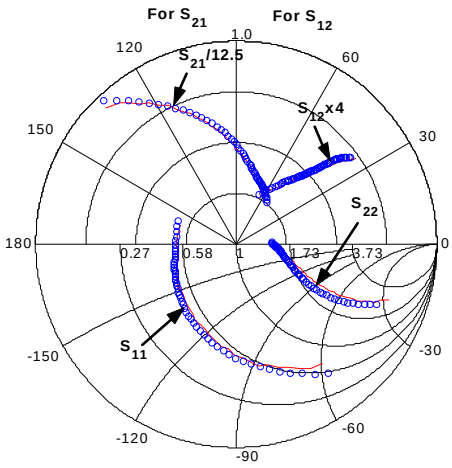

Figure 5.28. The comparison between simulated and measurement data in the curve of " S-parameters (Freq: 0.5-3 GHz, Bias: V_{be}=0.81V and V_{ce}=1.0V)". Solid lines indicate measured values and circles indicate simulated values.

5.4 HBT Amplifier Design and Fabrication

In order to further verify the extracted HBT nonlinear GP model on a microwave integrated circuit level, a high gain, high linearity and low power dissipation SiGe HBT amplifier has been designed, fabricated and tested on the basis of the GP model parameters extracted in Section 5.3.

5.4.1 The Selection of Substrate and Transistor

The selection of the substrate and the transistor plays a vital role in the microwave integrated circuit design, because it is usually the first step in the circuit design . Generally speaking, the substrate should be selected when the fabricated line is realizable and can withstand the large possible current flows. It should be noted that

the selection of the substrate will impose a constraint on the passive element modeling. By choosing a very high substrate permittivity, the resultant line width corresponding to 50Ω match will become very small, whereas the line width will be very wide with the very low substrate permittivity. Both of these extreme cases can invalidate the passive element modeling adopted for the design. Moreover, the trade-off between the ease of cutting and the roughness of the substrate must be considered .With the above criteria, a 33 mils thick RT/Duriod 5500 substrate , with the effective permittivity of 2.2, is selected.

Similar to those transistors which are used to extract HBT GP model, the SiGe HBT transistors with the package of SOT353 have been selected for the circuit design and fabrication.

5.4.2 Circuit Topology of a SiGe HBT Amplifier

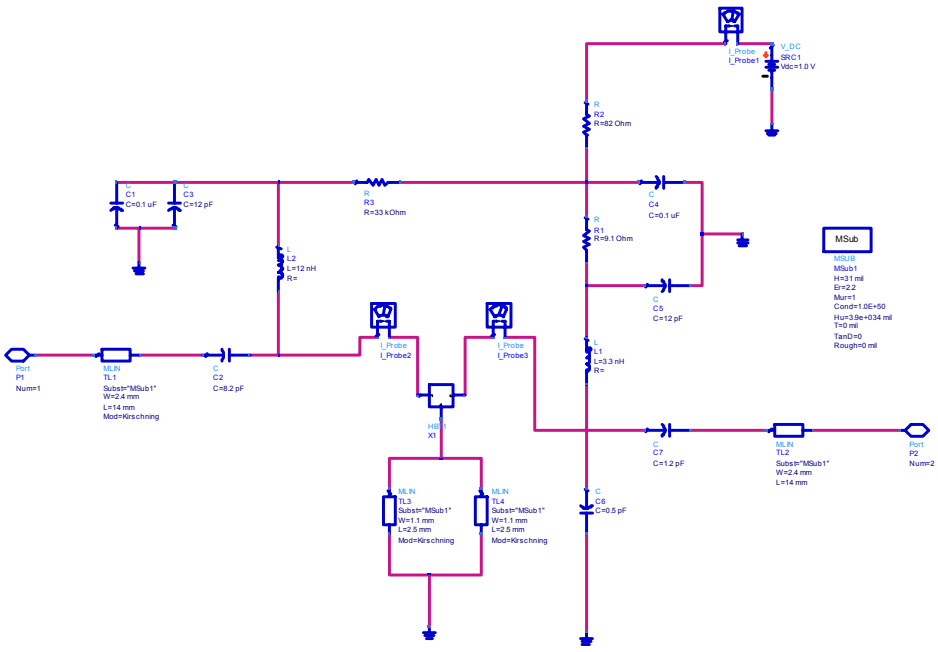

(a)

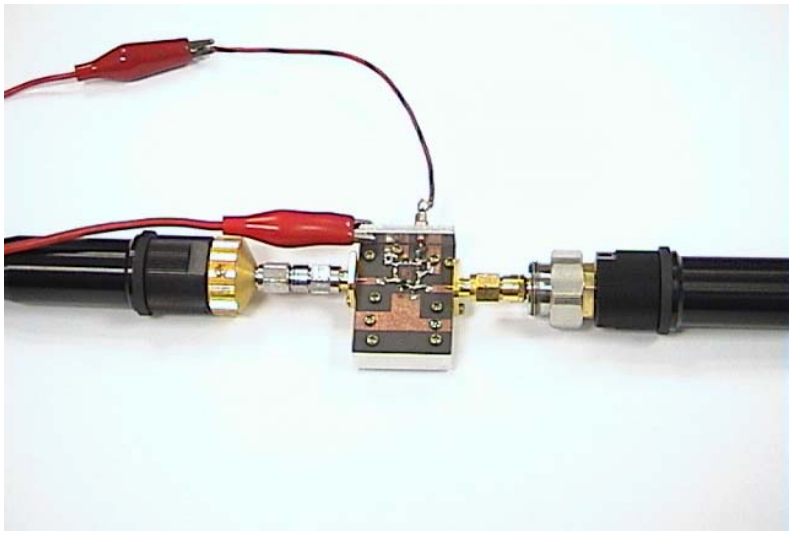

(b)

Figure 5.29. The schematic circuit topology (a) and picture (b) of the designed SiGe HBT amplifier.

Figure 5.29 gives the schematic circuit topology and picture of the designed SiGe HBT amplifier for model verification . ADS EDA tool from Agilent company has been used in the circuit analysis and optimization. The HBT amplifier is designed with the following specifications: frequency range: 1.8 GHz – 2.1 GHz, S_{21} >14 dB, S_{12} < - 15 dB, S_{11}, S_{22} < -10dB and IP3>10dB. A single bias network is used in the circuit.

5.4.3 High Linearity and Stable Bias Network Considerations

Besides the conventional specifications in the microwave integrated circuit design, such as gain, noise figure or input/output match, linearity is also an important consideration in the amplifier design [170]-[174]. First of all, an ideal amplifier should work to amplify signals without adding much noise. Furthermore, it should also keep the linear operation even when strong signals are received. In particular, the amplifier must work linearly to avoid some possible unexpected intermodulation when it receives a weak signal in the presence of a strong interferer. Usually, desensitization (blocking) and cross-modulation are the consequences of intermodulation.

Desensitization (blocking) often occurs when the intermodulation products caused by the strong interferer clear out the desired weak signal. Whereas, cross-modulation is caused when nonlinear interaction transfers the modulation on the amplitude of the interferer to the amplitude of the weak signal. Both effects above are undesirable, so high linearity is a critical issue for the amplifier design to reduce the problems above to meet the demand of practical applications. Actually, there are many linearization techniques in practice, in which feedforward, feedback, predistortion and adaptive linearizations are the common methods for linearization [170]-[174] . Because the main objective of this amplifier design here is the nonlinear model verification, several simple but efficient techniques have been adopted to raise the linear performance of the amplifier. For example, following the approach of "emitter degeneration"[175], the microstrip line with the optimized line length and width is connected to the emitter of the SiGe HBT in the amplifier. Also, the two capacitors have been added between the base and collector terminals of the transistor to suppress the fluctuations of the base and collector voltages.

Common-emitter amplifiers are usually very sensitive to stray impedance in the emitter circuit and any small inductance in series with the emitter will arouse the instability problem. Therefore, stable active bias networks must be implemented to meet the requirement for the high circuit performance. Figure 5.30 is a selected stable active bias network [176]. Here, diode D_1 can provide the temperature compensation and Q_1 can provide the base current of the transistor in the amplifier . The constant voltage difference across R_C then can keep the collector current of the transistor constant.

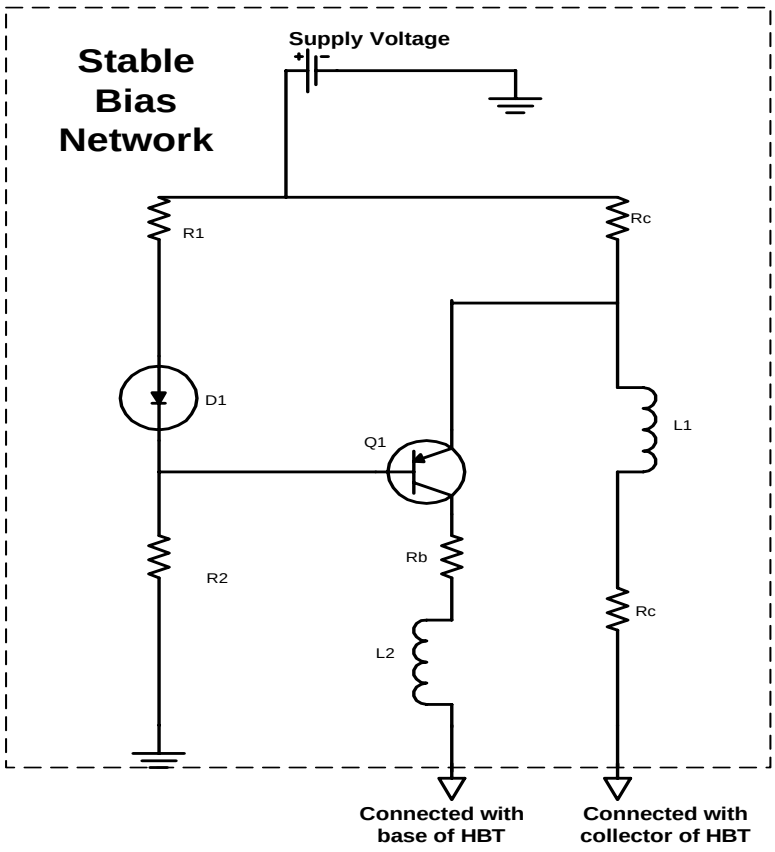

Figure 5.30. A stable active bias network.

5.4.4 Model Verification on Circuit Level

After the design and fabrication of the HBT amplifier, the measured data and simulated results based on the extracted nonlinear GP model have been compared in Figures 5.31 to 5.44. Figures 5.31 to 5.32 show the comparisons of "Gain vs. Output (Input) power" between measured and simulated data. The simulation results fit the corresponding measurement data well, especially in the middle range of the amplifier output power and nearly whole range of the amplifier input power. The simulated and measured output responses of two-tone IP_3 test are provided in Figures 5.33 to 5.36. The measurement data are directly plotted from Agilent spectrum analyzer. So, instead of overlapped-format plots, the comparisons of IP_3 test between simulated and measured data are made with different plots of simulated and measured results

separately. Figures 5.37 to 5.44 are comparisons of amplifier S-parameters between measured and simulated data. Two different biases of 4V and 5V are selected. It can be found that simulation results are able to predict the actual high-frequency performance of the amplifier. Furthermore, the simulation data are reasonable enough for such a microwave integrated circuit with a package-form HBT transistor. In general, the comparisons in Figures 5.31 to 5.44 clearly confirm the good agreement between measured and simulated data. Therefore, the correctness of the nonlinear model implemented in the circuit simulator can be verified.

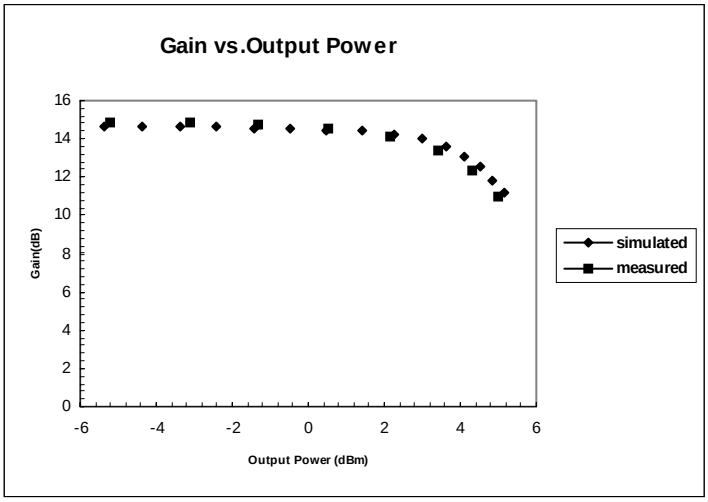

Figure 5.31. The comparison of " Gain vs. Output power" between the measured and simulated data (Bias=3V, Freq=1960MHz).

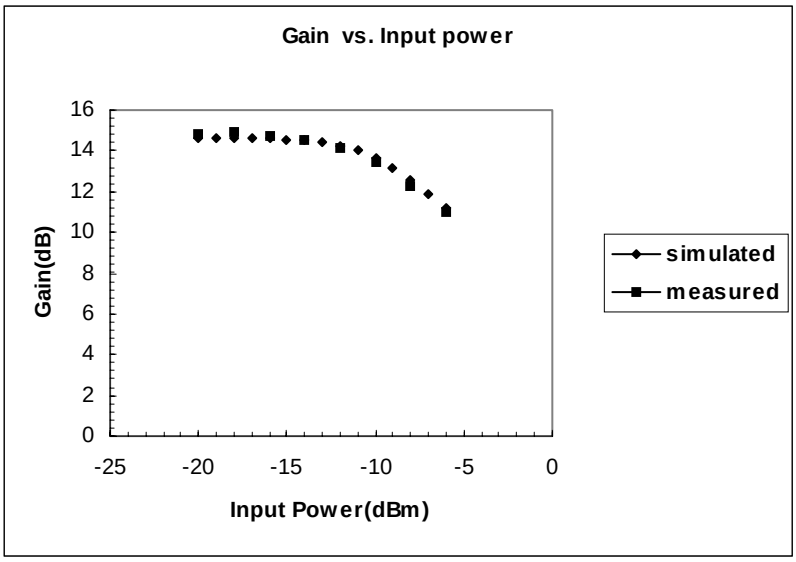

Figure 5.32. The comparison of " Gain vs. Input power" between the measured and simulated data (Bias=3V, Freq=1960MHz).

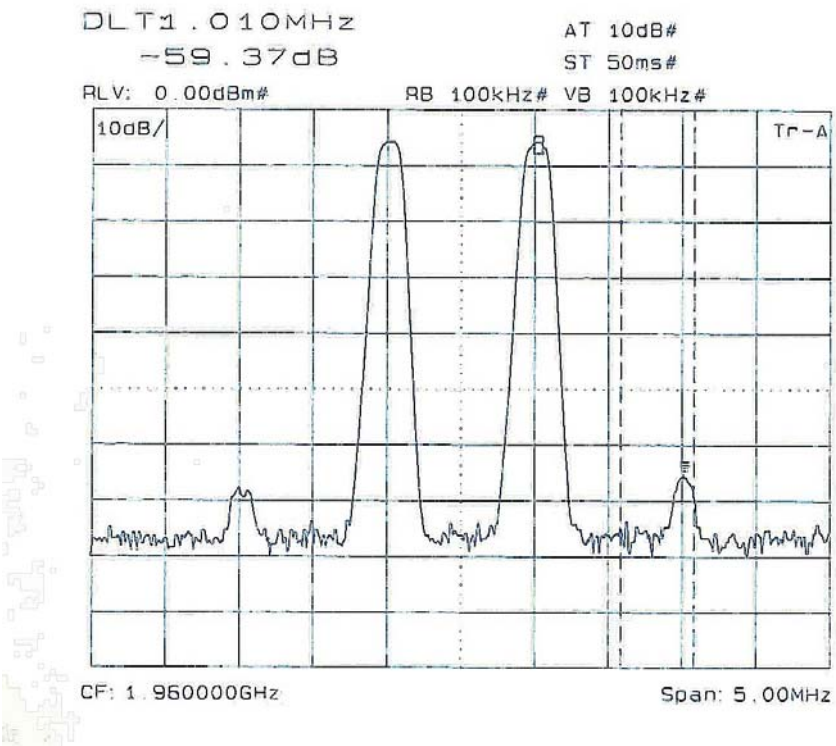

Figure 5.33. The measured output response of two-tone IP_3 test (Bias = 2V, Input power =-10dBm).

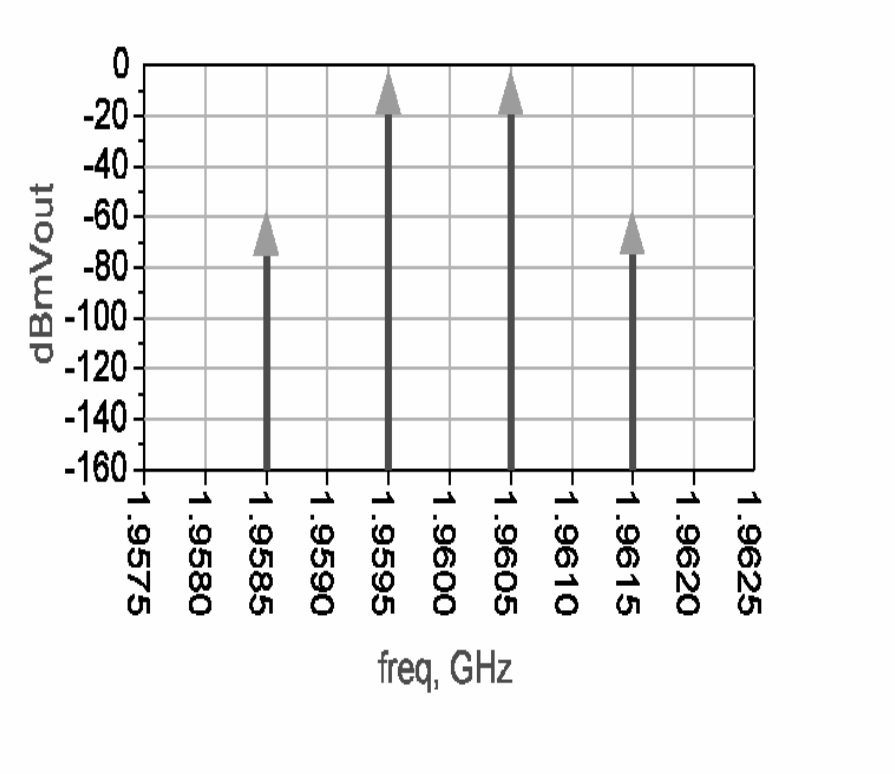

Figure 5.34. The simulated output response of two-tone IP_3 test (Bias = 2V, Input power =-10dBm).

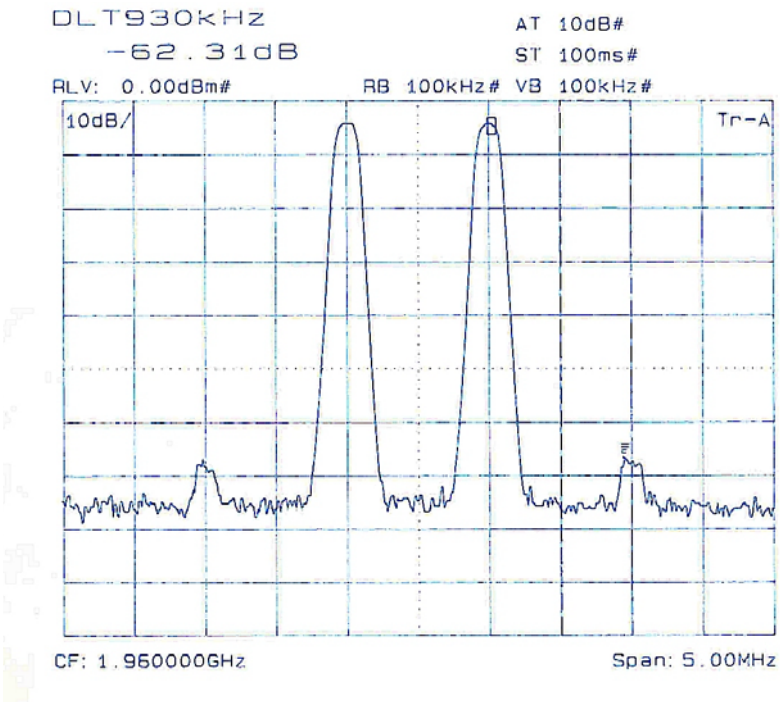

Figure 5.35. The measured output response of two-tone IP_3 test (Bias = 4.5V, Input power =-10dBm).

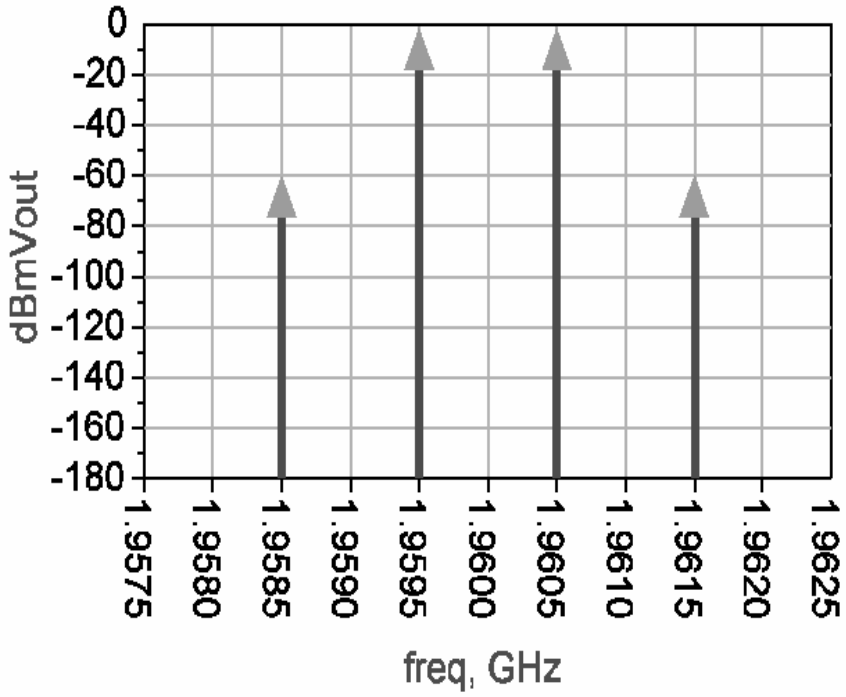

Figure 5.36. The simulated output response of two-tone IP_3 test (Bias = 4.5V, Input power =-10dBm).

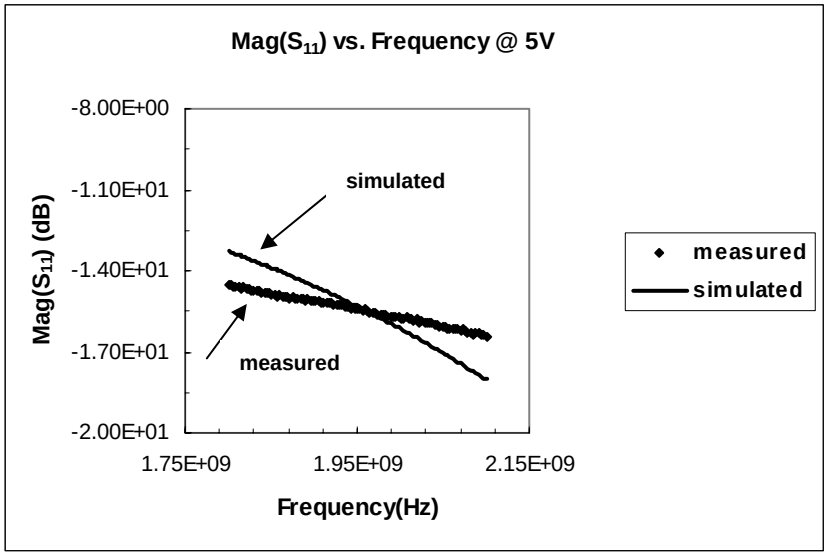

Figure 5.37. The comparison of "Mag (S_{11}) vs. Frequency (Bias=5V)" between measured and simulated data.

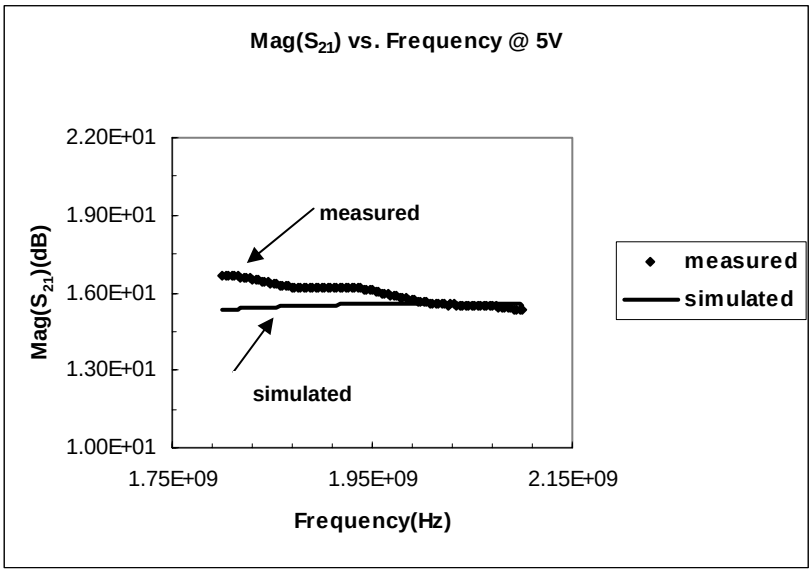

Figure 5. 38. The comparison of "Mag(S_{21}) vs. Frequency (Bias=5V)" between measured and simulated data.

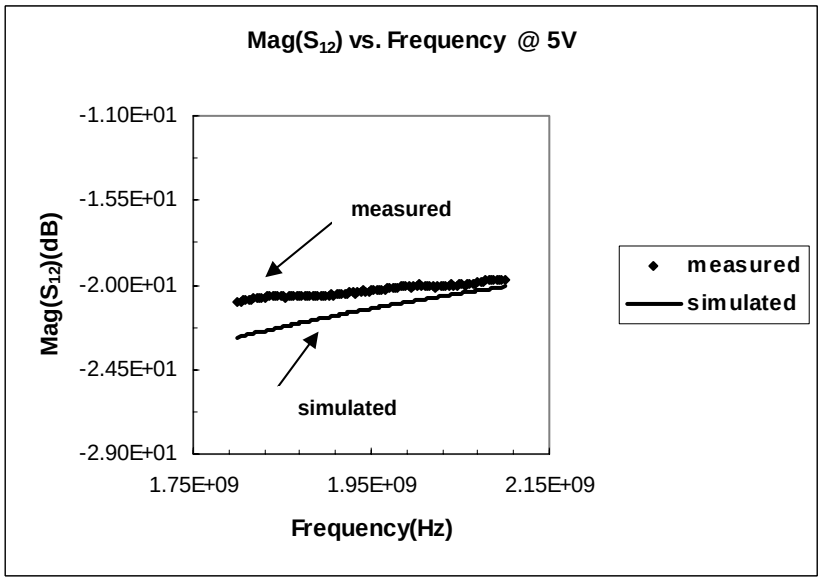

Figure 5.39. The comparison of "Mag(S_{12}) vs. Frequency (Bias=5V)" between measured and simulated data.

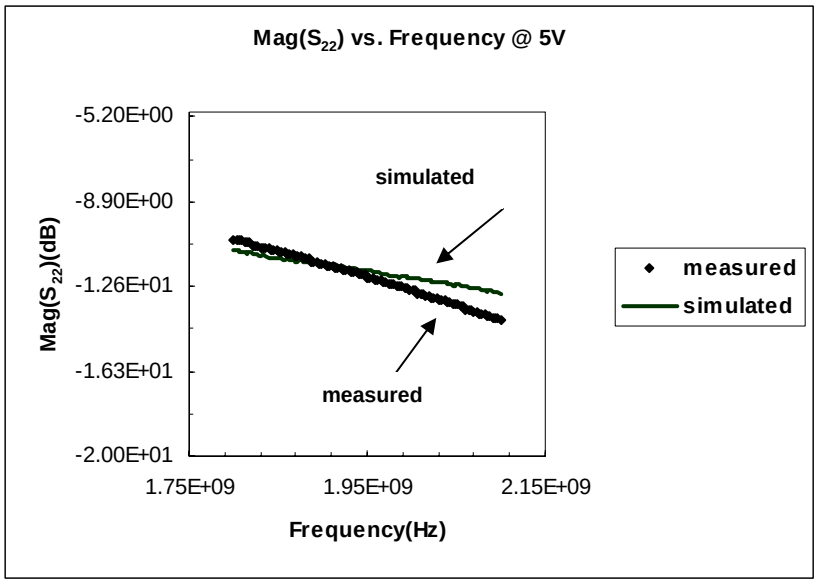

Figure 5. 40. The comparison of "Mag(S_{22}) vs. Frequency (Bias=5V)" between measured and simulated data.

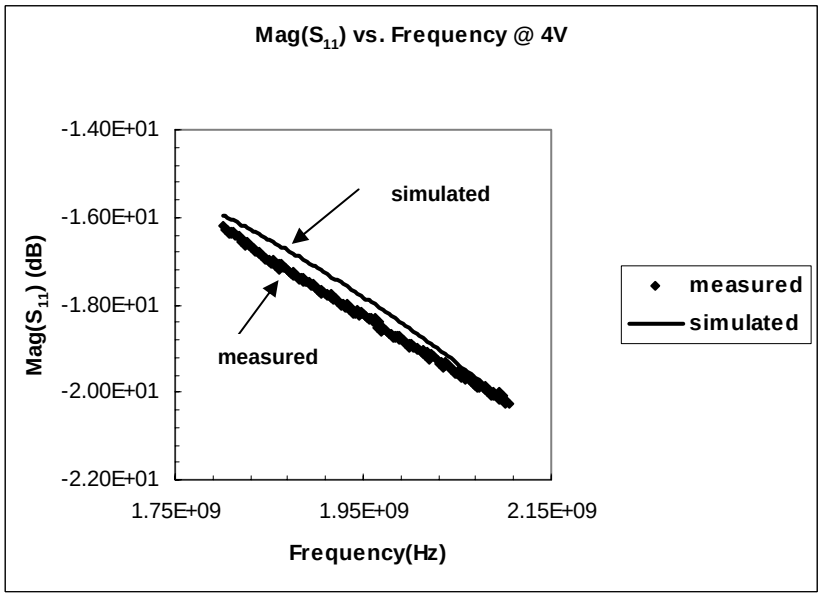

Figure 5. 41. The comparison of "Mag(S_{11}) vs. Frequency (Bias=4V)" between measured and simulated data.

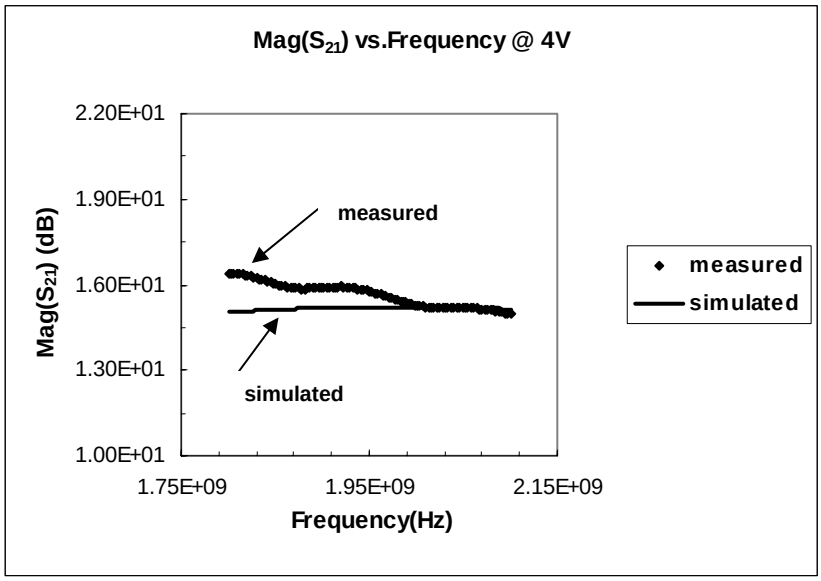

Figure 5. 42. The comparison of "Mag(S_{21}) vs. Frequency (Bias=4V)" between measured and simulated data.

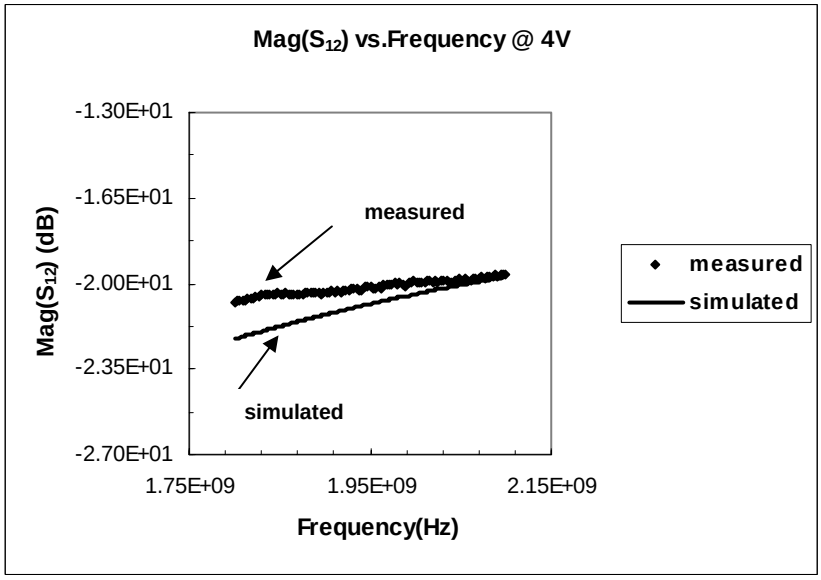

Figure 5. 43. The comparison of "Mag(S_{12}) vs. Frequency (Bias=4V)" between measured and simulated data.

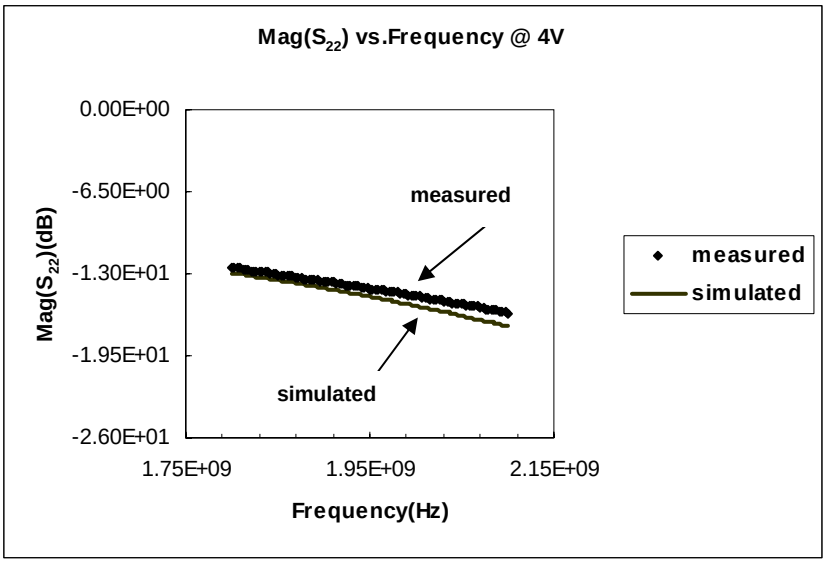

Figure 5.44. The comparison of "Mag(S_{22}) vs. Frequency (Bias=4V)" between measured and simulated data.

The deviations in the S-parameters between measured and simulated data are attributed to the following possible reasons:

1. The fringing and inter-coupling effects between electronic components and microstrip lines are not included;
2. The circuit losses are not considered comprehensively;
3. The parasitic effects of the lumped inductors and capacitors are not modeled completely and accurately in the circuit simulation;
4. The effects of various soldering points are not considered or modeled completely and precisely;
5. The deviations brought about by the circuit fabrication are inevitable, such as soldering points, via holes and metal line etching.

5.5 Vertical Bipolar Inter-Company (VBIC) Model

In the past years, plenty of BJT models that overcome some problems of the GP model have been published [177]-[182]. Meanwhile, a more comprehensive compact model for the bipolar transistors, which is called Vertical Bipolar Inter-Company (VBIC) model, has been developed. The VBIC model has eliminated the shortcomings of the GP model and its complete source code is available for the public domain.

The main objectives of the VBIC model include [54]-[56] (a) to overcome the major deficiencies of the GP model and to meet the modeling requirements of the rapidly growing bipolar transistor technology, (b) to provide the complete source codes, documents and model parameter extraction methods to the public domain , (c) to simplify the whole model by making the model with the default model parameters behave as the GP model , and (d) to avoid using regional functions and to adopt continuous function for the capacitance modeling.

The major advantages of the VBIC model are listed as follows [54]-[56]:

1. accurate implementation of the Early effect or the base width modulation ,
2. description of the depletion capacitances by using continuous functions,
3. improved modeling for the collector resistance modulation due to the "quasi-saturation" effect ,
4. consideration and first-order approximation of the distributed input impedance,
5. inclusion of the effects related to the parasitic substrate transistor and the overlap capacitances,
6. complete modeling for the weak avalanche multiplication ,
7. inclusion of the additional networks for excess phase and self-heating modeling ,
8. enhancement for the transit time modeling, and

9. improvement on the thermal modeling.

5.5.1 Overview of the VBIC Model [54]-[56]

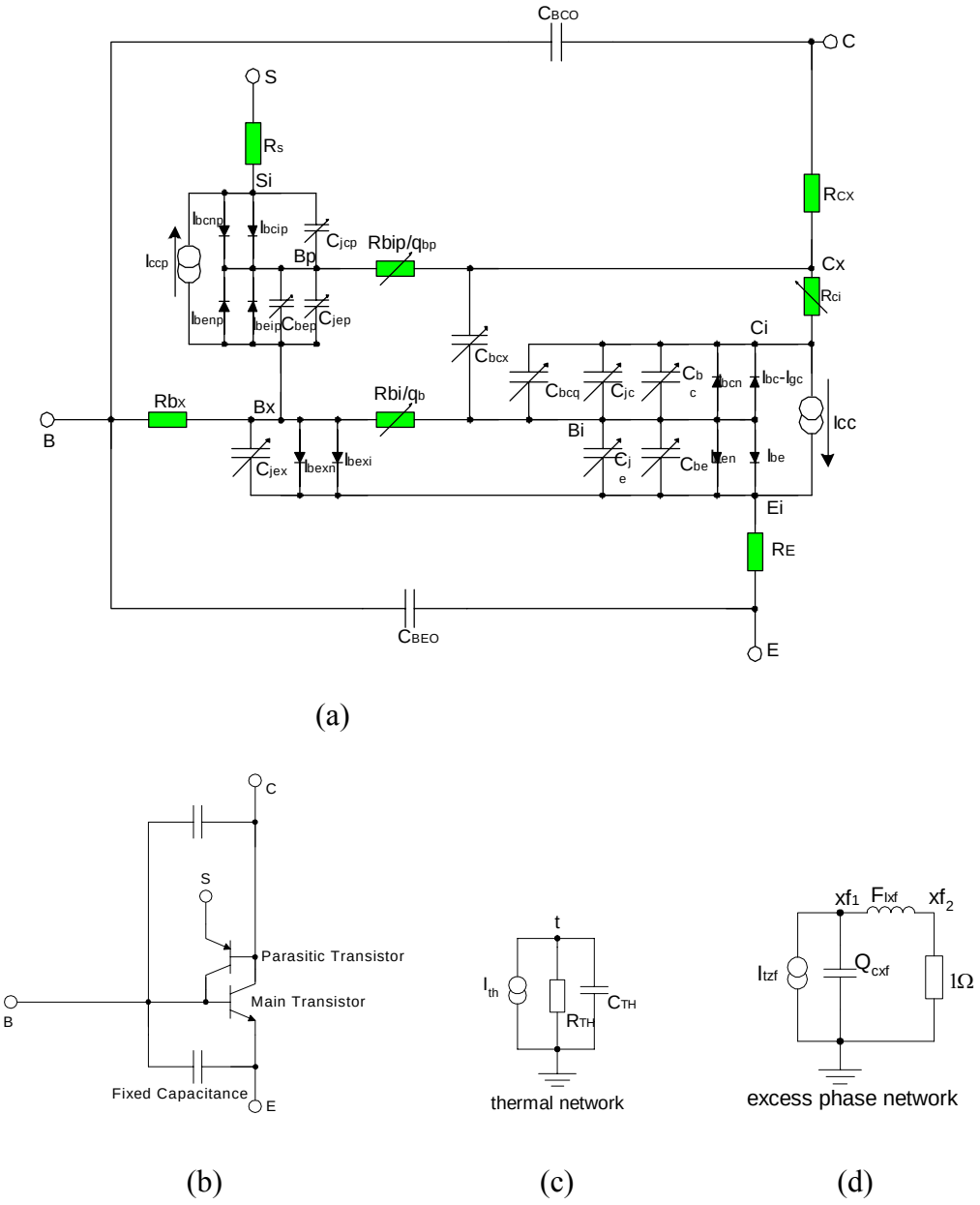

Figure 5.45. Equivalent circuit for the VBIC bipolar transistor model: (a) schematic equivalent circuit including the parasitic transistor, (b) main network, (c) thermal network, (d) excess phase network.

Figure 5.45 is the equivalent circuit of the VBIC model. The whole model equivalent circuit consists of one main network and two sub-networks. The main network includes an intrinsic and an extrinsic bipolar transistors. Meanwhile, one of the sub-networks is used to model excess phase by using a second order network, and the other one is used to model self-heating by adding a thermal network to model the local temperature rise and by including the temperature mappings of the model parameters.

As for the model topology in the main network, the VBIC model has the following different features as compared with the GP model. The parasitic substrate transistor is modeled by a simplified transistor based on the GP model. "Quasi-saturation" effect is modeled on the basis of Kull model [183], [187]. The distributed nature of the base is modeled to a first order. A weak avalanche current source has already been included [184]. The VBIC model has considered the extra phase in the forward transport current of I_{tf} [185]. Several constant capacitances are added to model the extrinsic parasitic capacitances. Now, the intrinsic base resistances for intrinsic and parasitic transistors are modulated by the normalized base charge. Meanwhile, the intrinsic collector resistance is modulated by its controlling voltage.

The default parameters for the VBIC model are used to turn off those elements in the VBIC model that are topologically different from the GP model. It should be noted that the VBIC model is based on the continuous and smooth functions, although there are two exceptions to this. First, conditional statements are still adopted in the VBIC model to avoid some numerical problems such as division by zero; Second, for the compatibility with the GP depletion charge and capacitance model, the regional model is still included in the VBIC depletion charge and capacitance model. In the VBIC model, noise models, with thermal, shot and 1/f noise components that are similar to those of the GP model, are also included.

In the VBIC model, there are two models for the normalized depletion charges q_{je} and q_{jc}. One is the traditional piecewise model used in the GP model, and the other is a continuous model in which the capacitances and depletion charges are limited to constant values when the junction biases are higher than the junction built-in potentials [186]. This gives a good transition between the bias regions where depletion and diffusion effects dominate the junction capacitances.

5.5.2 Extraction Methods for the VBIC Model Parameters

5.5.2.1 The General VBIC Model Extraction and Optimization Strategy

Good modeling strategy and parameter extraction sequence are very essential for the good modeling results. Based on the principle of the VBIC model and inter-dependence of the model parameters, the general VBIC model extraction and optimization strategy is proposed [188]. All the related VBIC model parameters and equations can be referred to Appendix B. As for the basic point in the strategy, the first model parameter extracted is the one that does not rely or depends lightly on the others. Then, the parameters which are less inter-dependent on the others are extracted subsequently.

1. Space charge capacitors must be extracted because the base charge is the most important parameter in the VBIC model.
2. The Early voltages can then be extracted.
3. From forward and reverse Gummel plots, all the diode parameters of the intrinsic transistor are extracted.
4. Similarly, from the substrate measurement, all the diode parameters for the parasitic transistor can be obtained at this stage.

5. The parasitic resistor RS can be determined from the reverse Gummel plot of the parasitic transistor. The similar methods can be adopted to extract the other constant resistors, such as RE, RBX, RCX.
6. The quasi-saturation parameter (except QCO) can be optimized from the DC output characteristics .
7. The method similar to that in the GP model extraction can be used to determine a good starting value for the inner base resistance RBI.
8. With the non-quasi-saturation bias conditions, the transit time parameters can be obtained by using the same technique as that in the GP model .
9. The inner base resistance RBI and the base distribution factor WBE can be optimized from the measured S-parameters without quasi-saturation.
10. At this stage, QCO, which affects the transistor high frequency performance, can be optimized from S-parameters with quasi-saturation.
11. At the last stage, DC output characteristics (especially in the quasi-saturation region) and S-parameters are needed to be fine-tuned with optimization.

5.5.2.2 The Unique Extraction Method for Some of VBIC Model Parameters

1. Early voltage determination

In the VBIC model, the Early voltage extraction method follows that of McAndrew and Nagel [189]-[190]. The major equations are listed below:

$$\left(q_{j,bcf} - \frac{I_{cf} \cdot C_{j,bcf}}{g_{0f}} \right) \frac{1}{VEF} + q_{j,bef} \frac{1}{VER} = -1 \ , \tag{5.5}$$

$$q_{j,bcr} \frac{1}{VEF} + \left(q_{j,ber} - \frac{I_{er} \cdot C_{j,ber}}{g_{0r}} \right) \cdot \frac{1}{VER} = -1 , \tag{5.6}$$

where q_j is the normalized depletion charge, C_j means the normalized junction depletion capacitance and g_0 is the output conductance. The subscripts f and r denote forward or reverse operation condition.

In addition,

$$g_{0f} = \frac{\partial I_c}{\partial V_{ce}} , \quad g_{0r} = \frac{\partial I_e}{\partial V_{ec}} , \tag{5.7}$$

$$a = q_{j,bcf} - \frac{I_{cf} \cdot C_{j,bcf}}{g_{0f}} , \quad b = q_{j,bef} , \tag{5.8}$$

and

$$c = q_{j,bcr} , \quad d = q_{j,ber} - \frac{I_{er} \cdot C_{j,ber}}{g_{0r}} . \tag{5.9}$$

Therefore, we have:

$$VEF = \frac{bc - ad}{b - d} \quad \text{and} \quad VER = \frac{bc - ad}{c - a} . \tag{5.10}$$

2. Space charge capacitances

The extraction method is similar to that in the GP model [188]. But, it should be noted that the parameters *AJE* , *AJC* , *AJS* must be set as -0.5 if we want to use the capacitance expressions in the GP model. The base-collector capacitance is distributed between intrinsic and extrinsic transistors. Also, the main part of this capacitance is usually associated with the parasitic transistor.

3. Diode parameters

When we take the forward Gummel measurement, the base-collector voltage must be set to zero. But, if the collector current is large enough, the "quasi-saturation" effect is always mixed with Webster effect which controls the value of *IKF* .Therefore, *IKF* has to be measured from a special setup in which the collector-emitter voltage is high

enough. Only in this case, the value of *IKF* is approximately the collector current where beta has dropped down to half of its maximum value [188].

4. "Quasi-saturation" parameters

Before the actual fine-tuning of these parameters, it is useful to know well how these parameters affect the output characteristics in the region of "quasi-saturation" [188].

RCI is the resistor that can determine the slope of the output characteristics curve in the saturated range. Therefore, its value can be obtained from the transition section around the "quasi-saturation" region. Also, this parameter does not need to have a physical value.

With the parameter of *GAMM*, the "quasi-saturation" effect will be extended to the region with a high current. *GAMM* also can affect the dynamic behavior of the transistor through the capacitors C_{bcq} and C_{bcx}.

VO can determine the start of velocity saturation, which means a smooth region at the high-end of the "quasi-saturation" and also a reduction of the collector current.

HRCF is added to reflect an increase of the collector current with a higher voltage. The influence of this parameter will increase with the smaller parameter value.

QCO does not affect the DC performance of the transistor. But, it can affect the transit time and can be determined from S-parameters.

5. Transit time parameters

The extraction method for the transit time parameters is based on the following equation:

$$T_f = TF \cdot (1 + QTF \cdot q_1) \cdot \left[1 + XTF \cdot \left(\frac{I_{tf}}{I_{tf} + ITF} \right)^2 \cdot e^{\frac{V_{bci}}{1.44 \cdot VTF}} \right]. \qquad (5.11)$$

Except the parameter of *QTF*, we can use the extraction method analogous to that in the GP model. Usually, the procedure is split into two steps [188]. First, the

transistor is biased with $V_{BC} = 0$ to simplify the equation above. Then, the parameters of TF , XTF and ITF can be extracted. Second, V_{CE} is swept and the parameter VTF is calculated. During these two steps, the transistor must be biased beyond the "quasi-saturation" region.

For the small forward transport current I_{tf} , the equation above can be simplified as:

$$T_f \approx TF \cdot (1 + QTF \cdot q_1) \ . \tag{5.12}$$

The parameters of TF and QTF now can be determined.

After the determination of all the transit time parameters, the parameters of RBI and WBE must be optimized again and the parameters of QCO and $GAMM$ need to be tuned.

5.6 Parameter Converting Method from the GP Model to the VBIC Model

Nowadays, two difficult situations are often faced by IC designers. One is the model availability versus model familiarity, and the other is the model complexity versus model simulation efficiency. Therefore, it is highly desirable that one model can be converted to another and two "consistent" models can be provided for each technology. That is, a simplified version is used for fast simulations and an advanced version is used for detailed and critical predictions. In the bipolar transistor modeling, model parameter extraction for each model is usually performed independently based on separate standard electrical characterizations, such as DC, CV and bias dependent S-parameter measurements. This approach has few problems for simple models like the GP model, because relatively fewer model parameters are needed . However, it has problems for more advanced models, because an advanced model generally consists of

much more model parameters and often contains some conflicting parameters. So, an advanced model is always unstable and modeling engineers always feel frustrated if they extract the advanced model directly.

In this section, our new model extraction methodology is proposed in which an advanced model is extracted by going through a simplified one. A simplified model provides an excellent starting point for an advanced model. In particular, we present a new methodology of extracting the VBIC model by going through the GP model. First, the standard GP model is extracted in the standard way. Next, the GP model parameters are directly converted to those of the VBIC model. Local modifications are subsequently carried out for those parameters that are affected by different equations used in the two models. Finally, new model parameters with enhanced modeling features are introduced by evaluating the differences between measurement and simulation results.

5.6.1 Converting the GP model to the VBIC Model

In theory, the VBIC model is fully based on the GP model with two enhancements, namely, to improve the GP model by using more accurate equations, and to extend it by describing additional features. Based on this analysis, it is believed that there must exist a shortcut for extracting the VBIC model parameters "directly" from all the available GP model parameters instead of doing it from scratch . Therefore, we have practiced and developed a completely new approach to directly convert GP model parameters to those corresponding parameters in VBIC model. The details are summarized in Table 5.4.

In the above table, the column of "VBIC" lists all the VBIC model parameters and the column of "GP" shows the correlated GP model parameters if there are any. The modifications needed for converting the GP model to the VBIC model are listed in

the column of “Typical Converting”. If the advanced VBIC model parameters (marked by the sign of "-" in the GP column) are not assigned, their default values are used where their effects are disabled. It can be seen that some of the GP model parameters have been directly converted to the VBIC model and some of the GP model parameters still need further modifications. However, at least the reliable initial values of some VBIC model parameters can be obtained. In general, some of the GP model parameters need to be modified by some factors. So, we aimed to find out the corresponding converting formulas.

1. Main collector current source

The forward and reverse current emission coefficients *NF* and *NR* are kept constant in both models. However, due to the different base charge modulation model for q_b, transport saturation current *IS* in the VBIC model has to be modified and usually, it is smaller than that in the GP model. The exact value of the correcting factor can be easily calculated by evaluating the difference between simulation and measurement results.

2. Early voltage

The implementations of Early effect in the GP and VBIC models are so different that strictly speaking, the parameters cannot be converted directly. However, in general, the GP Early voltage parameters are larger than those of the VBIC model. So, it is recommended that the Early voltage should be converted with the half value of the corresponding GP model parameter and modified by “local ratio evaluation” technique which will be given in the next section.

3. Charge capacitance

The space charge capacitance is the same if the selector A_{ji} (i=*E,C,S*) is set to a negative value. All space charge capacitance parameters are converted directly.

Table 5.4 The proposed converting method from the GP model to the VBIC model

VBIC	GP	Typical Converting	Remarks
Main Collector Current Source			
IS	IS	IS*0.9	Transport saturation current IS in VBIC is smaller due to the different q_b modeling
NF	NF		Forward current emission coeff.
NR	NR		Reverse current emission coeff.
Early Modeling			
VEF	VAF	VAF*0.5	Early effect is modeled differently in two models. In general , Early voltage in VBIC model is smaller than that of the GP model
VER	VAR	VAR*0.5	
Webster Effect			
IKF	IKF	IKF*0.9	High-current roll-off is less effective in VBIC model
IKR	IKR	IKR*0.9	
Forward Base Current			
IBEI	IS/BF		In the VBIC model, the ideal B-E diode and non-ideal B-E leakage diodes are modeled independently
NEI	NF		
IBEN	ISE		
NEN	NE		
WBE	-	1.0	Distributed base parameter. It is set to one if no distributed base modeling
Reverse Base Current			
IBCI	IS/BR		In the VBIC model, the ideal B-C diode and non-ideal B-C leakage diodes are modeled independently
NCI	NR		
IBCN	ISC		
NCN	NC		
Weak Avalanche Current			
AVC1	-	0.15	
AVC2	-	20	
Parasitic Resistance			
RE	RE		
RBX	RBM		The bias-dependent base resistance is modeled differently in both models
RBI	-		
-	RB		
-	IRB		
RS	-		
RBP	-		
RCX	RC		Constant external collector resistor
Quasi-Saturation			
RCI	-	RC*10	VBIC has a modified Kull model implemented
GAMM	-	100p	
VO	-	1.5	
HRCF	-	33m	
QCO	-	1.0f	
Space Charge Capacitance			
CJE	CJE		
PE	VJE		
ME	MJE		
AJE	-	-0.5	Space charge model selector (-0.5 for the GP model)
CJC	CJC		
PC	VJC		
MC	MJC		
AJC	-	-0.5	Space charge model selector (-0.5 for the GP model)

(a)

VBIC	GP	Typical Converting	Remarks
AJS	-	-0.5	Space charge model selector (-0.5 for the GP model)
FC	FC	0.9	
Transit Time (Diffusion Capacitance) Modeling			
TF	TF	TF*0.25	VBIC model has smaller TF due to additional QTF parameter
XTF	XTF		
ITF	ITF		
VTF	VTF		
QTF	-	0.3	Describes the additional dependency of the transport time on q_b
TR	TR		
Excess Phase			
TD	PTF	TF*PTF*π/180	In the VBIC model, excess phase is implemented by a sub-circuit which is consistent between small-signal and transient analyses
Parasitic Capacitance			
CBEO	-		External overlap capacitance needs to be added manually in the GP model
CBCO	-		
Parasitic Substrate Transistor			
ISP	-		The GP model does not cover the substrate transistor
NFP	-		
WSP	-		Distributed factor for parasitic collector current control between V_{bci} and V_{bep}
IBEIP	-		NEIP=NCI
IBENP	-		NENP=NCN
IBCIP	-		
NCIP	-		
IBCNP	-		
NCNP	-		
IKP	-		
Temperature Mapping			
CTH	-	100p	The VBIC model includes a self-heating sub-circuit
RTH	-	200	
TAMB	-	TNOM	
TNOM	TNOM		
EA	EG		
EAIE	-		
EAIC	-		
EAIS	-		
EANE	-		
EANC	-		
EANS	-		
XRE	-		
XRB	-		
XRC	-		
XRS	-		
XVO	-		
XIS	XTI		
XII	XTB		
XIN	XTB		
XNF	-		
TAVC	-		

(b)

4. Diode currents

In the VBIC model, the ideal base current is not coupled to the transport current, so that *IBEI=IS/BF* and *IBCI=IS/BR*. The GP model parameters of the non-ideal or recombination section of the base current can, however, be transferred directly to those corresponding parameters of the VBIC model.

5. Transit time parameters

If *QTF* is set as zero, the GP model parameters such as the transit time and the excess phase, can be transferred to the corresponding VBIC model parameters without any change. If *QTF* is introduced, *TF* will be reduced.

5.6.2 "Local Ratio Evaluation" Technique

Strictly speaking, our developed model conversion method in the section above cannot be applied to some of the model parameters accurately. Because some of it is based on our practical model extraction experience. Therefore, a new modeling technique, namely, " local ratio evaluation", is proposed. This new parameter extraction technique is very useful if the current values of the parameters are not too far away from their final values. The typical applications are (a) to determine a model parameter which is converted from other model (such as the VBIC model parameter from the GP model) by error correction, (b) to update an existing model for new wafer lot run which may have some shifts in technologies, (c) to extract models from similar wafers or chips for typical and worst models or statistical deviations , and (d) to perform model extraction for the same DUT under different temperature.

The key point is to avoid complex mathematical solutions and to avoid using optimization or manual tuning procedures. To demonstrate it and make it easier to understand, an example below, which is taken from real SiGe HBT modeling data, is

used to show how to extract the Early voltage *VEF* and transport saturation current *IS* in the VBIC model when they are converted from the corresponding parameters in the GP model (*VAF* and *IS*).

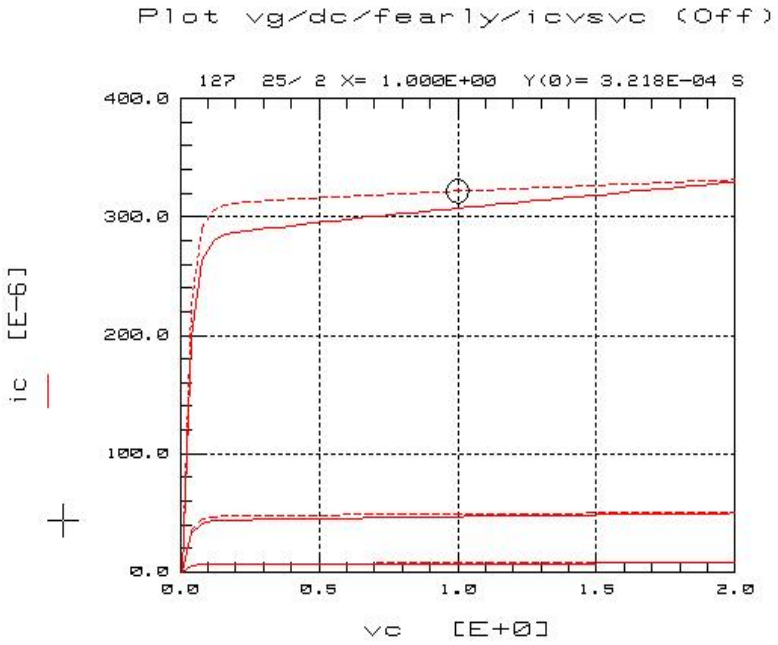

(a)

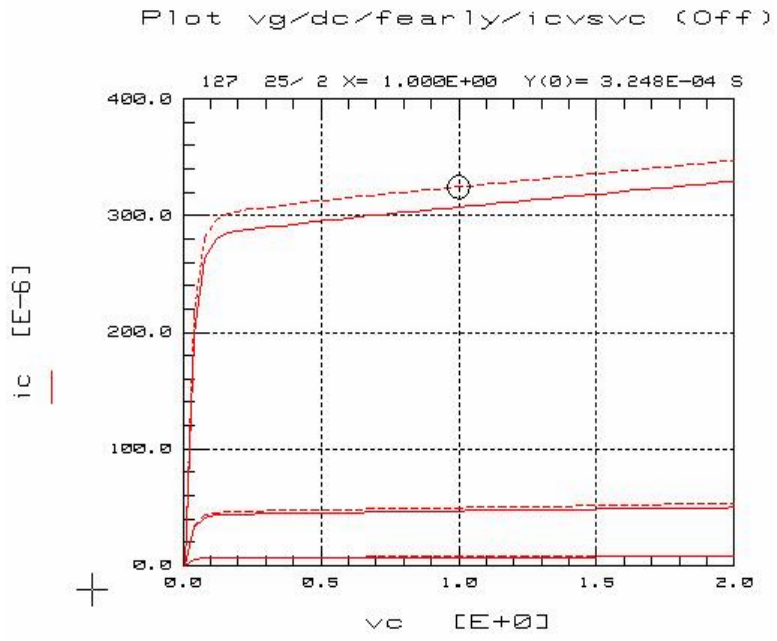

(b)

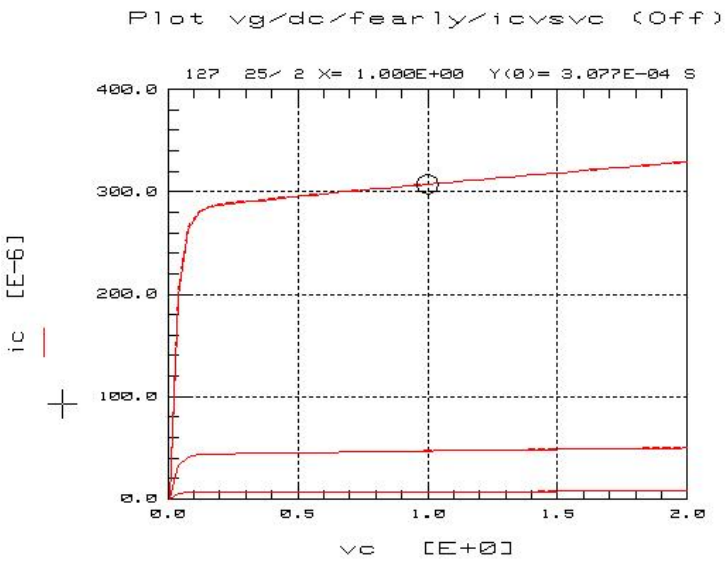

(c)

Figure 5.46. I-V characteristic of a SiGe HBT (solid line denotes measurement, dashed line denotes simulation with the VBIC model) (a) simulation with parameters directly converted from the GP model, (b) simulation after VEF correction by local ration evaluation technique, (c) simulation after IS correction .

Figure 5.46 (a) is the measured and simulated current-voltage characteristic of a SiGe HBT device. The solid line is measured data and dashed line is simulated results by the VBIC model whose parameters are converted directly from the GP model. Now, the simulation results are shifted from the measurement data, because the Early voltage modeling is different in both models. However, the converted parameter values for *VEF* and *IS* in the VBIC model can be corrected in our proposed way as follows.

1. Correction of *VEF*

It is well known that *VEF* will determine the slope of the I-V curve in the saturation region. So, we suggest to select any two points in one of the I-V curves in this region, then the new *VEF* (VEF^{new}) can be determined from :

$$VEF^{new} = VEF \cdot \frac{I_{c2}^{sim} - I_{c1}^{sim}}{I_{c2}^{mea} - I_{c1}^{mea}} \quad , \tag{5.13}$$

where the superscripts *sim* and *mea* denote simulated and measured data. After this correction, the new simulation result is shown in Figure 5.46 (b). The slopes for the simulation and measurement results are identical.

2. Correction of *IS*

Next, *IS* , which determines the height of the simulated current curve needs to be corrected. We recommend to select any one point in the saturation region. Then, the new *IS* (IS^{new}) can be determined from :

$$IS^{new} = IS \cdot \frac{I_c^{mea}}{I_c^{sim}}. \tag{5.14}$$

After this correction, the final simulation results fit the measurement data as shown in Figure 5.46 (c).

5.6.3 Experiments, Results and Discussions

The extraction procedure by using our new "local ratio evaluation" technique is implemented in Agilent IC-CAP modeling system with two equivalent circuits and two simulators for the GP and VBIC models which have been realized in a single model set-up.

Basic procedures are as follows:

1. First, the GP model is extracted with SPICE simulator and well-established extracting routines.
2. Next, the GP model parameters are directly converted to the corresponding parameters in the VBIC model when all the other VBIC advanced features are turned off. In this case, the VBIC model is equivalent to the GP model except for the different formulas used for normalized base charge q_b .

3. Then, by evaluating the difference between measurement and simulation results, the difference of q_b modeling is corrected by "local ratio evaluation" technique.
4. Finally, new features, such as quasi-saturation effect, self-heating and weak avalanche breakdown are introduced sequentially.
5. The above steps can be sped up by using typical converting formulas listed in the column 3 of Table 5.4.

The experimental results are presented in Figures 5.47-5.51. Figure 5.47 shows typical SiGe HBT characteristics modeled with the GP model that has no quasi-saturation (QS), self-heating (ST) and weak avalanche (AV) modeling. Figure 5.47(a) is the standard output I-V characteristic that clearly shows the difference between measured data and simulated results in QS and AV regions. Figure 5.47(b) is the plot of external base-emitter voltage versus collector-emitter voltage with the base current as a changeable parameter. It also clearly shows the difference between measured data and simulated results in the ST region.

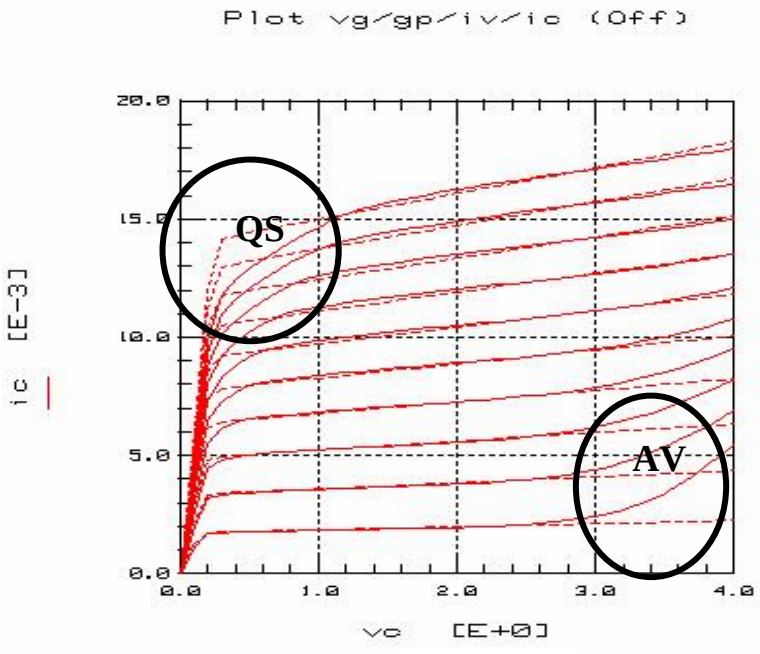

(a)

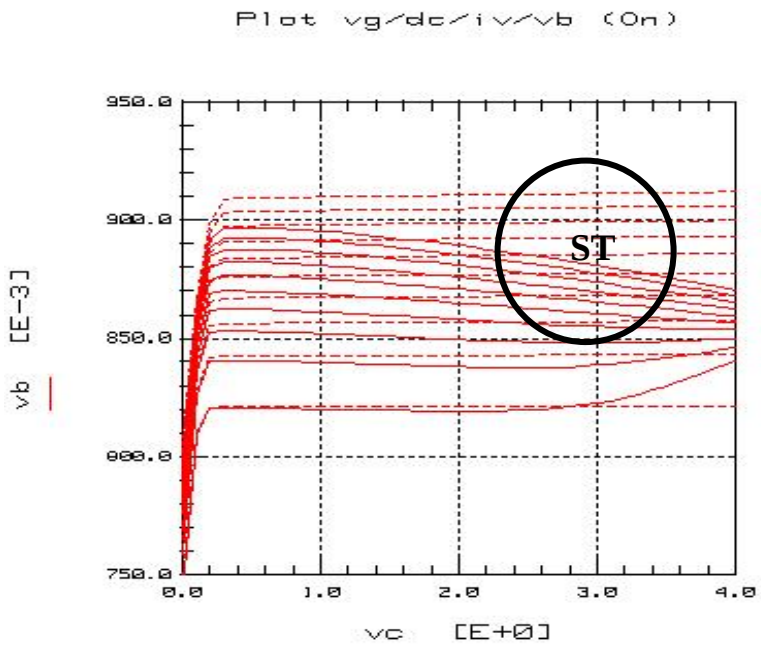

(b)

Figure 5.47. I-V characteristic and simulation with the GP model for a SiGe HBT device showing no quasi-saturation (QS), weak avalanche (AV), self-heating effect (ST).

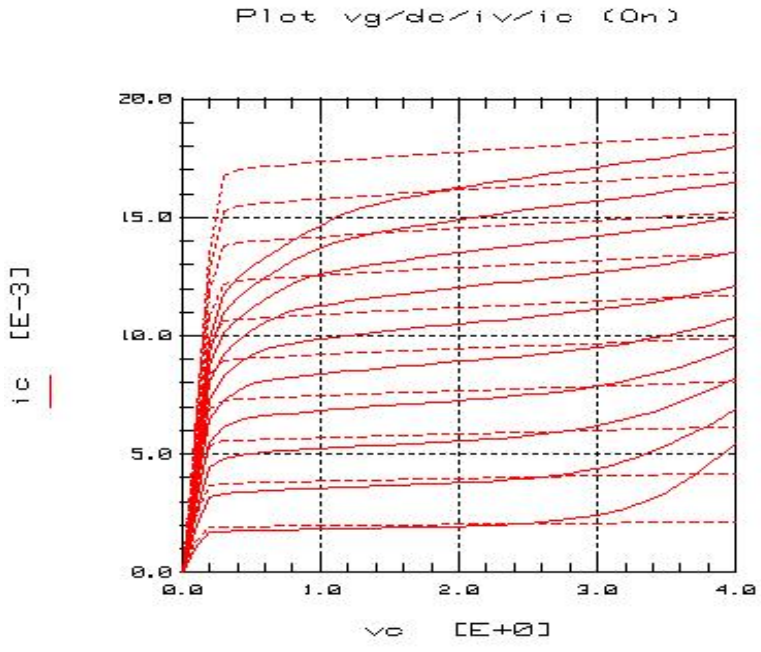

(a)

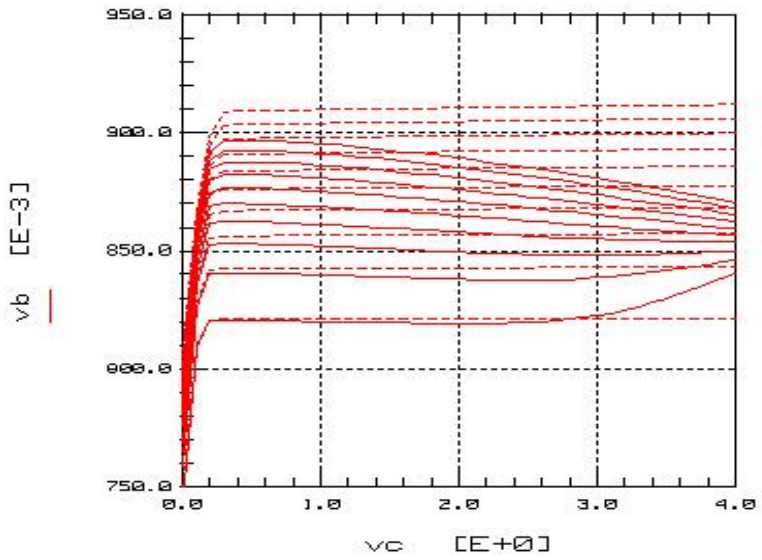

(b)

Figure 5.48. The same characteristic as Fig. 5.47, but simulation with the VBIC model. Model parameters are converted directly from the GP model , i.e. all advanced features in VBIC model are disabled.

In Figure 5.48 , the simulation is carried out using VBIC model whose parameters are converted directly from the GP model. All advanced features in VBIC model are disabled. It should produce the simulation results which are similar to those simulation results using the GP model. The difference in the QS region is due to the different Early voltage modeling used in the GP and VBIC models.

In Figure 5.49, VBIC model parameters are converted from those in the GP model with typical modifications or additional extensions as given in column 3 of Table 5.4. Especially, the parameters *IS*, *VEF* and *IKF* have been decreased, and the parameters *RCI*, *RBI* have been increased. It shows clearly that there are some improvements in the QS region, but there are still some differences in the ST region.

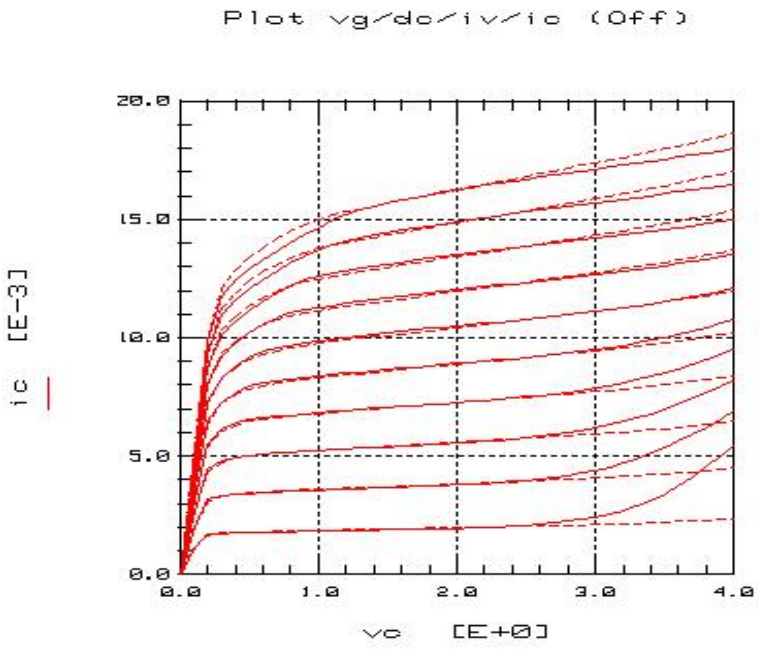

(a)

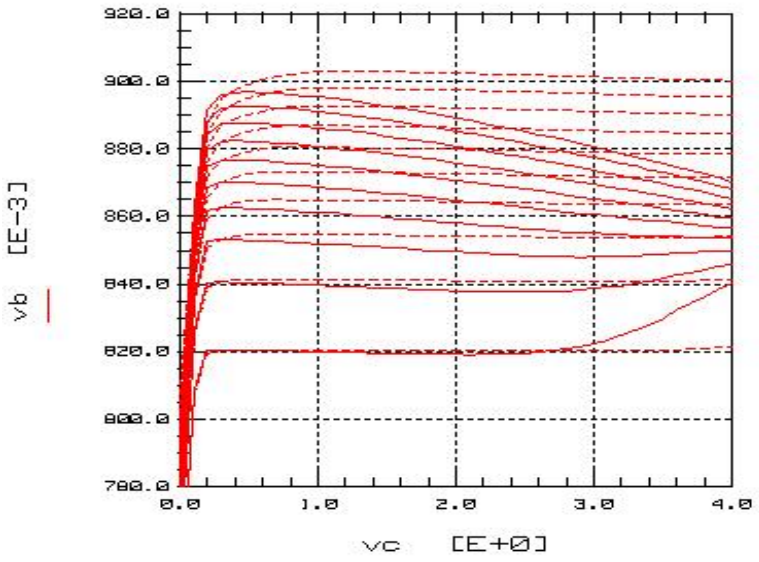

(b)

Figure 5.49. The same characteristic as Fig. 5.47, but the VBIC model parameters are converted from the GP model with typical modifications or additional extensions.

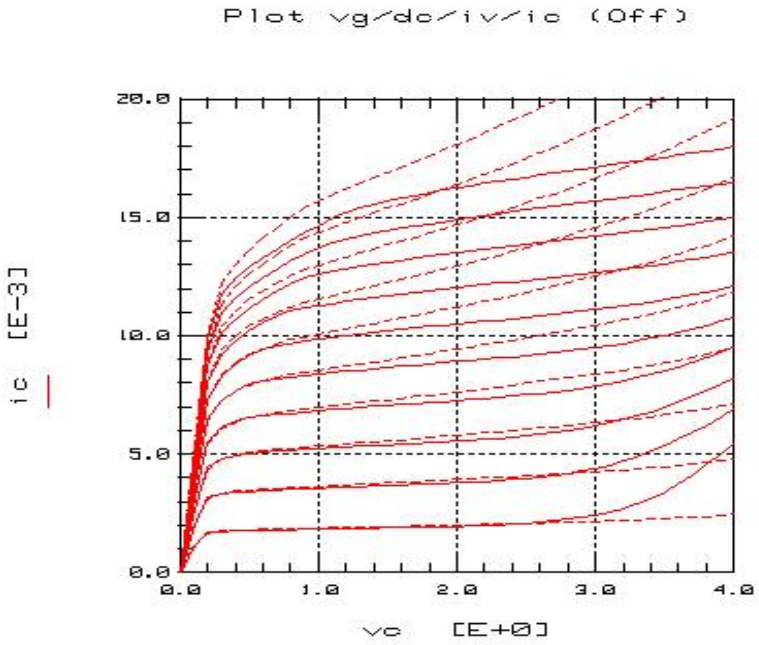

(a)

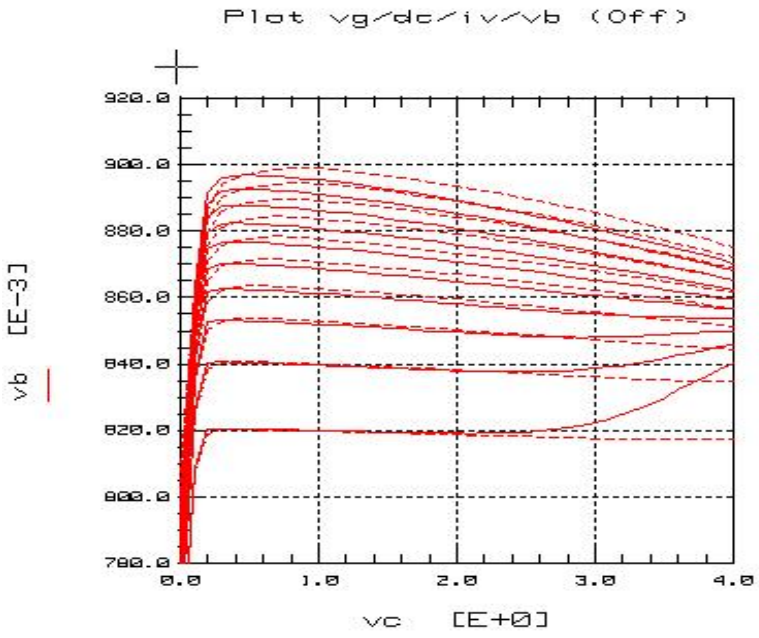

(b)

Figure 5.50. The same characteristic as Fig.5.47. Self-heating sub-circuit is included and locally corrected.

In Figure 5.50 , self-heating sub-circuit is included and locally corrected. However, the parameters *IS* and *VEF* are affected due to the self-heating effect. Therefore, the related model parameters need to be modified in the high-power region. At this stage, our developed "local ration evaluation" technique can be applied.

Figure 5.51 shows the results after all the corrections in the above steps. The QS and ST regions are well modeled. However, the weak avalanche breakdown effect cannot be modeled correctly in both high and low current AV regions simultaneously. We find out that it is due to the limitation of AV model in the VBIC model and the related discussion on this issue will be carried out in Section 5.7.

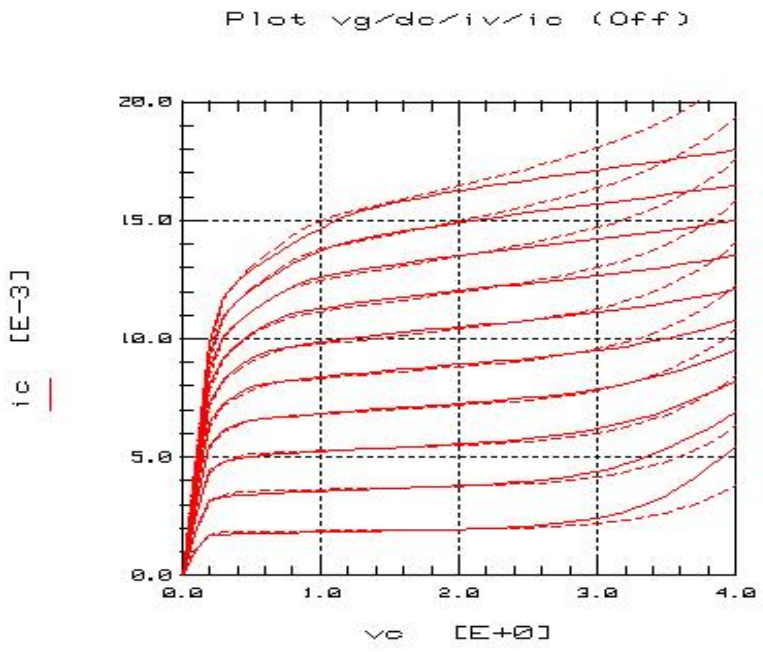

(a)

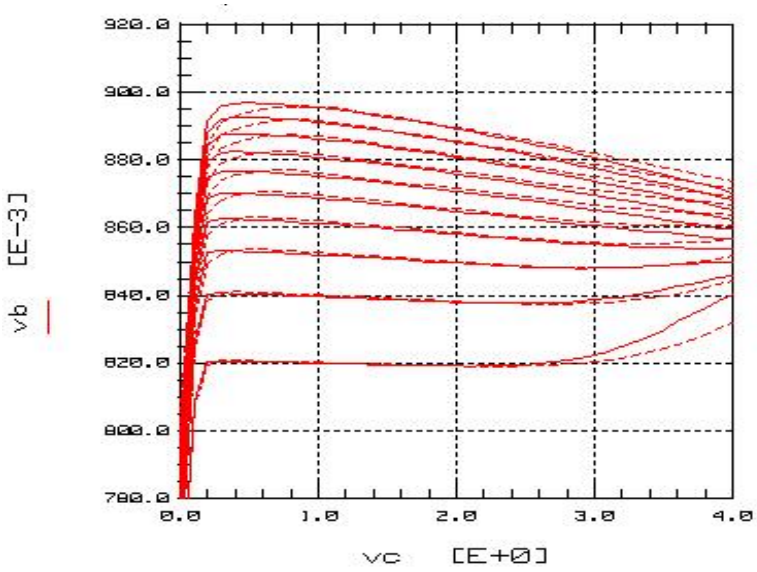

(b)

Figure 5.51. The final IV characteristic and simulation with the VBIC model in which QS, AV and ST effects are included.

In conclusion, in this section, based on the fact that the VBIC model is a direct enhancement and extension of the GP model, we have presented a novel approach – "local ratio evaluation" technique to obtain VBIC model parameters based on the GP model parameters. The detailed experimental procedures have been provided and excellent fit between some measured and simulated data has been obtained. The practical benefits of this work are: (a) Two models are extracted at the same time. The GP model can be used as a simplified version and the VBIC model as an advanced version. (b) There is less frustration in advanced model extraction by first going through the simple one. (c) It is possible to generate a VBIC model from an existing GP model by simple conversion formulas.

5.7 An Improved HBT Avalanche Breakdown Model

The Heterojunction Bipolar Transistors (HBT) has emerged recently as a promising candidate for power amplifier application in complex-modulation systems [191]. In such an application, device breakdown voltage is one of the critical specifications. Therefore, the avalanche multiplication in both III-V and SiGe HBTs has received intensive research worldwide [192]-[208].

In the standard Gummel-Poon(GP) model, there is no avalanche breakdown model included to account for avalanche breakdown. In the more advanced bipolar models such as VBIC [55]-[56] , MEXTRAM [98], the avalanche model is based on the well-known Chynoweth's empirical law and local electric field derivation . In the HICUM model [198], however, the avalanche model was derived similar to that of MEXTRAM on the basis that breakdown is caused by the maximum local electric field and depends strongly on the device geometric parameters. One basic common assumption for all the above models is the weak avalanche, i.e. the generated avalanche current should be much smaller than the collector current source. This assumption may not hold for a HBT with a highly-doped base region.

5.7.1 Classification of Avalanche Multiplication Behaviors

From the DC characteristics of the HBT devices, three groups of avalanche breakdown characterization have been noted as shown in Figure 5.52:

Group A: almost constant breakdown voltage V_{bk} as shown in Figure 5.52 (a).

Group B: V_{bk} increases with increased collect current density as shown in Figure 5.52 (b).

Group C: V_{bk} decreases with increased collect current density as shown in Figure 5.52(c).

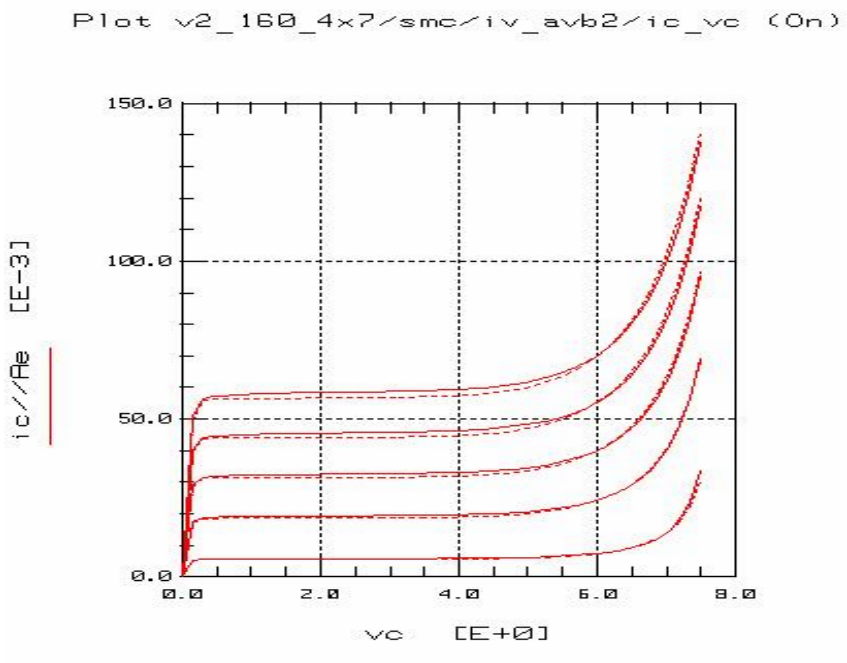
Plot v2_160_4x7/smc/iv_avb2/ic_vc (On)
ic//Ae [E-3]
150.0
100.0
50.0
0.0
0.0
2.0
4.0
6.0
8.0
Vc [E+0]

(a)

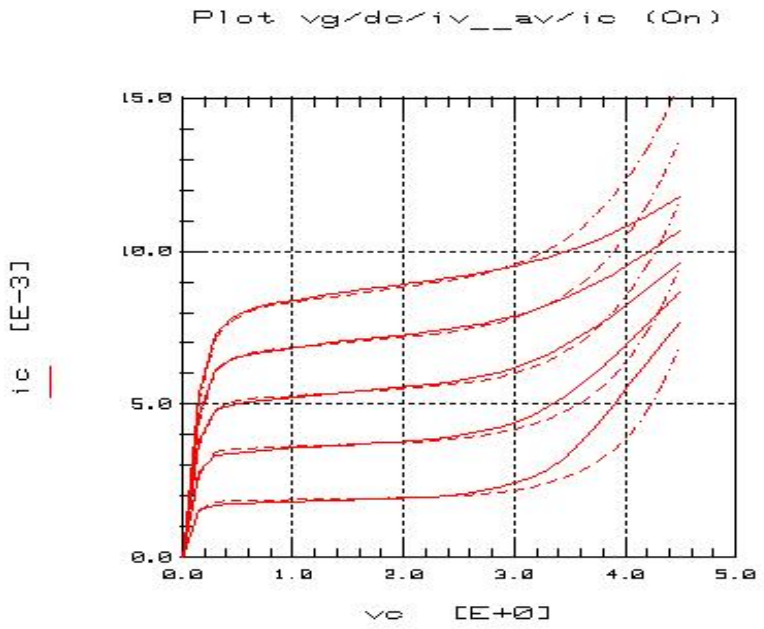
Plot vg/dc/iv__av/ic (On)
ic [E-3]
15.0
10.0
5.0
0.0
0.0
1.0
2.0
3.0
4.0
5.0
Vc [E+0]

(b)

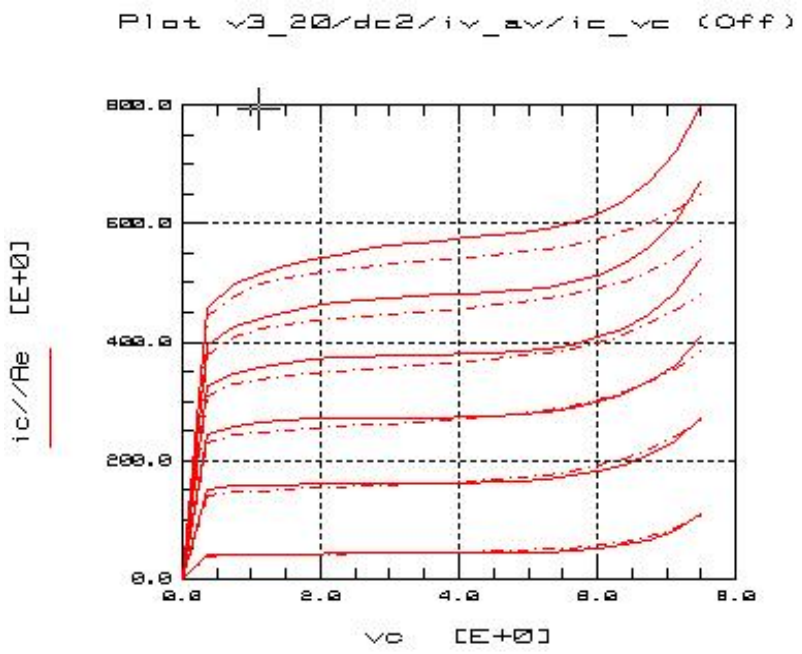

(c)

Figure 5.52. Three kinds of avalanche breakdown behaviors in HBT device (solid lines are measured data, dashed lines are simulation results with the VBIC model) : (a) almost constant breakdown voltage V_{bk}, (b) V_{bk} increases with increased Ic, and (c) V_{bk} decreases with increased Ic.

In Figure 5.52, simulation with the VBIC model is also shown. It can be seen that the VBIC model fits well only for group A, which is the basic assumption weak avalanche breakdown model is based on.

In [178], the avalanche model is derived with the assumptions that collector current does not affect the electric field distribution in the depletion layer and the avalanche behavior of the high current is due to the temperature dependence of the avalanche parameter. Therefore, one more avalanche model parameter is needed which is extracted by thermal resistance measurement. In addition, as noted in [192], avalanche multiplication factor changes with current density in modern SiGe HBTs. It is therefore concluded that there is a need to model the avalanche behavior as a function of current density to accurately predict distortion in circuit simulation. To the

best of our knowledge, so far, no model in commercial EDA tool can predict these characteristics completely.

5.7.2 HBT Avalanche Breakdown Modeling Enhancement

As shown from Figure 5.45 (a), the VBIC model includes a weak avalanche current source for the base-collector junction (I_{gc}) to account for the onset of the avalanche current. It is essentially based on the MEXTRAM [98] avalanche model but the effect of base-collector current on the avalanche current is more explicitly included as follows:

$$I_{gc} = (I_{cc} - I_{bc}) \cdot AVC1 \cdot (PC - V_{bci}) \cdot \exp\left[- AVC2 \cdot (PC - V_{bci})^{MC-1}\right], \qquad (5.15)$$

where $AVC1, AVC2$ are constant avalanche model parameters, PC and MC are built-in potential and grading coefficient of the base-collector space charge capacitance, respectively. V_{bci} is the internal nodal voltage across the base-collector junction. $AVC1$ is an empirical parameter related to the ratio of avalanche current to collector current source while $AVC2$ is a parameter reflecting the maximum field in the base-collector depletion charge region. In the VBIC model, $AVC2$ is further considered to be linearly dependent on temperature,

$$AVC2(TEMP) = AVC2(TNOM) \cdot \left[1 + TAVC \cdot (TEMP - TNOM)\right] \quad , \qquad (5.16)$$

where *TAVC* is one of the temperature parameters in the VBIC model. The overall DC behavior is very sensitive to avalanche parameters $AVC1$ and $AVC2$. Therefore, they should be extracted by the data-fitting process from DC characterization. For safe operation, the base-emitter voltage should be kept constant and low enough. Meanwhile, base-collector voltage is slowly increased until the base current has significantly decreased due to avalanche effect. Following this, the base-emitter voltage or base current can be varied.

As discussed in the previous section, the avalanche modeling above in the VBIC model can only fit well for group A having a lower collector current density or weak avalanche, i.e. the avalanche current is much smaller than the collector current source. However, with a small modification to the existing VBIC model, both group B and C can be covered. From a data-fitting process, we realized that, if we vary either *AVC1* or *AVC2*, different curves in Figure 5.52(b) and Figure 5.52(c) can be fitted well. Furthermore, by analyzing the dependence of the resulted parameter values on the bias current density , we find out that the VBIC constant avalanche model parameter can be simply modified to the linear function of the bias current density as follows:

$$AVC2 = AVC2' - AVC3(I_{cc} - I_{bc}), \tag{5.17}$$

where *AVC2'* and *AVC3* are two new model parameters. In practice, I_{cc}, the collector current source, is the main portion of the collector current and is much larger than I_{bc} due to the high current gain in SiGe HBTs. Therefore, the parameter can be extracted by the following method . First, set $AVC3 = 0$, the model degrades into the original VBIC model form. Second, extract different values of *AVC2* using the least square method to fit curve characterization from the lowest to highest current region. Finally, substitute the resulted values into the above equation, the new model parameters $AVC2'$ and *AVC3* can be solved.

Based on our derived equation (5.17), we have also experienced that if parameter *AVC1* is modified to a current dependent one, similar results can be obtained. However, to maintain the physical meaning of the compact model, extending the parameter *AVC2* is preferred. The results are presented in Figures 5.53 and 5.54. Both measurement and simulation are carried out in commercial modeling package Agilent IC-CAP. Parameter extraction is implemented using IC-CAP Parameter Extraction Language (PEL) along with the build-in optimizer.

Figures 5.53 and 5.54 show typical results of modeling enhancement for device groups B and C. Solid lines are measurement data and dashed lines are simulation results with the VBIC model. Figures 5.53(a) and 5.54(a) give simulated results by using the original VBIC model with the constant *AVC1* and *AVC2*. Figures 5.53 (b) and 5.54(b) give simulated results with enhancement for parameter *AVC1* and Figures 5.53(c) and 5.54(c) give a better enhancement by defining *AVC2* as a current dependent parameter. From Figures 5.53 and 5.54, it has been proved that our developed avalanche modeling method can achieve a better fitting effect than the conventional VBIC model in the device avalanche breakdown region. It has also shown clearly that the method of "parameter *AVC2* is defined as linear current dependent" is better than the method of "parameter *AVC1* is defined as linear current dependent".

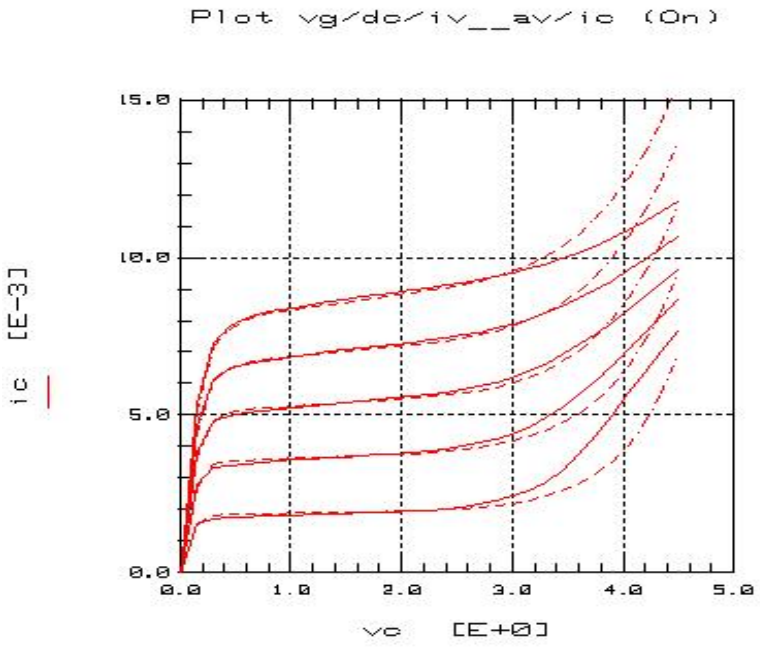

(a)

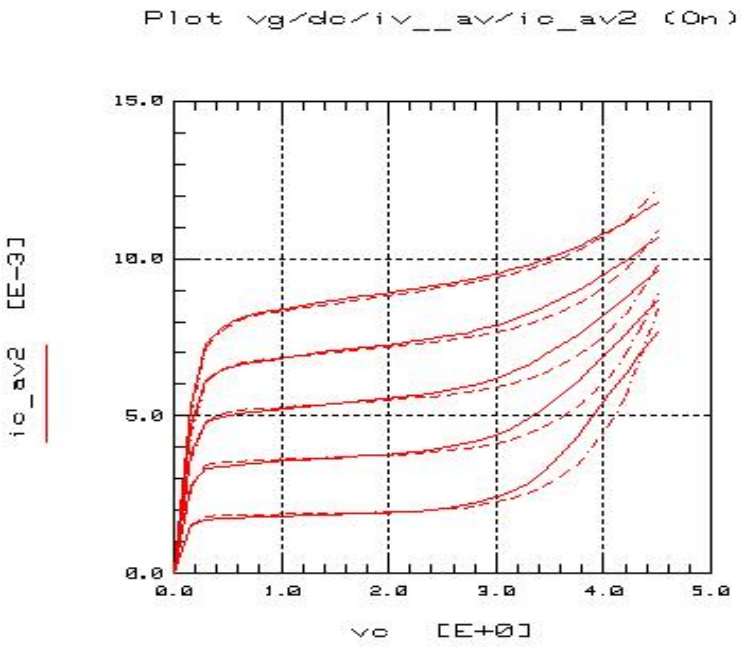

(b)

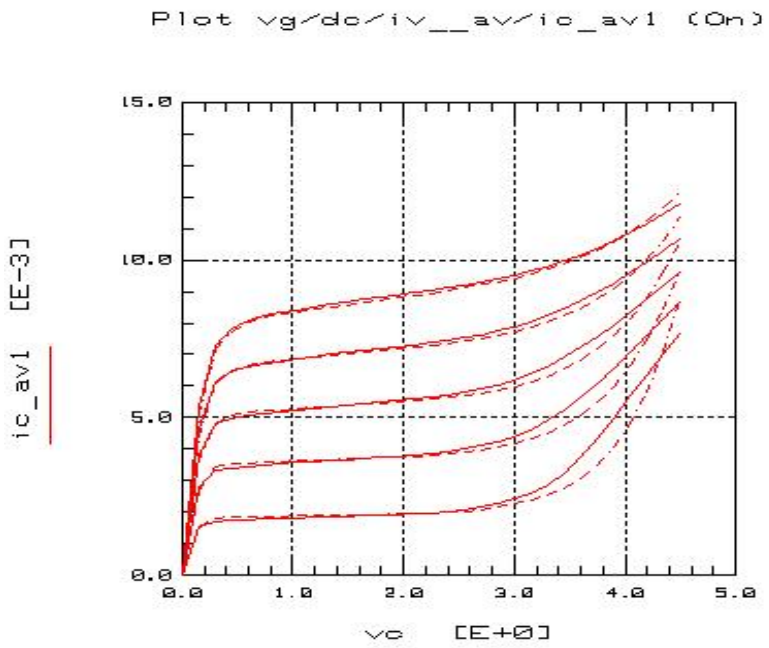

(c)

Figure 5.53. Avalanche multiplication characterization (solid lines) and modeling with the VBIC model (dashed lines) for device group B.
(a) Weak avalanche model parameters *AVC1* and *AVC2* in theVBIC model are constant
(b) Parameter *AVC1* is defined as linear current dependent
(c) Parameter *AVC2* is defined as linear current dependent

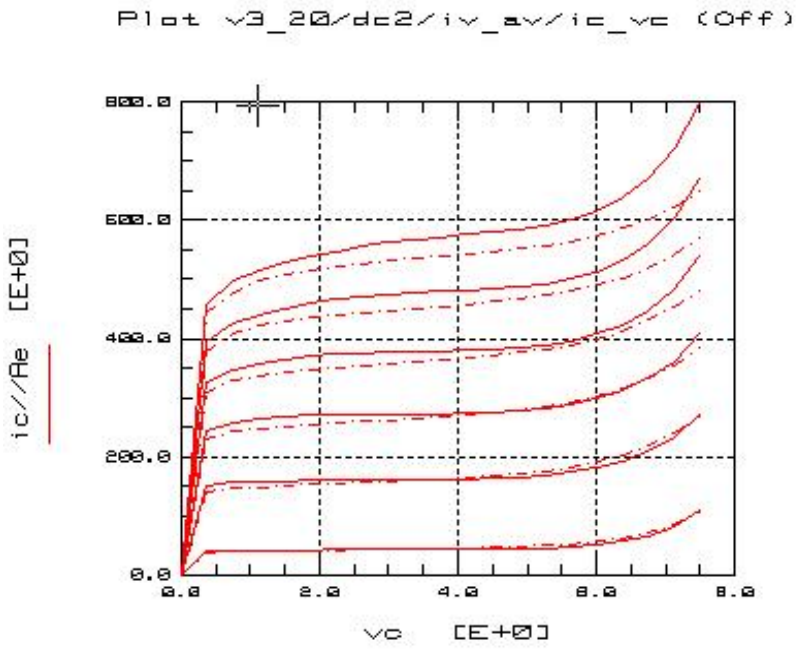
Plot v3_20/dc2/iv_av/ic_vc (Off)
800.0
600.0
400.0
200.0
0.0
ic//Ae [E+0]
0.0
2.0
4.0
6.0
8.0
Vc [E+0]

(a)

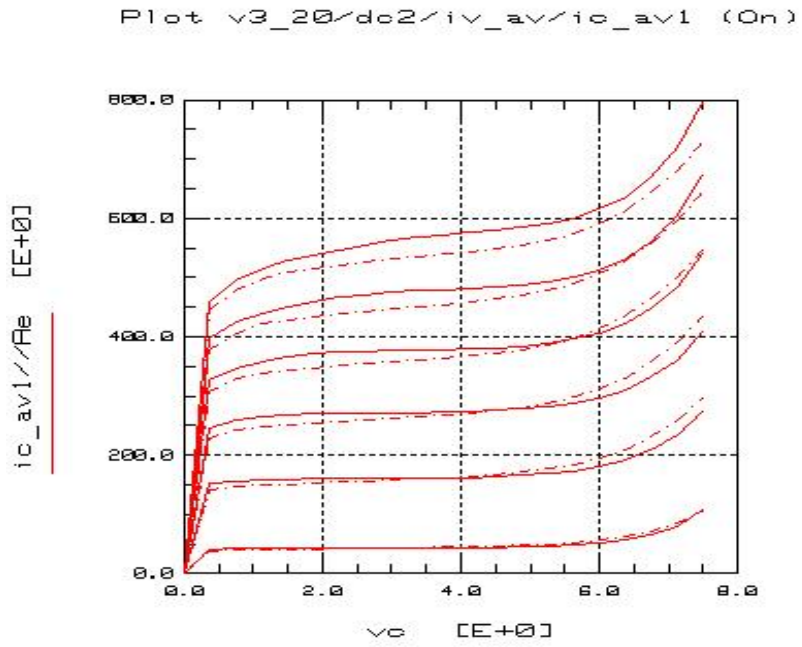
Plot v3_20/dc2/iv_av/ic_av1 (On)
800.0
600.0
400.0
200.0
0.0
ic_av1//Ae [E+0]
0.0
2.0
4.0
6.0
8.0
Vc [E+0]

(b)

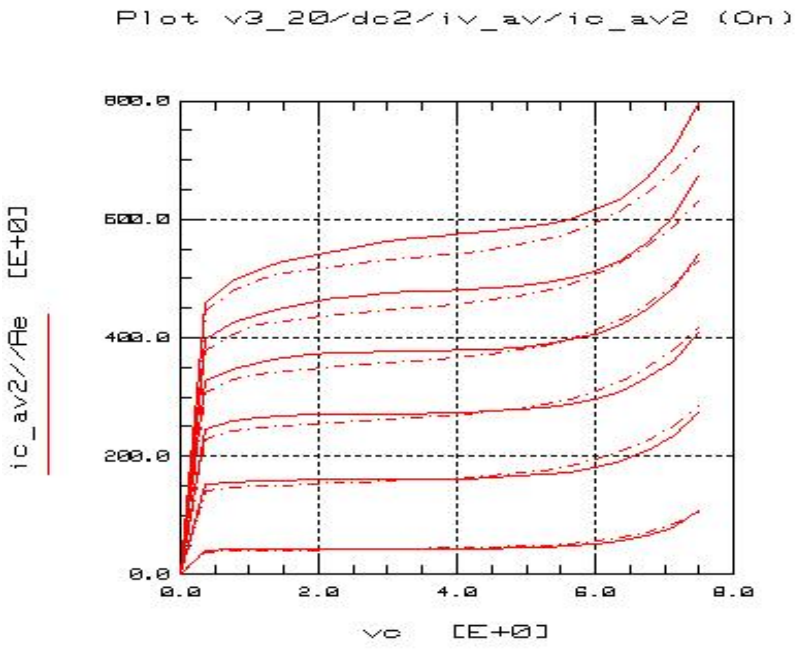

(c)

Figure 5.54. Avalanche multiplication characterization (solid lines) and modeling with the VBIC model (dashed lines) for device group C:
(a) Weak avalanche model parameters *AVC1* and *AVC2* in the VBIC model are constant
(b) Parameter *AVC1* is defined as linear current dependent
(c) Parameter *AVC2* is defined as linear current dependent

In conclusion, an empirical enhancement of the VBIC avalanche multiplication model is developed. By simply replacing a constant avalanche model parameter with a linear current dependent parameter, the new model can predict well all the observed avalanche behaviors accurately. It extends the validity of the original model from low current density region or weak avalanche to high current density region that is more useful in today's HBT power applications. The simplicity allows its convenient implementation into the commercial modeling tools and the newly added model parameters can be extracted without any extra measurements.

5.8 Conclusion

In this chapter, the definitions and characteristics of the various large-signal models have been discussed. The GP model has been selected as the main basis for the HBT large-signal model development. The physical background, model structure and model parameter extraction strategy of the GP model have been analyzed. Some improved model parameter extraction methods have been proposed and discussed. A SiGe HBT amplifier with high gain and high linearity has been designed, fabricated and measured on the basis of the extracted HBT large-signal model. Finally, the model verifications on both the single device and the microwave integrated circuit levels have been performed. Therefore, the validity of the developed HBT large-signal model has been confirmed.

In this chapter, an improved HBT large-signal model based on the VBIC model has also been developed. The background of the VBIC model has been introduced and some unique model parameter extraction methods of the VBIC model have been discussed. To improve the performance of the conventional VBIC model, two novel approaches have been studied and applied for the VBIC model enhancement. It has shown that the developed "local ratio evaluation" technique is very useful in the practical model conversion from the GP model to the VBIC model. It has also been proved that the newly proposed avalanche breakdown model is able to predict the HBT avalanche breakdown characteristics more accurately.

CHAPTER 6

CONCLUSIONS

6.1 Conclusions

In this project, several new techniques for the characterization and modeling of heterojunction bipolar transistors (HBTs) have been investigated. A review of past publications numbering about 200 on the relevant research areas has been completed. The dissertation discusses in detail the small-signal characterization and modeling for HBTs in Chapters 2-4. Several novel methods for HBT small-signal modeling are proposed. The strong correlation between extrinsic and intrinsic HBT small-signal model elements is explicitly derived and then a new additional equation is obtained to reduce the number of unknowns for the optimization. Based on such a strong correlation and the additional equation, the efficiency and accuracy of model parameter extraction have been improved greatly. The generalized pencil-of- function (GPOF) method is studied thoroughly in Chapter 3. The GPOF method can be used to describe the high frequency performance of HBTs precisely. Besides, based on the GPOF method, a new approach for the HBT small-signal model parameter extraction is developed. It has been proven that the extracted model elements are reliable enough for the modeling procedures. In Chapter 4, the parasitic electromagnetic effects are taken into account in the newly proposed millimeter-wave HBT small-signal model. Electromagnetic simulation is adopted to include the effects of the extrinsic metallic structure. Also, the “local access point” and “multi-port connection” methods are used in this model. The fitting and prediction abilities of the model have been demonstrated.

In Chapter 5, the classifications and definitions of large-signal models have been fully discussed. In addition, the basic principle, relevant model equations and parameter extraction of the Gummel-Poon (GP) model have been studied in depth. A practical set of model parameter extraction methods is proposed and the complete experimental results are presented. ICCAP modeling software is used in the whole modeling procedure. The accuracy of the extracted GP model has been proven on the level of a single transistor. In order to further verify the correctness of the model, a 1800-2100MHz, high gain and high linearity SiGe HBT amplifier has been designed and fabricated on the basis of the model above. Measurement results, such as S-parameters, gain vs. input (output) power and IP_3, have demonstrated the validity of the model on the level of microwave integrated circuit.

The Vertical Bipolar Inter-Company (VBIC) model has also been discussed in Chapter 5. The basic principle, relevant model equations and parameter extraction of the VBIC model have been studied completely. In addition, two improvements on the conventional VBIC model, namely, “improved avalanche breakdown model” and “ converting technique from the GP to the VBIC model”, are proposed to enhance the performance of the VBIC model. In fact, our proposed techniques are very suitable for the practical VBIC model development.

6.2 Future Works

Although the comparisons of HBT small-signal and large-signal performance in the previous chapters have demonstrated good agreement between the simulation results by the proposed methods and the respective measurement data, there are still a few areas in which some improvements are needed. In the HBT empirical small-signal modeling, several more advanced and efficient optimization algorithms, such as

genetic and simulated annealing methods, should be studied. In the HBT distributed small-signal model for millimeter-wave applications, the determination of a suitable number of " local access points" and relevant matrix computation still require a more intensive study.

In the future research works, instead of packaged HBTs, chip-formed HBTs should be used in HBT large-signal model development. Also, special de-emdedding "short" and "open" patterns should be designed and fabricated to further enhance the measurement accuracy. Because of the limitations of experimental conditions, the circuit design and model verification based on the VBIC model have not been completed yet. In the future, the extraction of the more advanced HBT large-signal models, such as VBIC, MEXTRAM and HICUM models, should be undertaken and some improvements are still needed to describe the high frequency performance of various HBTs more precisely and comprehensively.

REFERENCES

[1] W.Shockley, U.S. Patent , No. 2,569,347, 1951.

[2] H.Kroemer, "Theory of a wide-gap emitter for transistors," Proc.IRE, vol.45, pp.1535-1537, 1957.

[3] H.Kroemer, " Heterostructure bipolar transistors and integrated circuits," Proc. IEEE, vol.70, pp.13-25, 1982.

[4] W.Liu, *Handbook of III-V heterojunction bipolar transistors.* New York, NY: John Wiley & Sons, 1998.

[5] J.J.Liou, *Principles and analysis of AlGaAs/GaAs heterojunction bipolar transistors.* Norwood, MA: Artech House,1996.

[6] F.Ali and A.Gupta (Eds.), *HEMTs and HBTs: devices, fabrication, and circuits.* Norwood, MA: Artech House, 1991.

[7] J.S.Yuan, *SiGe,GaAs and InP heterojunction bipolar transistors.* New York, NY: John Wiley & Sons, 1999.

[8] T.Itoh, G.Haddad and J.Harvey (Eds.), *RF technologies for low power wireless communications.* New York, NY: John Wiley & Sons, 2001 .

[9] J.S.Yuan, "Overview of SiGe technology modeling and application," in IEEE 1st International Symposium on Quality Electronic Design, 2000, pp. 67-72.

[10] G.Heftman, " SiGe's influence spreads to many applications," Microwaves & RF, vol.39, No.10, pp.29-40,2000.

[11] "Silicon/silicon germanium BiCMOS processes and circuit techniques for RFICs," IEEE MTT-S International Microwave Symposium Workshop Notes, 2000.

[12] D.L.Harame, D.C.Ahlgren, D.D.Coolbaugh, J.S.Dunn, G.G.Freeman, J.D.Gillis, R.A.Groves, G.N.Hendersen, R.A.Johnson, A.J.Joseph, S.Subbanna, A.M.Victor, K.M.Watson, C.S.Webster and P.J.Zampardi, "Current status and future trends of SiGe BiCMOS technology," IEEE Trans. Electron Devices, vol.48, No.11, pp.2575-2594,2001.

[13] C.Elliott, "Building the wireless Internet," IEEE Spectrum, vol.38, No.1, pp.14-16, 2001.

[14] M.J.Riezenman, " The rebirth of radio," IEEE Spectrum, vol.38, No.1, pp.62-64,2001.

[15] L.Geppert , " RF bridges to the network," IEEE Spectrum, vol.38, No.1, pp.69-71,2001.

[16] J.W.Graff, E.F. Schubert and A. Osinsky, " On the reduction of base resistance in GaN-based heterojunction bipolar transistors," in Proc. IEEE/Cornell Conference on High Performance Devices, 2000, pp.28-32.

[17] D.L. Pulfrey and S. Fathpour, "Performance Predictions for N-P-N $Al_xGa_{1-x}N$/GaN HBTs," IEEE Trans. Electron Devices, vol.48, pp.597-602, 2001.

[18] L.S.McCarthy, I.P.Smorchkova, H.Xing, P.Kozodoy, P.Fini, J.Limb, D.L.Pulfrey, J.S.Speck, M.J.W.Rodwell, S.P.DenBaars and U.K.Mishra, " GaN HBT: Toward an RF device," IEEE Trans. Electron Devices, vol.48, pp.543-551, 2001.

[19] J.J. Huang, M.Hattendorf, M.Feng, D.J.H.Lambert, B.S.Shelton, M.M.Wong, U.Chowdhury, T.G.Zhu, H.K.Kwon and R.D.Dupuis, " Temperature dependent common emitter current gain and collector-emitter offset voltage study in AlGaN/GaN heterojunction bipolar transistors," IEEE Electron Device Letters , vol.22, pp.157-159, 2001.

[20] B.S.Shelton, D.J.H.Lambert, J.J.Huang, M.M.Wong, U.Chowdhury, T.G.Zhu, H.K.Kwon, Z.L.Weber, M.Benarama, M.Feng, R.D.Dupuis, "Selective area growth and characterization of AlGaN/GaN heterojunction bipolar transistors by metalorganic chemical vapor deposition," IEEE Trans. on Electron Devices, vol.48, pp.490-494, 2001.

[21] M.F.Chang (Ed.), *Current trends in heterojunction bipolar transistors.* Singapore: World Scientific Publishing, 1996.

[22] P.M.Asbeck, F.M.C.Chang, K.C.Wang, G.J.Sullivan and D.T.Cheung, "GaAs-based heterojunction bipolar transistors for very high performance electronic circuits," Proc. IEEE, vol.81, No.12, pp.1709-1726,1993.

[23] C.T.M.Chang and H.T.Yuan, "GaAs HBT's for high-speed digital integrated circuit applications," Proc. IEEE, vol.81, No.12, pp.1727-1743,1993.

[24] B.K.Oyama and B.P.Wong, "GaAs HBT's for analog circuits," Proc. IEEE, , vol.81, No.12, pp.1744-1761, 1993.

[25] B.Bayraktaroglu ," GaAs HBT's for microwave integrated circuits," Proc. IEEE, , vol.81, No.12, pp.1762-1785,1993.

[26] D.M.Pozar, *Microwave Engineering, Second Edition.* New York, NY: John Wiley & Sons,1998.

[27] D.Costa, W.U. Liu and J.S.Harris, Jr., "Direct extraction of the AlGaAs/GaAs heterojunction bipolar transistor small-signal equivalent circuit," IEEE Trans. Electron Devices, vol.38, pp.2018-2024, 1991.

[28] U. Schaper and B.Holzapfl, "Analytical parameter extraction of the HBT equivalent circuit with T-like topology from measured S-parameters," IEEE Trans. Microwave Theory Tech., vol.43, pp.493-498, 1995.

[29] Y.Gobert, P.J.Tasker and K.H.Bachem, " A physical, yet simple, small-signal equivalent circuit for the heterojunction bipolar transistor," IEEE Trans. Microwave Theory Tech., vol.45, pp.149-153,1997.

[30] A. Samelis and D. Pavlidis , " DC to high-frequency HBT-model parameter evaluation using impedance block conditioned optimization," IEEE Trans. Microwave Theory Tech. vol.45, pp.886-897, 1997.

[31] J.M.M.Rios, L.M.Lunardi, S.Chandrasekhar and Y.Miyamoto, " A self-consistent method for complete small-signal parameter extraction of InP-based heterojunction bipolar transistors (HBT's)," IEEE Trans. Microwave Theory Tech., vol.45, pp.39-45, 1997.

[32] H.Ghaddab, F.M.Ghannouchi, F.Choubani and A.Bouallegue, "Small-signal modeling of HBT's using a hybrid optimization / statistical technique," IEEE Trans. Microwave Theory Tech. , vol.46, pp.292-298, 1998.

[33] M.Rudolph, R.Doerner and P.Heymann , " Direct extraction of HBT equivalent-circuit elements," IEEE Trans. Microwave Theory Tech., vol.47, pp.82-84, 1999.

[34] S.Bousnina, P.Mandeville, A.B.Kouki, R.Surridge and F.M.Ghannouchi, "A new analytical and broadband method for determining the HBT small-signal model parameters," in IEEE MTT-S Int. Microwave Symp. Dig., 2000, pp.1397-1400.

[35] R.Schultheis, N.Bovolon, J.E.Müller and P.Zwicknagl, "Modelling of heterojunction bipolar transistors (HBTs) based on Gallium Arsenide (GaAs)," International Journal of RF and Microwave Computer Aided Engineering , vol.10, pp.33-42, 2000.

[36] M.Agethen, S.Schüller, P.Velling, W.Brockerhoff and F.J.Tegude, " Consistent small-signal and RF-noise parameter modeling of carbon doped InP/InGaAs HBT," in IEEE MTT-S Int. Microwave Symp. Dig., 2001, pp.1765-1768.

[37] A.Cidronali, G.Collodi,A.Santarelli,G.Vannini, and G.Manes, " Small-signal distributed FET modeling through electromagnetic analysis of the extrinsic structure," in IEEE MTT-S Int. Microwave Symp. Dig., 1998, pp.287-290.

[38] E.Larique, S.Mons, D.Baillargeat, S.Verdeyme, M.Aubourg, R.Quéré, P.Guillon , C.Zanchi and J.Sombrin, " Linear and nonlinear FET modeling applying an electromagnetic and electrical hybrid software," IEEE Trans. Microwave Theory Tech., vol.47, pp. 915-918, 1999.

[39] A.Cidronali, G.Collodi, G. Vannini, A.Santarelli and G. Manes , " A new approach to FET model scaling and MMIC design based on electromagnetic analysis," IEEE Trans. Microwave Theory Tech., vol.47, pp. 900-907, 1999.

[40] A.Laloue, J.B.David, R.Quéré, B.Mallet-Guy, E.Laporte, J.F. Villemazet and M.Soulard, " Extrapolation of a measurement-based millimeter-wave nonlinear model of pHEMT to arbitrary-shaped transistors through electromagnetic simulations," IEEE Trans. Microwave Theory Tech., vol.47, pp. 908-914, 1999.

[41] C. M. Snowden ,"Large-signal microwave characterization of AlGaAs/GaAs HBT's based on a physics-based electrothermal model ," IEEE Trans. Microwave Theory Tech.,vol.45, pp.58-71,1997.

[42] S.Wilms and H. M. Rein, " Analytical high-current model for the transit time of SiGe HBTs," in IEEE Bipolar/BiCMOS Circuits and Technology Meeting, 1998, pp.199-202.

[43] K.M.Walter, B.Ebersman, D.A.Sunderland, G.D.Berg, G.G.Freeman, R.A.Groves, D.K.Jadus and D.L.Harame, " A scaleable statistical SPICE Gummel-Poon model for SiGe HBT's," IEEE J. Solid-State Circuits, vol. 33, pp. 1439-1444, 1998.

[44] M. Schröter and T.Y.Lee, " Physics-based minority charge and transit time modeling for bipolar transistors," IEEE Trans. Electron Devices, vol.46, pp.288-300, 1999.

[45] M.Rudolph, R.Doerner, K.Beilenhoff and P.Heymann, " Scalable GaInP/GaAs HBT large-signal model," in IEEE MTT-S Int. Microwave Symp. Dig., 2000, pp.753-756.

[46] F.X.Sinnesbichler and G. R. Olbrich, "Accurate large-signal modeling of SiGe HBTs ," in IEEE MTT-S Int. Microwave Symp. Dig., 2000, pp.749-752 .

[47] A.Garlapati and S.Prasad, " A unified model for single/multifinger HBTs including self-heating effects," IEEE Trans. Microwave Theory Tech., vol.49, pp.186-191,2001.

[48] S.V.Cherepko, M.S. Shirokov, J.C.M.Hwang and A.Brandstaedter, " Improved large-signal model and model extraction procedure for InGaP/GaAs HBTs under high-current operations," in IEEE MTT-S Int. Microwave Symp. Dig., 2001 , pp.671-674.

[49] T.K.Sarkar and O.Pereira, " Using the matrix pencil method to estimate the parameters of a sum of complex exponentials," IEEE Antennas and Propagation Magazine, vol.37, pp.48-55,1995.

[50] K.C.Gupta, R.Garg and R.Chadha , *Computer-aided design of microwave circuits*. Dedham, MA: Artech House, 1981.

[51] H.K. Gummel and H.C. Poon, "An integrated charge control model of bipolar transistors," Bell Syst. Tech. Journal, vol. 49, pp.827-852,1970.

[52] I.E.Getreu, *modeling the bipolar transistor*. Amsterdam: Elsevier Scientific, 1978.

[53] P. Antognetti and G.Massobrio (Eds.), *Semiconductor device modeling with SPICE*. New York : McGraw-Hill, 1988.

[54] C. McAndrew, J.Seitchik, D.Bowers, M.Dunn, M.Foisy, I.Getreu, M.McSwain, S.Moinian, J.Parker, P.van Wijnen and L.Wagner, "VBIC95: An improved vertical,

IC bipolar transistor model," in IEEE Bipolar/BiCMOS Circuits and Technology Meeting, 1995, pp.170-177.

[55] C. C. McAndrew, J.A.Seitchik, D.F.Bowers, M.Dunn, M.Foisy, I.Getreu, M.McSwain, S.Moinian, J.Parker, D.J.Roulston, M.Schröter, P.van Wijnen and L.F.Wagner, "VBIC95, the vertical bipolar inter-company model," IEEE J. Solid-State Circuits, vol. 31, pp. 1476-1483, 1996.

[56] F. Najm and L.Arledge, " VBIC95: An improved bipolar transistor model, " IEEE Circuits and Devices Magazine , vol. 12, pp. 11-15, 1996.

[57] D.Costa, W. Liu and J.S.Harris, Jr., " A new direct method for determining the heterojunction bipolar transistor equivalent circuit model," in IEEE Bipolar Circuits and Technology Meeting, 1990, pp.118-121.

[58] C.J. Wei and J.C.M.Hwang, "Direct extraction of equivalent circuit parameters for heterojunction bipolar transistors," IEEE Trans. Microwave Theory Tech., vol.43, pp.2035-2040, 1995.

[59] B.Li and S. Prasad , " Basic expressions and approximations in small-signal parameter extraction for HBT's" IEEE Trans. Microwave Theory Tech., vol.47, pp.534-539, 1999.

[60] B. Li, S.Prasad, L.W.Yang and S.C.Wang, " A semianalytical parameter-extraction procedure for HBT equivalent circuit," IEEE Trans. Microwave Theory Tech., vol.46, pp.1427-1435, 1998.

[61] S.J. Spiegel, D.Ritter, R.A.Hamm, A.Feygenson and P.R.Smith, "Extraction of the InP/GaInAs heterojunction bipolar transistor small-signal equivalent circuit," IEEE Trans. Electron Devices, vol.42, pp.1059-1064,1995.

[62] S.A.Maas and D.Tait, "Parameter-extraction method for heterojunction bipolar transistors" , IEEE Microwave Guided Wave Letters , vol.2, pp.502-504, 1992.

[63] B.L.Ooi, T.S.Zhou, and P.S.Kooi, "An efficient method for HBT model parameter extraction based on the correlation between extrinsic and intrinsic elements," International Journal of RF and Microwave Computer-Aided Engineering, vol.12, pp.311-319, 2002.

[64] R.J.Trew, U.K.Mishra, W.L.Pribble and J.F.Jensen, " A parameter extraction technique for heterojunction bipolar transistors," in IEEE MTT-S Int. Microwave Symp. Dig., 1989, pp.897-900.

[65] D.R.Pehlke and D.Pavlidis, "Evaluation of the factors determining HBT high-frequency performance by direct analysis of S-parameter data," IEEE Trans. Microwave Theory Tech., vol.40, pp.2367-2373, 1992.

[66] D.Wu, D.L.Miller, M.Fukuda and Y.H.Yun, " Unique determination of AlGaAs/GaAs HBT's small-signal equivalent circuit parameters." in Proc.IEEE GaAs IC Symp., 1993, pp.259-262.

[67] J.H.Shin, Y.Chung, Y.Suh and B.Kim, " Extraction of low-frequency noise model of self-aligned AlGaAs/GaAs heterojunction bipolar transistor," in IEEE MTT-S Int. Microwave Symp. Dig., 1996, pp.1309-1312.

[68] Y.Suh, E.Seok, J.-H Shin, B.Kim, D.Heo, A.Raghavan and J.Laskar , " Direct extraction method for internal equivalent circuit parameters of HBT small-signal hybrid-II model," in IEEE MTT-S Int. Microwave Symp. Dig., 2000, pp.1401-1404.

[69] S.Lee , "Fast and efficient extraction of HBT model parameters using multibias S-parameter sets," IEEE Trans. Microwave Theory Tech., vol.44, pp.1499-1502, 1996.

[70] T.S.Horng, J.M.Wu and H.H.Huang, " An extrinsic-inductance independent approach for direct extraction of HBT intrinsic circuit parameters," in IEEE MTT-S Int. Microwave Symp. Dig., 2001, pp.1761-1764.

[71] T.S.Horng, J.M.Wu and H.H.Huang, " An extrinsic-inductance independent approach for direct extraction of HBT intrinsic circuit parameters," IEEE Trans. Microwave Theory Tech. , vol.49, pp.2300-2305, 2001.

[72] R.Menozzi and A.Piazzi , " HEMT and HBT small-signal model optimization using a genetic algorithm," IEEE Workshop on High Performance Electron Devices for Microwave and Optoelectronic Applications, 1997, pp.13-18.

[73] R.Menozzi, M. Borgarino, J.Tasselli and A. Marty, " HBT small-signal model extraction using a genetic algorithm," in Proc.IEEE GaAs IC Symp., 1998, pp157-160.

[74] G.L.Bilbro, M.B.Steer, R.J.Trew, C.R.Chang and S.G.Skaggs, " Extraction of the parameters of equivalent circuits of microwave transistors using tree annealing," IEEE Trans. Microwave Theory Tech. , vol.38, pp.1711-1718, 1990.

[75] K.Shirakawa, H.Oikawa, T.Shimura, Y.Kawasaki, Y.Ohashi, T.Saito and Y.Daido, "An approach to determining an equivalent circuit for HEMT's," IEEE Trans. Microwave Theory Tech., vol. 43 , pp.499-503,1995.

[76] B.L.Ooi, M.S.Leong and P.S. Kooi, "A novel approach for determining the GaAs MESFET small-signal equivalent-circuit elements," IEEE Trans. Microwave Theory Tech., vol. 45, pp.2084-2088,1997.

[77] F.Lin and G.Kompa, "FET model parameter extraction based on optimization with multiplane data-fitting and bidirectional search---a new concept," IEEE Trans. Microwave Theory Tech., vol. 42 , pp.1114-1121,1994.

[78] K.Levenberg, "A method for the solution of certain problems in least squares," Quart.Appl.Math. vol.2, pp.164-168 , 1944.

[79] D.Marquardt, "An algorithm for least-squares estimation of nonlinear parameters," SIAM J.Appl.Math., vol.11, pp.431-441, 1963.

[80] B.L.Ooi, T.S.Zhou, and P.S.Kooi, " AlGaAs/GaAs HBT Model Estimation through the Generalized Pencil-of-Function Method," IEEE Trans. Microwave Theory Tech., vol. 49, pp.1289-1294,2001

[81] Y.Hua and T.K.Sarkar, "Generalized pencil-of-function method for extracting poles of an EM system from its transient response," IEEE Trans. Antennas and Propagation, vol.37, pp. 229-234, 1989.

[82] Y.Hua and T.K.Sarkar, "Matrix pencil method for estimating parameters of exponentially damped/undamped sinusoids in noise," IEEE Trans. Acoust., Speech, Signal Processing, vol.38, pp.814-824, 1990.

[83] Z.A Marićević, T.K.Sarkar, Y.Hua and A.R.Djordjević, "Time-domain measurements with the Hewlett-Packard network analyzer HP8510 using the matrix pencil method," IEEE Trans. Microwave Theory Tech., vol.39, pp. 538-547, 1991.

[84] Z.A Maricevic and T.K.Sarkar, "Application of matrix pencil technique to analysis of microstrip" in IEEE AP-S Int. Symp. Dig., 1995, pp.1506-1509.

[85] J.Ritter and F.Arndt, " Efficient FDTD/matrix-pencil method for the full-wave scattering parameter analysis of waveguiding structures," IEEE Trans. Microwave Theory Tech., vol.44, pp. 2450-2456,1996.

[86] G.H.Golub and C.F.Van Loan, *Matrix Computations.* Baltimore, MD: Johns Hopkins Univ., 1983.

[87] G.E.Forsythe, M.A.Malcolm and C.B.Moler, " Computer methods for mathematical computations," Englewood Cliffs, NJ: Prentice-Hall ,1977.

[88] K.Nagatomo, Y.Daido, M.Shimizu and N.Okubo, " GaAs MESFET characterization using least squares approximation by rational functions," IEEE Trans. Microwave Theory Tech., vol.41, pp. 199-205,1993.

[89] M.L.James, G.M.Smith, and J.C.Wolford, *Applied Numerical Methods for Digital Computation.* New York, NY: HarperCollins College Publishers, 1993.

[90] R.O.Grondin, S.M.El-Ghazaly and S.Goodnick, " A review of global modeling of charge transport in semiconductors and full-wave electromagnetics," IEEE Trans. Microwave Theory Tech., vol.47, pp. 817-829, 1999.

[91] S.M.Hammadi and S.M.El-Ghazaly, " Air-bridged gate MESFET: a new structure to reduce wave propagation effects in high-frequency transistors," IEEE Trans. Microwave Theory Tech., vol.47, pp. 890-899, 1999.

[92] A.Witzig, C.Schuster,P.Regli and W.Fichtner, " Global modeling of microwave applications by combining the FDTD method and a general semiconductor device and circuit simulator," IEEE Trans. Microwave Theory Tech., vol.47, pp. 919-928, 1999.

[93] R.Hajji, F.M.Ghannouchi and A.B. Kouki, "A systematic layout-based method for the modeling of high-power HBT's using the scaling approach," IEEE Trans. Electron Devices, vol.42, pp. 528-533, 1995.

[94] R.Hajji and F.M.Ghannouchi, "Small-signal distributed model for GaAs HBT's and S-parameter prediction at millimeter-wave frequencies," IEEE Trans. Electron Devices, vol.44, pp. 723-732, 1997.

[95] J.Dubouloy, JF.Villemazet, V.Grognet, M.Soulard, D.Pasquet and E.Bourdel, "New versatile model: accurate prediction and synthesis ability for arbitrary geometry FET," in IEEE MTT-S Int. Microwave Symp. Dig., 1998, pp.283-286.

[96] E.Larique, S.Mons, D.Baillargeat, S.Verdeyme, M.Aubourg, P.Guillon and R.Quere, "Electromagnetic analysis for microwave FET modeling," IEEE Microwave Guided Wave Letters, vol.8, pp.41-43, 1998.

[97] K.D.Ma, M.Chen, B.Houshmand,Y.Qian and T.Itoh, " Global time-domain full-wave analysis of microwave circuits involving highly nonlinear phenomena and EMC effects," IEEE Trans. Microwave Theory Tech., vol.47, pp. 859-866, 1999.

[98] H.C. de Graaff and F. M. Klaassen, *Compact transistor modelling for circuit design.* Wien, New York: Springer-Verlag , 1990.

[99] M.Andersson, Z.Xia, P.Kuivalainen and H.Pohjonen, " Compact $Si_{1-x}Ge_x/Si$ heterojunction bipolar transistor model for device and circuit simulation," IEE Proceedings Circuits, Devices and Systems,vol.142, pp.1-7, 1995.

[100] H.C., de Graaff, , and W.J. Kloosterman, " New formulation of the current and charge relations in bipolar transistor modelling for CACD purposes," IEEE Trans. Electron Devices, vol.32, pp.2415-2419, 1985.

[101] G.B.Hong , J. G.Fossum and M.Ugajin, " A physical SiGe –base HBT model for circuit simulation and design," in IEEE Int. Electron Devices Meeting Tech.Dig., 1992, pp.577-580.

[102] M.B.Das, "High-frequency performance limitations of millimetre-wave heterojunction bipolar transistors," IEEE Trans. Electron Devices, vol.35, pp.604-614, 1988.

[103] J.J.Liou, L.L.Liou, C.I.Huang and B.Bayraktaroglu, "A physics-based, analytical heterojunction bipolar transistor model including thermal and high-current effects ," IEEE Trans. Electron Devices, vol.40, pp.1570-1577, 1993.

[104] C.D.Parikh and F.A.Lindholm, " A new charge-control model for single- and double-heterojunction bipolar transistors," IEEE Trans. Electron Devices, vol.39, pp.1303-1311, 1992.

[105] B.R.Ryum and I.M.Abdel-Motaleb , "A Gummel-Poon model for abrupt and graded heterojunction bipolar transistors (HBTs)," Solid –State Electronics, vol.33, pp.869-880, 1990.

[106] C.N.Huang and I.M.Abdel-Motaleb, " Gummel-Poon model for single and double heterojunction bipolar transistors," IEE Proceedings-G Circuits, Devices and Systems, vol.138, pp.165-169, 1991.

[107] J.J.Liou and J.S.Yuan, " Physics-based large-signal heterojunction bipolar transistor model for circuit simulation," IEE Proceedings-G Circuits, Devices and Systems, vol.138, pp.97-103, 1991.

[108] J.J.X.Feng, D.L.Pulfrey, J.Sitch and R.Surridge, " A physics-based HBT SPICE model for large-signal applications," IEEE Trans. Electron Devices, vol.42, pp.8-14, 1995.

[109] V.Krozer, M.Ruppert, M.Schüssler, K.Fricke, W.Y.Lee and H.L.Hartnagel, " Calculation of the power capabilities of HBT amplifiers based on a new physical HBT model," International Journal of Microwave and Millimeter-Wave Computer-Aided Engineering, vol.6, pp.270-280, 1996.

[110] C. Sangiamsak and S.J.Harrold, " Physical property based HBT models for SPICE simulation," in IEEE 8th International Symposium on High Performance Electron Devices for Microwave and Optoelectronic Applications , 2000, pp.265-270.

[111] M.Schröter, " Bipolar transistor modeling for the design of high-speed ICs," *Lecture note for the course on " RF IC design for wireless communication systems,"* Lausanne, Switzerland, 1998.

[112] P.A.H. Hart, Ed., *Bipolar and bipolar-MOS integration.* Amsterdam , the Netherlands: Elsevier , 1994.

[113] K.W. Michaels and A.J.Strojwas, " A compact physically-based bipolar transistor model," in IEEE Bipolar Circuits and Technology Meeting, 1989, pp.242-245.

[114] M.Regis, O.Llopis, L.Escotte, R.Plana, A.Gruhle, T.J.Brazil, M.Chaubet and J.Graffeuil, " Nonlinear modelling of a SiGe HBT with applications to ultra low phase noise dielectric resonator oscillators," in IEEE MTT-S Int. Microwave Symp. Dig., 1999, pp.83-86.

[115] C.N.Rheinfelder, F.J.Beiβwanger and W.Heinrich, " Nonlinear modelling of SiGe HBT's up to 50 GHz," IEEE Trans. Microwave Theory Tech.,vol.45, pp.2503-2508,1997.

[116] C.Rheinfelder, M.Rudolph, F.Beiβwanger and W.Heinrich, " Nonlinear modelling of SiGe HBTs up to 50GHz," in IEEE MTT-S Int. Microwave Symp. Dig., 1997, pp.877-880.

[117] X.Zhang, G.Henderson and C.Souchuns, " An Accurate physics-based large-signal model for high power SiGe BJT's," in IEEE MTT-S Int. Microwave Symp. Dig., 1999, pp.435-438.

[118] L. Bengtsson, C.Hedenäs, D.Dawson and H.Zirath, " Large signal modelling of GaAs/AlGaAs HBT's with separation of the surface recombination current," Solid-State Electronics, vol.43, pp.2163-2172, 1999.

[119] M.E.Hafizi, C.R.Crowell and M.E.Grupen, " The DC characteristics of GaAs/AlGaAs heterojunction bipolar transistors with application to device modelling," IEEE Trans Electron Devices, vol. 37, pp.2121-2129, 1990.

[120] H.M.Rein, M. Schröter, A.Koldehoff and K.Wörner, " A semi-physical bipolar transistor model for the design of very-high-frequency analog ICs," in IEEE Bipolar/BiCMOS Circuits and Technology Meeting, 1992, pp.217-220.

[121] M.Y.Frankel and D.Pavlidis, " An analysis of the large-signal characteristics of AlGaAs/GaAs heterojunction bipolar transistors," IEEE Trans. Microwave Theory Tech., vol.40, pp.465-474,1992.

[122] D.A.Teeter, J.R.East and G.I.Haddad, " Large-signal HBT characterization and modelling at millimetre wave frequencies," IEEE Trans. Microwave Theory Tech. ,vol.41, pp.1087-1093,1993.

[123] M.E.Mokari, S.Ganesan and B.Blumgold, " Systematic non-linear model parameter extraction for microwave HBT devices," in IEEE Proceedings of the 36th Midwest Symposium on Circuits and Systems, 1993, pp. 1031-1036.

[124] M. Schröter, M.Friedrich and H.M.Rein, "A generalized integral charge-control relation and its application to compact models for silicon-based HBT's," IEEE Trans. Electron Devices, vol.40, pp.2036-2046, 1993.

[125] C.T.Dikmen, N.S. Doğan and M.A.Osman, " DC modelling and characterization of AlGaAs/GaAs heterojunction bipolar transistors for high-temperature applications," IEEE J. Solid-State Circuits, vol. 29, pp. 108-116, 1994.

[126] D.Wu , M. Fukuda and Y.H.Yun," A novel extraction method for accurate determination of HBT large-signal model parameters ," in IEEE MTT-S Int. Microwave Symp. Dig.,1995, pp.1235-1238.

[127] K.Yang, A.L.Gutierrez-Aitken, X.Zhang, P.Bhattacharya and G.I.Haddad, "An HSPICE HBT model for InP-based single HBT's," IEEE Trans. Electron Devices, vol.43, pp.1470-1472,1996.

[128] M.Friedrich and H.M.Rein," Analytical current-voltage relations for compact SiGe HBT models -- part I: the "idealized" HBT," IEEE Trans. Electron Devices, vol.46, pp.1384-1393, 1999.

[129] M.Friedrich and H.M.Rein," Analytical current-voltage relations for compact SiGe HBT models -- part II: application to practical HBT's and parameter extraction," IEEE Trans. Electron Devices, vol.46, pp.1394-1401, 1999.

[130] Q.M.Zhang, H.Hu, J.Sitch, R.K.Surridge and J.M.Xu, " A new large signal HBT model ," IEEE Trans. Microwave Theory Tech., vol.44, pp.2001-2009, 1996.

[131] C.J.Wei , J.C.M.Hwang, W.J.Ho and J.A.Higgins, " Large-signal modelling of self-heating and RF-breakdown effects in power HBTs ," in IEEE MTT-S Int. Microwave Symp. Dig., 1996, pp.1751-1754.

[132] C.J.Wei , J.C.M.Hwang, W.J.Ho and J.A.Higgins, " Large-signal modelling of self-heating, collector transit time, and RF-breakdown effects in power HBT's," IEEE Trans. Microwave Theory Tech., vol.44, pp.2641-2647, 1996.

[133] K.Lu , P. Perry and T.J.Brazil, " A new SPICE-type heterojunction bipolar transistor model for DC, microwave small-signal and large-signal circuit simulation," in IEEE MTT-S Int. Microwave Symp. Dig., 1994, pp.1579-1582.

[134] K.Lu , P.A.Perry and T.J.Brazil, " A new large-signal AlGaAs/GaAs HBT model including self-heating effects, with corresponding parameter-extraction procedure," IEEE Trans. Microwave Theory Tech., vol.43, pp.1433-1445,1995.

[135] K.Lu , X.Zhang and G.N.Henderson, " A simplified large-signal HBT model for RF circuit design," in IEEE MTT-S Int. Microwave Symp. Dig., 1998, pp.1607-1610.

[136] R.Hajji, A.B.Kouki, S.El-Rabaie and F.M.Ghannouchi,"Systematic DC/small-signal/large-signal analysis of heterojunction bipolar transistors using a new consistent nonlinear model, " IEEE Trans. Microwave Theory Tech., vol.44, pp.233-241, 1996.

[137] P.C.Grossman and J.Choma, Jr., " Large signal modelling of HBT's including self-heating and transit time effects," IEEE Trans. Microwave Theory Tech., vol.40, pp.449-464, 1992.

[138] T.R.Turlington, *Behavioral modeling of nonlinear RF and microwave devices.* Norwood , MA: Artech House, 1999.

[139] C. Christodoulou and M. Georgiopoulos, *Applications of neural networks in electromagnetics*. Norwood, MA: Artech House, 2001.

[140] Q.J. Zhang and K.C. Gupta, *Neural networks for RF and microwave design.* Norwood, MA: Artech House, 2000.

[141] V.B.Litovski, J.I.Radjenović, Ž.M.Mrčarica and S.Lj.Milenković, " MOS transistor modelling using neural network," Electronics Letters, vol.28, pp.1766-1768, 1992.

[142] A.H.Zaabab, Q.J.Zhang and M.Nakhla, " A neural network modeling approach to circuit optimization and statistical design," ," IEEE Trans. Microwave Theory Tech., vol.43, pp.1349-1358, 1995.

[143] F. Günes , F.Gürgen and H.Torpi, "Signal-noise neural network model for active microwave devices," IEE Proceedings Circuits, Devices and Systems,vol.143, pp.1-8, 1996.

[144] K. Shirakawa , M.Shimiz, N.Okubo and Y.Daido, " A large-signal characterization of an HEMT using a multilayered neural network," IEEE Trans.on Microwave Theory Tech.,vol.45, pp.1630-1633, 1997.

[145] F.Wang, and Q.J.Zhang, " Knowledge based neural models for microwave design," IEEE Trans. Microwave Theory Tech., vol.45, pp.2333-2343, 1997.

[146] A.H.Zaabab, Q.J.Zhang and M.S.Nakhla, " Device and circuit-level modeling using neural networks with faster training based on network sparsity," IEEE Trans. Microwave Theory Tech., vol.45, pp.1696-1704, 1997.

[147] S.M.S.Imtiaz, and S.M.El-Ghazaly, "Global modeling of millimeter-wave circuits: electromagnetic simulation of amplifiers," IEEE Trans. Microwave Theory Tech., vol.45, 1997, pp. 2208-2216.

[148] V.K.Devabhaktuni, C.Xi and Q.J.Zhang , "A neural network approach to the modeling of heterojunction bipolar transistors from S-parameter data," in Proc. European Microwave Conf., vol.1, 1998, pp.306-311.

[149] K.Shirakawa, M.Shimizu, N.Okubo and Y.Daido, " Structural determination of multilayered large-signal neural-network HEMT model," IEEE Trans. Microwave Theory Tech.,vol.46, pp.1367-1375, 1998.

[150] P. M. Watson, K. C. Gupta, and R. L. Mahajan , "Applications of knowledge-based artificial neural network modeling to microwave components," International Journal of RF and Microwave Computer-Aided Engineering, vol.9, pp.254-260, 1999.

[151] Y. Harkouss, J.Rousset, H.Chéhadé, E.Ngoya, D.Barataud and J.P.Teyssier, " The use of artificial neural networks in nonlinear microwave devices and circuits modeling: An application to telecommunication system design," International Journal of RF and Microwave Computer-Aided Engineering, vol.9, pp. 198-215, 1999.

[152] G. L. Creech, J. M. Zurada, " Neural network modeling of GaAs IC material and MESFET device characteristics," International Journal of RF and Microwave Computer-Aided Engineering, vol.9, pp. 241-253, 1999.

[153] S.Goasguen, S.M.Hammadi and S.M.El-Ghazaly, " A global modeling approach using artificial neural network," in IEEE MTT-S Int. Microwave Symp. Dig., 1999, pp.153-156.

[154] F.Wang, V. K. Devabhaktuni, C. Xi and Q.J. Zhang, " Neural network structures and training algorithms for RF and microwave applications," International Journal of RF and Microwave Computer-Aided Engineering, vol.9, pp. 216-240, 1999.

[155] F.Sischka, "Gummel-Poon bipolar model parameter extraction toolkit" Hewlett-Packard, Dept. HP-EEsof, 1998.

[156] T.H.Ning and D.D.Tang, " Method for determining the emitter and base series resistances of bipolar transistors," IEEE Trans. Electron Devices, vol.31, pp.409-412, 1984.

[157] T.Nakadai and K.Hashimoto, " Measuring the base resistance of bipolar transistors," in IEEE Bipolar Circuits and Technology Meeting, 1991, pp.200-203.

[158] M.Linder, F.Ingvarson, K.O.Jeppson, J.V.Grahn, S.L.Zhang and M.Östling, " On DC modeling of the base resistance in bipolar transistors," Solid-State Electronics, vol.44, pp.1411-1418, 2000.

[159] M.Jo and D.E.Burk, "An intrinsic base resistance model for low and high currents," IEEE Trans. Electron Devices, vol.37, pp.202-209, 1990.

[160] W.J.Kloosterman, J.C.J.Paasschens and D.B.M.Klaassen, "Improved extraction of base and emitter resistance from small signal high frequency admittance measurements," in IEEE Bipolar/BiCMOS Circuits and Technology Meeting, 1999, pp.93-96.

[161] J.Weng, J.Holz and T.F.Meister, " New method to determine the base resistance of bipolar transistors," IEEE Electron Device Letters, vol.13, pp.158-160, 1992.

[162] W.Thomann and S.G.Knorr, " An accurate technique for the direct measurement of the base spreading resistance of bipolar transistors," in IEEE Bipolar Circuits and Technology Meeting, 1991, pp.196-199.

[163] R.Gabl, M.Reisch and M.Pohl, " Improved extraction method for the emitter resistance of bipolar transistors," in IEEE Bipolar/BiCMOS Circuits and Technology Meeting, 1998, pp.211-214.

[164] S.J.Prasad, " A method of measuring base and emitter resistances of AlGaAs/GaAs HBTs," in IEEE Bipolar/BiCMOS Circuits and Technology Meeting, 1992, pp.204-207.

[165] D.Berger, N.Gambetta, D.Céli and C.Dufaza, " Extraction of the base-collector capacitance splitting along the base resistance using HF measurements," in IEEE Bipolar/BiCMOS Circuits and Technology Meeting, 2000, pp.180-183.

[166] A.Samelis, " Modeling the bias dependence of the base-collector capacitance of power heterojunction bipolar transistors," IEEE Trans. Microwave Theory Tech., vol.47, pp.642-645, 1999.

[167] M.Hattendorf , D.Scott, Q.Yang and M.Feng, " Method to determine intrinsic and extrinsic base-collector capacitance of HBTs directly from bias-dependent S-parameter data," IEEE Electron Device Letters, vol.22, pp.116-118, 2001.

[168] "HP ICCAP modeling software -- user's guide," Hewlett-Packard Company, 1997.

[169] F.Sischka, " The ICCAP characterization basics handbook," Agilent Technologies, Dept. EEsof-EDA, Munich, Germany, 2000.

[170] V.Aparin and C.Persico, " Effect of out-of-band terminations on intermodulation distortion in common-emitter circuits," in IEEE MTT-S Int. Microwave Symp. Dig., 1999, pp.977-980.

[171] K.W.Kobayashi, A.Gutierrez-Aitken, P.C.Grossman, L.Yang, E.Kaneshiro, T.R.Block, A.K.Oki and D.C.Streit, " Tunable linearity characteristics of a DC-3 GHz InP HBT active feedback amplifier," in Proc. IEEE GaAs IC Symp.,1999, pp.291-294.

[172] P.B.Kenington, *High-linearity RF amplifier design.* Norwood, MA: Artech House, 2000.

[173] A.Katz , " Linearization: reducing distortion in power amplifiers," IEEE Microwave Magazine, vol.2, pp.37-49, 2001.

[174] J. Sun and M.Y.W.Chia, " The novel programmable RF predistortion linearizer," in IEEE MTT-S Int. Microwave Symp. Dig., 2001, pp.809-812.

[175] K.L.Fong and R.G.Meyer, " High-frequency nonlinearity analysis of common-emitter and differential-pair transconductance stages," IEEE J. Solid-State Circuits, vol.33, pp.548-555, 1998.

[176] P.Vizmuller, *RF design guide: systems, circuits and equations.* Norwood, MA: Artech House, 1995.

[177] H. Stübing and H. M. Rein, "A compact physical large-signal model for high-speed bipolar transistors at high current densities-part I: one-dimensional model," IEEE Trans. Electron Devices, vol. 34, pp.1741-1751,1987.

[178] H. M. Rein and M. Schröter, "A compact physical large-signal model for high-speed bipolar transistors at high current densities- part II: two-dimensional model and experimental results," IEEE Trans. Electron Devices, vol. 34 , pp. 1752-1761, 1987.

[179] H.Jeong and J.G.Fossum, " A charge-based large-signal bipolar transistor model for device and circuit simulation," IEEE Trans. Electron Devices, vol.36, pp.124-131, 1989.

[180] W.J. Kloosterman and H. C. de Graaff, " Avalanche multiplication in a compact bipolar transistor model for circuit simulation," IEEE Trans. Electron Devices, vol.36, pp.1376-1380, 1989.

[181] G.Neaves, J.White, M.Burnham, A.Zlotnicka and R.Pryor, " Characterization of low VAR bipolar transistors using a revised SPICE simulation," in IEEE Bipolar/BiCMOS Circuits and Technology Meeting, 1992, pp.229-232.

[182] Y. Dai and J. S. Yuan , " Current-dependent collector resistance of the bipolar transistor in quasi-saturation," IEE Proceedings Circuits, Devices and Systems, vol.145, pp. 66-70, 1998.

[183] G.M.Kull, L.W.Nagel, S.W.Lee, P.Lloyd, E.J.Prendergast, and H.Dirks, " A unified circuit model for bipolar transistors including quasi-saturation effects," IEEE Trans. Electron Devices, vol.32, pp.1103-1113, 1985.

[184] W.J. Kloosterman and H. C. de Graaff, " Avalanche multiplication in a compact bipolar transistor model for circuit simulation," in IEEE Bipolar Circuits and Technology Meeting, 1988, pp.103-106.

[185] P.B.Weil and L.P.Mcnamee, "Simulation of excess phase in bipolar transistors," IEEE Trans. Circuits and Systems, vol.25, pp.114-116, 1978.

[186] C.C.McAndrew, B.K.Bhattacharyya, and O.Wing, " A C_∞-continuous depletion capacitance model," IEEE Trans. Computer-aided Design of Integrated Circuits and Systems, vol.12 , pp.825-828, 1993.

[187] L.J.Turgeon and J.R.Mathews, " A bipolar transistor model of quasi-saturation for use in computer aided design (CAD)," in IEEE Int. Electron Devices Meeting Tech.Dig., 1980, pp.394-397.

[188] F. Sischka, *The IC-CAP Modeling Reference Book*, Dept. HP-EEsof, Hewlett-Packard Company, 1998.

[189] C.C.McAndrew and L.W.Nagel, " Early effect modeling in SPICE," IEEE J. Solid-State Circuits, vol.31, pp. 136-138, 1996.

[190] C.C.McAndrew and L.W.Nagel, " SPICE Early modelling," in IEEE Bipolar/BiCMOS Circuits and Technology Meeting, 1994, pp.144-147.

[191] U.Erben, M.Wahl, A.Schüppen and H.Schumacher, "Class-A SiGe HBT power amplifiers at C-band frequencies," IEEE Microwave and Guided Wave Letters, vol.5, pp. 435-436, 1995.

[192] H.Jeong and J.G.Fossum, " Modeling impact ionization in advanced bipolar transistors for device/circuit simulation," in IEEE Bipolar Circuits and Technology Meeting, 1988, pp.107-110.

[193] J. J. Chen, G.B.Gao, J.I.Chyi and H.Morkoc, "Breakdown behavior of GaAs/AlGaAs HBT's," IEEE Trans. Electron Devices, vol. 36, pp. 2165-2172, 1989.

[194] T.Lackner, " Avalanche multiplication in semiconductors: a modification of Chynoweth's law," Solid-State Electronics, vol.34, pp.33-42, 1991.

[195] G.A.M.Hurkx, D.B.M.Klaassen and M.P.G.Knuvers, " A new recombination model for device simulation including tunneling," IEEE Trans. Electron Devices, vol.39, pp.331-338, 1992.

[196] C.H.Díaz and S.M.Kang, " New algorithms for circuit simulation of device breakdown," IEEE Trans. Computer-aided Design of Integrated Circuits and Systems, vol.11, pp.1344-1354, 1992.

[197] G.B.Hong and J.G.Fossum, " Implementation of nonlocal model for impact-ionization current in bipolar circuit simulation and application to SiGe HBT design optimization," IEEE Trans. Electron Devices, vol.42, pp.1166-1173, 1995.

[198] M. Schröter, Z.Yan, T.Y.Lee and W.Shi, "A compact tunneling current and collector breakdown model," in IEEE Bipolar/BiCMOS Circuits and Technology Meeting, 1998, pp. 203-206.

[199] R.Anholt, " Physical compact collector-emitter breakdown model for heterojunction bipolar transistors," Solid-State Electronics, vol.41, pp.1735-1737, 1997.

[200] J. S. Hamel, "Separating the influences of neutral base recombination and avalanche breakdown on base current reduction in SiGe HBT's," IEEE Trans. Electron Devices, vol. 44, pp. 901-903, 1997.

[201] R. M. Flitcroft, J.P.R.David, P.A.Houston and C.C.Button, "Avalanche multiplication in GaInP/GaAs single heterojunction bipolar transistors," IEEE Trans. Electron Devices, vol. 45, pp. 1207-1212, 1998.

[202] G. Niu, J.D.Cressler, U.Gogineni and D.L.Harame, "Collector-base junction avalanche multiplication effects in advanced UHV/CVD SiGe HBT's," IEEE Electron Device Letters, vol.19, pp. 288-290, 1998.

[203] M.S.Peter, J.W.Slotboom and D.Terpstra, " Impact ionization and neutral base recombination in SiGe HBT's," in IEEE Bipolar/BiCMOS Circuits and Technology Meeting, 1999, pp.58-61.

[204] G. Niu, J.D.Cressler, S.Zhang,U.Gogineni and D.C.Ahlgren, "Measurement of collector-base junction avalanche multiplication effects in advanced UHV/CVD SiGe HBT's," IEEE Trans. Electron Devices, vol. 46, pp. 1007-1015, 1999.

[205] W.J.Kloosterman, J.C.J.Paasschens and R.J.Havens, " A comprehensive bipolar avalanche multiplication compact model for circuit simulation," in IEEE Bipolar/BiCMOS Circuits and Technology Meeting, 2000, pp.172-175.

[206] J.Scott and T.Low, " Avalanche breakdown in HBTs: variation with collector current and effect on linearity," in Proc. IEEE GaAs IC Symp., 2000, pp. 237-240.

[207] H. Wang and G.I.Ng, "Avalanche multiplication in InP/InGaAs double heterojunction bipolar transistors with composite collectors, " IEEE Trans. Electron Devices, vol. 47, pp. 1125-1133, 2000.

[208] S.Joshi, R.Ida, P.Givelin and E.Rosenbaum, " An analysis of bipolar breakdown and its application to the design of ESD protection circuits," in IEEE 39th Annual International Reliability Physics Symposium, 2001, pp.240-245.

APPENDIX A

The Major Equations in the GP Model

Table A.1 A list of the GP model parameters

DC operation

Name	Parameter Explanation
IS	Transport saturation current
XTI	Temperature exponent for effect on IS
E_g	Energy gap for temperature effect on IS
BF	Ideal forward maximum beta (DC current gain)
BR	Ideal reverse maximum beta (DC current gain)
XTB	Forward and reverse beta temperature coefficient
VAF	Forward Early voltage
VAR	Reverse Early voltage
NF	Forward current emission coefficient
NR	Reverse current emission coefficient
NE	Base-emitter leakage emission coefficient
NC	Base-collector leakage emission coefficient
ISE	Base-emitter leakage saturation current
ISC	Base-collector leakage saturation current
IKF	Knee current when forward beta at high current roll-off
IKR	Knee current when reverse beta at high current roll-off

Ohmic parasitics

Name	Parameter Explanation
RB	Zero bias base resistance
IRB	Current at medium base resistance
RBM	Minimum base resistance at high current
RE	Emitter resistance
RC	Collector resistance

Capacitances

Name	Parameter Explanation
CJE	Base-emitter zero-bias depletion capacitance
VJE	Base-emitter built-in potential
MJE	Base-emitter junction exponential factor
CJC	Base-collector zero-bias depletion capacitance
VJC	Base-collector built-in potential
MJC	Base-collector junction exponential factor
CJS	Collector-substrate zero-bias depletion capacitance
VJS	Substrate junction built-in potential
MJS	Substrate junction exponential factor
FC	Forward bias depletion capacitance coefficient
XCJC	Fraction of base-collector capacitor connected to internal base

Transit time

Name	Parameter Explanation
TF	Ideal forward transit time
XTF	Coefficient for bias dependence of TF
VTF	Voltage describing V_{bc} dependence of TF
ITF	High current parameter for effect on TF
PTF	Excess phase at frequency of $1/(TF \cdot 2\pi)$
TR	Ideal reverse transit time

Noise and temperature effects

Name	Parameter Explanation
KF	Flicker noise coefficient
AF	Flicker noise exponential
TEMP	Device temperature for simulation
TNOM	Device parameter extraction temperature

Table A.1 is a list of the GP model parameters. The important equations of the GP model are expressed as follows. All these equations assume the following conditions.

1. All voltages in these model equations are referred to the internal nodes (inside the parasitic resistances) unless otherwise stated.
2. A current with a positive polarity flows into the bipolar transistor.

3. The model parameters are referred to *TNOM* and *TNOM* is the measurement temperature .
4. *TEMP* is the simulation temperature and its default value is *TNOM* when it is not specified . The parameters obtained at the temperature of *TEMP* are listed by adding primes to the corresponding parameters obtained at the temperature of *TNOM*.
5. Thermal voltage V_t is equal to $\frac{k \cdot TEMP}{q}$.

DC Operation

Normalized base charge q_b is expressed as :

$$q_b = \frac{1}{1 - \frac{V_{BC}}{VAF} - \frac{V_{BE}}{VAR}} \cdot \frac{1 + \sqrt{1 + \frac{4 \cdot IS}{IKF} \cdot [\exp(\frac{V_{BE}}{NF \cdot V_t}) - 1] + \frac{4 \cdot IS}{IKR} \cdot [\exp(\frac{V_{BC}}{NR \cdot V_t}) - 1]}}{2}$$

(A.1)

Collector current I_C is expressed as :

$$I_C = \frac{IS}{q_b} \cdot \left[\exp(\frac{V_{BE}}{NF \cdot V_t}) - \exp(\frac{V_{BC}}{NR \cdot V_t}) \right] - \frac{IS}{BR} \left[\exp(\frac{V_{BC}}{NR \cdot V_t}) - 1 \right] - ISC \cdot \left[\exp(\frac{V_{BC}}{NC \cdot V_t}) - 1 \right]$$

(A.2)

Emitter current I_E is expressed as:

$$I_E = \frac{-IS}{q_b} \cdot \left[\exp(\frac{V_{BE}}{NF \cdot V_t}) - \exp(\frac{V_{BC}}{NR \cdot V_t}) \right] - \frac{IS}{BF} \left[\exp(\frac{V_{BE}}{NF \cdot V_t}) - 1 \right] - ISE \cdot \left[\exp(\frac{V_{BE}}{NE \cdot V_t}) - 1 \right]$$

(A.3)

Base current I_B is expressed as:

$$I_B = \frac{IS}{BF}\cdot\left[\exp(\frac{V_{BE}}{NF\cdot V_t})-1\right]+ISE\cdot\left[\exp(\frac{V_{BE}}{NE\cdot V_t})-1\right]+\frac{IS}{BR}\cdot\left[\exp(\frac{V_{BC}}{NR\cdot V_t})-1\right]$$

$$+ISC\cdot\left[\exp(\frac{V_{BC}}{NC\cdot V_t})-1\right] \qquad \text{(A.4)}$$

DC and AC Operation

Base resistance R_B is expressed as:

For $IRB = 0$: $R_B = RBM + \frac{RB - RBM}{q_b}$. (A.5)

For $IRB \neq 0$:

$$z = \left(\sqrt{1+\frac{144\cdot I_B}{\pi^2\cdot IRB}}-1\right)\cdot\left(\frac{\pi^2}{24}\cdot\sqrt{\frac{IRB}{I_B}}\right), \qquad \text{(A.6)}$$

and $$R_B = RBM + 3\cdot(RB - RBM)\cdot\frac{\tan(z)-z}{z\cdot\tan^2(z)} \ . \qquad \text{(A.7)}$$

AC Operation

Effective forward transit time T_f is expressed as:

$$T_f = TF\cdot\left\{1+XTF\cdot\left[\frac{IS\cdot\left[\exp(\frac{V_{BE}}{NF\cdot V_t})-1\right]}{ITF+IS\cdot\left[\exp(\frac{V_{BE}}{NF\cdot V_t})-1\right]}\right]^2\cdot\exp(\frac{V_{BC}}{1.44\cdot VTF})\right\} \ . \qquad \text{(A.8)}$$

Forward transit charge Q_{tf} is expressed as:

$$Q_{tf} = \frac{T_f\cdot IS\cdot\left[\exp(\frac{V_{BE}}{NF\cdot V_t})-1\right]}{q_b} \ . \qquad \text{(A.9)}$$

Reverse transit charge Q_{tr} is expressed as:

$$Q_{tr} = \frac{TR \cdot IS \cdot \left[\exp(\frac{V_{BC}}{NR \cdot V_t}) - 1 \right]}{q_b} \quad . \tag{A.10}$$

Base-emitter junction capacitance C_{be} is expressed as:

For $V_{BE} < FC \cdot VJE$:

$$C_{be} = \frac{CJE}{\left(1 - \frac{V_{BE}}{VJE}\right)^{MJE}} \quad , \tag{A.11}$$

For $V_{BE} \geq FC \cdot VJE$:

$$C_{be} = \frac{CJE}{(1 - FC)^{MJE}} \cdot \left[1 + \frac{MJE \cdot (V_{BE} - FC \cdot VJE)}{VJE \cdot (1 - FC)} \right] . \tag{A.12}$$

Base-emitter diffusion capacitance $C_{diff\,(be)}$ is expressed as:

$$C_{diff\,(be)} = \frac{\partial Q_{tf}}{\partial V_{BE}} . \tag{A.13}$$

Total base-emitter capacitance C_{π} is expressed as:

$$C_{\pi} = C_{diff\,(be)} + C_{be} . \tag{A.14}$$

Base-collector internal and external junction capacitances C_{bc} and C_{bcx} are expressed as:

For $V_{BC} < FC \cdot VJC$:

$$C_{bc} = \frac{CJC \cdot XCJC}{\left(1 - \frac{V_{BC}}{VJC}\right)^{MJC}} \quad \text{and} \quad C_{bcx} = \frac{CJC \cdot (1 - XCJC)}{\left(1 - \frac{V_{BC}}{VJC}\right)^{MJC}}, \tag{A.15}$$

For $V_{BC} \geq FC \cdot VJC$:

$$C_{bc} = \frac{CJC \cdot XCJC}{(1 - FC)^{MJC}} \cdot \left[1 + \frac{MJC \cdot (V_{BC} - FC \cdot VJC)}{VJC \cdot (1 - FC)}\right],$$

and $$C_{bcx} = \frac{CJC \cdot (1 - XCJC)}{(1 - FC)^{MJC}} \cdot \left[1 + \frac{MJC \cdot (V_{BXC} - FC \cdot VJC)}{VJC \cdot (1 - FC)}\right], \tag{A.16}$$

where $V_{BXC} = V_B(external) - V_C$.

Base-collector internal diffusion capacitance $C_{diff\,(bc)}$ is expressed as:

$$C_{diff\,(bc)} = \frac{\partial Q_{tr}}{\partial V_{BC}} \ . \tag{A.17}$$

Total base-collector internal capacitance C_{μ} is expressed as:

$$C_{\mu} = C_{diff\,(bc)} + C_{bc}\,. \tag{A.18}$$

Collector-substrate capacitance C_{cs} is expressed as:

For $V_{SC} < 0$:

$$C_{cs} = \frac{CJS}{\left(1 - \frac{V_{SC}}{VJS}\right)^{MJS}} \ , \tag{A.19}$$

For $V_{SC} \geq 0$:

$$C_{cs} = CJS \cdot (1 + MJS \cdot \frac{V_{SC}}{VJS})\,. \tag{A.20}$$

Temperature Effects

Energy gap E_g is expressed as:

$$E_g = 1.16 - \left(\frac{7.02 \times 10^{-4} \cdot TEMP^2}{TEMP + 1108} \right) . \quad \text{(A.21)}$$

Intrinsic silicon concentration N_i is expressed as:

$$N_i = 1.45 \times 10^{10} \cdot \left(\frac{TEMP}{300.15} \right)^{1.5} \cdot \exp\left[\frac{q}{2k} \cdot \left(\frac{-E_g}{TEMP} + \frac{1.1151}{300.15} \right) \right] . \quad \text{(A.22)}$$

Saturation current IS is expressed as:

$$IS' = IS \left(\frac{TEMP}{TNOM} \right)^{XTI} \cdot \exp\left[\frac{E_g}{V_t} \cdot \left(\frac{TEMP}{TNOM} - 1 \right) \right] . \quad \text{(A.23)}$$

Forward ideal current gain BF is expressed as:

$$BF' = BF \cdot \left(\frac{TEMP}{TNOM} \right)^{XTB} . \quad \text{(A.24)}$$

Reverse ideal current gain BR is expressed as:

$$BR' = BR \cdot \left(\frac{TEMP}{TNOM} \right)^{XTB} . \quad \text{(A.25)}$$

Base-emitter leakage saturation current ISE is expressed as:

$$ISE' = ISE . \left(\frac{TEMP}{TNOM} \right)^{-XTB} \cdot \left\{ \left(\frac{TEMP}{TNOM} \right)^{XTI} \cdot \exp\left[\frac{E_g}{V_t} \left(\frac{TEMP}{TNOM} - 1 \right) \right] \right\}^{\frac{1}{NE}} . \quad \text{(A.26)}$$

Base-collector leakage saturation current ISC is expressed as:

$$ISC' = ISC . \left(\frac{TEMP}{TNOM} \right)^{-XTB} \cdot \left\{ \left(\frac{TEMP}{TNOM} \right)^{XTI} \cdot \exp\left[\frac{E_g}{V_t} \left(\frac{TEMP}{TNOM} - 1 \right) \right] \right\}^{\frac{1}{NC}} . \quad \text{(A.27)}$$

Base-emitter built-in potential VJE is expressed as:

$$VJE' = VJE \cdot \left(\frac{TEMP}{TNOM} \right) + 2 \cdot V_t \cdot \ln\left(\frac{1.45 \times 10^{10}}{N_i} \right) . \quad \text{(A.28)}$$

Base-collector built-in potential VJC is expressed as:

$$VJC' = VJC \cdot \left(\frac{TEMP}{TNOM} \right) + 2 \cdot V_t \cdot \ln \left(\frac{1.45 \times 10^{10}}{N_i} \right) . \quad \text{(A.29)}$$

APPENDIX B

The Major Equations Used in the VBIC Model

Table B.1 A list of the VBIC model parameters

Parasitic capacitors

Name	Parameter Explanation
CBEO	Base-emitter junction overlap capacitor
CBCO	Base- collector junction overlap capacitor

Space charge capacitors

Name	Parameter Explanation
CJE	Base-emitter zero-bias depletion capacitance
PE	Base-emitter built-in potential
ME	Base-emitter junction exponential factor
AJE	Switching parameter for base-emitter depletion capacitance
CJC	Base-collector zero-bias depletion capacitance
PC	Base-collector built-in potential
MC	Base-collector junction exponential factor
AJC	Switching parameter for base-collector depletion capacitance
CJEP	Base-emitter junction zero-bias depletion capacitance for the parasitic transistor
CJCP	Base-collector junction zero-bias depletion capacitance for the parasitic transistor
PS	Substrate junction built-in potential
MS	Substrate junction exponential factor
AJS	Switching parameter for substrate junction depletion capacitance
FC	Forward - bias depletion capacitance coefficient

Early effect modeling

Name	Parameter Explanation
VEF	Forward Early voltage
VER	Reverse Early voltage

DC forward

Name	Parameter Explanation
IS	Transport saturation current
NF	Forward current emission coefficient
IBEI	The ideal factor for base-emitter junction saturation current
NEI	The ideal factor for base-emitter junction emission coefficient
IBEN	The non- ideal factor for base-emitter junction saturation current
NEN	The non-ideal factor for base-emitter junction emission coefficient
IKF	High current when forward beta roll-off

DC reverse

Name	Parameter Explanation
NR	Reverse current emission coefficient
IBCI	The ideal factor for base-collector junction saturation current
NCI	The ideal factor for base-collector junction emission coefficient
IBCN	The non- ideal factor for base-collector junction saturation current
NCN	The non-ideal factor for base-collector junction emission coefficient
IKR	High current when reverse beta roll-off

Distributed base

Name	Parameter Explanation
WBE	Base distribution factor

Quasi-saturation effect

Name	Parameter Explanation
RCI	A parameter in the quasi-saturation model
GAMM	A parameter in the quasi-saturation model
VO	A parameter in the quasi-saturation model
HRCF	A parameter in the quasi-saturation model
QCO	The store charge parameter in the quasi-saturation model

Resistors

Name	Parameter Explanation
RE	Emitter resistance
RBX	Extrinsic base resistance
RBI	Intrinsic base resistance modulated by the normalized base charge
RS	Substrate resistance
RBP	Base resistance in the parasitic transistor
RCX	Extrinsic collector resistance

Avalanche effects

Name	Parameter Explanation
*AVC*1	A parameter for the weak avalanche current
*AVC*2	A parameter for the weak avalanche current

Delay time

Name	Parameter Explanation
TF	Ideal forward transit time
QTF	A parameter for the forward transit time
XTF	Coefficient for bias dependence of *TF*
ITF	Parameter for High current effect on *TF*
VTF	Voltage describing V_{bc} dependence of *TF*
TR	Ideal reverse transit time

Excess phase

Name	Parameter Explanation
TD	A parameter reflecting the excess phase shift

Parasitic transistor

Name	Parameter Explanation
ISP	Transport saturation current in the parasitic transistor
NFP	Forward current emission coefficient in the parasitic transistor
IBEIP	The ideal factor for base-emitter junction saturation current in the parasitic transistor
IBENP	The non- ideal factor for base-emitter junction saturation current in the parasitic transistor
IBCIP	The ideal factor for base-collector junction saturation current in the parasitic transistor
NCIP	The ideal factor for base-collector junction emission coefficient in the parasitic transistor
IBCNP	The non- ideal factor for base-collector junction saturation current in the parasitic transistor
NCNP	The non-ideal factor for base-collector junction emission coefficient in the parasitic transistor
IKP	High current when forward beta roll-off in the parasitic transistor

Table B.1 is a list of the VBIC model parameters .The major equations in the VBIC model are selected and listed here for the convenience of discussions and explanations.

In the following discussions, currents will be indexed with their corresponding node names and flow into the nodes. Meanwhile, branch voltages are denoted by abbreviations like "i" for internal, "x" for external, "o" for outer and "p" for parasitic: $V_{bei} = V_{Bi} - V_{Ei}$, $V_{bci} = V_{Bi} - V_{Ci}$, $V_{bcx} = V_{Bi} - V_{Cx}$, $V_{bep} = V_{Bx} - V_{Bp}$, $V_{bcp} = V_{Si} - V_{Bp}$, $V_{BE} = V_B - V_E$, $V_{CE} = V_C - V_E$, $V_{BC} = V_B - V_C$, $V_{SC} = V_S - V_C$.

DC performance of the intrinsic transistor

The collector current I_{cc} is expressed as

$$I_{cc} = \frac{I_{tf} - I_{tr}}{q_b} = \frac{IS}{q_b} \cdot \left(e^{\frac{V_{bei}}{NF \cdot V_t}} - 1 \right) - \frac{IS}{q_b} \left(e^{\frac{V_{bci}}{NR \cdot V_t}} - 1 \right), \tag{B.1}$$

$$q_b = \frac{q_1}{2} + \sqrt{\left(\frac{q_1}{2} \right)^2 + q_2} \quad , \tag{B.2}$$

$$q_1 = 1 + \frac{q_{je}}{VER} + \frac{q_{jc}}{VEF} , \tag{B.3}$$

and $$q_2 = \frac{1}{IKF} \cdot IS \cdot \left(e^{\frac{V_{bei}}{NF \cdot V_t}} - 1 \right) + \frac{1}{IKR} \cdot IS \cdot \left(e^{\frac{V_{bci}}{NR \cdot V_t}} - 1 \right) . \tag{B.4}$$

When $V_i < FC \cdot P_i$, the normalized depletion charge function is defined as :

$$q_{ji} = \frac{P_i}{(1 - M_i)} \left[1 - \left(1 - \frac{V_i}{P_i} \right)^{1 - M_i} \right] \quad , \qquad i = e, c . \tag{B.5}$$

When $V_i > FC \cdot P_i$, the normalized depletion charge function is defined as :

$$q_{ji} = \frac{P_i}{(1-M_i)}\left[1-(1-FC)^{1-M_i}\right] + (V_i - FC\cdot P_i)\cdot\left[\frac{1-FC+\frac{M_i(V_i-FC\cdot P_i)}{2P_i}}{(1-FC)^{(1+M_i)}}\right],$$

$$i = e, c\,. \qquad \text{(B.6)}$$

The total base current of the intrinsic transistor is

$$I_b = I_{be} + I_{bc}\ . \qquad \text{(B.7)}$$

The total base-emitter current I_{be} is split into inner base and outer base part and is expressed as

$$\begin{aligned} I_{be} &= I_{beinner} + I_{bex} \\ &= IBEI\cdot\left(e^{\frac{V_{bei}}{NEI\cdot V_t}} - 1\right) + IBEN\cdot\left(e^{\frac{V_{bei}}{NEN\cdot V_t}} - 1\right). \end{aligned} \qquad \text{(B.8)}$$

The base-emitter inner current $I_{beinner}$ is expressed as

$$I_{beinner} = I_{bei} + I_{ben}\ . \qquad \text{(B.9)}$$

The ideal part of base-emitter inner current I_{bei} is expressed as

$$I_{bei} = WBE\cdot IBEI\cdot\left(e^{\frac{V_{bei}}{NEI\cdot V_t}} - 1\right). \qquad \text{(B.10)}$$

The non-ideal part of base-emitter inner current I_{ben} is expressed as

$$I_{ben} = WBE\cdot IBEN\cdot\left(e^{\frac{V_{bei}}{NEN\cdot V_t}} - 1\right). \qquad \text{(B.11)}$$

The base-emitter outer current I_{bex} is expressed as:

$$I_{bex} = I_{bexi} + I_{bexn}\,. \qquad \text{(B.12)}$$

The ideal part of base-emitter outer current I_{bexi} is expressed as

$$I_{bexi} = (1 - WBE) \cdot IBEI \cdot \left(e^{\frac{V_{bei}}{NEI \cdot V_t}} - 1 \right) \quad . \tag{B.13}$$

The non-ideal part of base-emitter outer current I_{bexn} is expressed as

$$I_{bexn} = (1 - WBE) \cdot IBEN \cdot \left(e^{\frac{V_{bei}}{NEN \cdot V_t}} - 1 \right) \quad . \tag{B.14}$$

The total base-collector current I_{bc} is split into ideal and nonideal parts and is expressed as

$$I_{bc} = I_{bci} + I_{bcn} \quad . \tag{B.15}$$

The ideal part of base-collector current I_{bci} is expressed as

$$I_{bci} = IBCI \cdot \left(e^{\frac{V_{bci}}{NCI \cdot V_t}} - 1 \right) \quad . \tag{B.16}$$

The non-ideal part of base-collector current I_{bcn} is expressed as

$$I_{bcn} = IBCN \cdot \left(e^{\frac{V_{bci}}{NCN \cdot V_t}} - 1 \right) \quad . \tag{B.17}$$

Avalanche current I_{gc} is expressed as

$$I_{gc} = (I_{cc} - I_{bc}) \cdot AVC1 \cdot (PC - V_{bci}) \cdot e^{-AVC2 \cdot (PC - V_{bci})^{MC-1}} \quad . \tag{B.18}$$

DC performance of the parasitic transistor

The total parasitic collector current I_{ccp} is expressed as

$$I_{ccp} = \frac{I_{tfp} - I_{trp}}{q_{bp}} \quad . \tag{B.19}$$

The parasitic forward current I_{tfp} is expressed as

$$I_{tfp} = ISP \cdot [WSP \cdot e^{\frac{V_{bep}}{NFP \cdot V_t}} + (1 - WSP) \cdot e^{\frac{V_{bci}}{NFP \cdot V_t}} - 1] \quad . \tag{B.20}$$

The parasitic reverse current I_{trp} is expressed as

$$I_{trp} = ISP \cdot \left(e^{\frac{V_{bcp}}{NFP \cdot V_t}} - 1 \right) . \tag{B.21}$$

$$q_{bp} = \frac{1}{2} \cdot \sqrt{1 + 4 \cdot q_{2p}} , \tag{B.22}$$

and

$$q_{2p} = \frac{I_{tfp}}{IKP} . \tag{B.23}$$

The total parasitic base current I_{bp} is split into base-emitter current and base-collector current and is expressed as

$$I_{bp} = I_{bep} + I_{bcp} . \tag{B.24}$$

The parasitic base-emitter current I_{bep} is split into ideal part and non-ideal part and is expressed as

$$I_{bep} = I_{beip} + I_{benp} . \tag{B.25}$$

The ideal part of parasitic base-emitter current I_{beip} is expressed as

$$I_{beip} = IBEIP \cdot \left(e^{\frac{V_{bep}}{NCI \cdot V_t}} - 1 \right) . \tag{B.26}$$

The non-ideal part of parasitic base-emitter current I_{benp} is expressed as

$$I_{benp} = IBENP \cdot \left(e^{\frac{V_{bep}}{NCN \cdot V_t}} - 1 \right) . \tag{B.27}$$

The parasitic base-collector current I_{bcp} is split into ideal part and non-ideal part and is expressed as

$$I_{bcp} = I_{bcip} + I_{bcnp} \ . \tag{B.28}$$

The ideal part of parasitic base-collector current I_{bcip} is expressed as

$$I_{bcip} = IBCIP \cdot \left(e^{\frac{V_{bcp}}{NCIP \cdot V_t}} - 1 \right) . \tag{B.29}$$

The non-ideal part of parasitic base-collector current I_{bcnp} is expressed as

$$I_{bcnp} = IBCNP \cdot \left(e^{\frac{V_{bcp}}{NCNP \cdot V_t}} - 1 \right) . \tag{B.30}$$

Resistors

Emitter resistance R_e is considered as constant. Parasitic resistance R_s is modeled with constant value. Total base resistance R_b is expressed as

$$R_b = R_{bx} + \frac{R_{bi}}{q_b} \ , \tag{B.31}$$

where the outer part of base resistance R_{bx} is considered as constant and the parasitic base resistance R_{bp} is expressed as

$$R_{bp} = \frac{R_{bip}}{q_{bp}} \ . \tag{B.32}$$

Besides, the outer part of collector resistance R_{cx} is considered as constant. R_{ci} is used for the model of "quasi-saturation", that is

$$I_{R_{ci}} = \frac{I_{epi0}}{\sqrt{1 + \left[\frac{I_{epi0} \cdot R_{ci}}{VO \cdot \left(1 + \frac{0.5 \cdot \sqrt{0.01 + V_{rci}^2}}{VO \cdot HRCF} \right)} \right]^2}} \ , \tag{B.33}$$

$$I_{epi0} = \frac{1}{R_{ci}}\left[V_{rci} + V_t \cdot \left(K_{bci} - K_{bcx} - \ln\frac{1+K_{bci}}{1+K_{bcx}}\right)\right] \quad , \tag{B.34}$$

$$K_{bci} = \sqrt{1 + GAMM \cdot e^{\frac{V_{bci}}{V_t}}} \quad , \tag{B.35}$$

$$K_{bcx} = \sqrt{1 + GAMM \cdot e^{\frac{V_{bcx}}{V_t}}} \quad , \tag{B.36}$$

$$V_{rci} = V_{bci} - V_{bcx} = V_{bi} - V_{ci} - (V_{bi} - V_{cx}) = V_{cx} - V_{ci} \quad . \tag{B.37}$$

Capacitors

The total base-emitter space charge capacitance C_{jbe} is expressed as

$$C_{jbe} = \frac{\partial(CJE \cdot q_{je})}{\partial(V_{BE})} \quad . \tag{B.38}$$

The inner and outer parts of base-emitter space charge capacitance C_{jbei} and C_{jbex} are expressed as

$$C_{jbei} = WBE \cdot C_{jbe} \quad \text{and} \quad C_{jbex} = (1 - WBE) \cdot C_{jbe} \quad . \tag{B.39}$$

The base-emitter diffusion capacitance C_{be} is expressed as

$$C_{be} = \frac{\partial(T_f \cdot I_{tf})}{\partial(V_{BE})}, \tag{B.40}$$

where

$$T_f = TF \cdot (1 + QTF \cdot q_1) \cdot \left[1 + XTF \cdot \left(\frac{I_{tf}}{I_{tf} + ITF}\right)^2 \cdot e^{\frac{V_{bci}}{1.44 \cdot VTF}}\right]. \tag{B.41}$$

The total base-collector space charge capacitance C_{jbc} is expressed as

$$C_{jbc} = \frac{\partial(CJC \cdot q_{jc})}{\partial(V_{BC})}. \tag{B.42}$$

The inner and outer parts of base-collector space charge capacitance C_{jbci} and C_{jbcx} are expressed as

$$C_{jbci} = WSP \cdot C_{jbc} \quad \text{and} \quad C_{jbcx} = (1 - WSP) \cdot C_{jbc} \ . \tag{B.43}$$

The base-collector diffusion capacitance C_{bc} is expressed as

$$C_{bc} = \frac{\partial (TR \cdot I_{tr})}{\partial (V_{BC})} \ . \tag{B.44}$$

The base-collector space charge capacitance of the parasitic transistor C_{cs} is expressed as

For $V_{SC} < 0$:

$$C_{cs} = \frac{CJCP}{\left(1 - \frac{V_{SC}}{PS}\right)^{MS}} \ , \tag{B.45}$$

and

For $V_{SC} \geq 0$:

$$C_{cs} = CJCP \cdot (1 + MS \cdot \frac{V_{SC}}{PS}) \, . \tag{B.46}$$

The parasitic diffusion capacitance C_{bep} is expressed as

$$C_{bep} = \frac{\partial (TR \cdot I_{tfp})}{\partial (V_{BC})} \tag{B.47}$$

The additional charge caused by quasi-saturation Q_{bcx} is expressed as

$$Q_{bcx} = QCO \cdot K_{bcx} \ . \tag{B.48}$$

The other additional charge caused by quasi-saturation Q_{bcq} is expressed as

$$Q_{bcq} = QCO \cdot K_{bci} \, . \tag{B.49}$$

APPENDIX C

Comparison between Measured Data and Simulated Results

Table C.1 The comparison between measured data and simulated results in Chapter 2

	Real(S11)	Real(S11)	Imag(S11)	Imag(S11)	Real(S21)	Real(S21)	Imag(S21)	Imag(S21)
Freq (Hz)	measured	simulated	measured	simulated	measured	simulated	measured	simulated
2.00E+08	5.89E-01	5.83E-01	-3.30E-02	-3.27E-02	-7.78E+00	-7.86E+00	2.73E-01	2.75E-01
4.00E+08	5.86E-01	5.80E-01	-6.60E-02	-6.55E-02	-7.75E+00	-7.83E+00	5.44E-01	5.49E-01
6.00E+08	5.80E-01	5.74E-01	-9.80E-02	-9.72E-02	-7.71E+00	-7.79E+00	8.11E-01	8.18E-01
8.00E+08	5.73E-01	5.67E-01	-1.29E-01	-1.28E-01	-7.65E+00	-7.73E+00	1.07E+00	1.08E+00
1.00E+09	5.63E-01	5.57E-01	-1.60E-01	-1.59E-01	-7.57E+00	-7.65E+00	1.33E+00	1.34E+00
1.20E+09	5.52E-01	5.46E-01	-1.90E-01	-1.88E-01	-7.48E+00	-7.55E+00	1.58E+00	1.59E+00
1.40E+09	5.39E-01	5.34E-01	-2.19E-01	-2.17E-01	-7.38E+00	-7.45E+00	1.82E+00	1.84E+00
1.60E+09	5.24E-01	5.19E-01	-2.46E-01	-2.44E-01	-7.26E+00	-7.33E+00	2.05E+00	2.07E+00
1.80E+09	5.08E-01	5.09E-01	-2.72E-01	-2.70E-01	-7.13E+00	-7.20E+00	2.27E+00	2.29E+00
2.00E+09	4.90E-01	4.91E-01	-2.97E-01	-2.95E-01	-6.99E+00	-7.06E+00	2.47E+00	2.49E+00
2.20E+09	4.72E-01	4.73E-01	-3.20E-01	-3.17E-01	-6.84E+00	-6.91E+00	2.67E+00	2.69E+00
2.40E+09	4.52E-01	4.53E-01	-3.42E-01	-3.39E-01	-6.68E+00	-6.75E+00	2.85E+00	2.87E+00
2.60E+09	4.32E-01	4.33E-01	-3.61E-01	-3.58E-01	-6.52E+00	-6.59E+00	3.02E+00	3.05E+00
2.80E+09	4.11E-01	4.12E-01	-3.80E-01	-3.77E-01	-6.35E+00	-6.41E+00	3.17E+00	3.20E+00
3.00E+09	3.89E-01	3.90E-01	-3.97E-01	-3.94E-01	-6.18E+00	-6.24E+00	3.32E+00	3.35E+00
3.20E+09	3.68E-01	3.69E-01	-4.12E-01	-4.09E-01	-6.00E+00	-6.06E+00	3.45E+00	3.41E+00
3.40E+09	3.46E-01	3.47E-01	-4.25E-01	-4.22E-01	-5.83E+00	-5.87E+00	3.57E+00	3.53E+00
3.60E+09	3.23E-01	3.21E-01	-4.37E-01	-4.34E-01	-5.65E+00	-5.69E+00	3.67E+00	3.63E+00
3.80E+09	3.01E-01	2.99E-01	-4.48E-01	-4.44E-01	-5.47E+00	-5.51E+00	3.77E+00	3.72E+00
4.00E+09	2.79E-01	2.77E-01	-4.58E-01	-4.54E-01	-5.29E+00	-5.33E+00	3.85E+00	3.80E+00
4.20E+09	2.57E-01	2.55E-01	-4.66E-01	-4.62E-01	-5.12E+00	-5.16E+00	3.93E+00	3.88E+00
4.40E+09	2.36E-01	2.35E-01	-4.72E-01	-4.68E-01	-4.95E+00	-4.99E+00	3.99E+00	3.94E+00
4.60E+09	2.15E-01	2.14E-01	-4.78E-01	-4.74E-01	-4.78E+00	-4.82E+00	4.05E+00	4.00E+00
4.80E+09	1.94E-01	1.93E-01	-4.83E-01	-4.88E-01	-4.61E+00	-4.65E+00	4.09E+00	4.04E+00
5.00E+09	1.73E-01	1.72E-01	-4.86E-01	-4.91E-01	-4.44E+00	-4.47E+00	4.13E+00	4.08E+00
5.20E+09	1.53E-01	1.52E-01	-4.89E-01	-4.94E-01	-4.28E+00	-4.31E+00	4.16E+00	4.11E+00
5.40E+09	1.34E-01	1.33E-01	-4.91E-01	-4.96E-01	-4.13E+00	-4.16E+00	4.18E+00	4.13E+00
5.60E+09	1.15E-01	1.14E-01	-4.92E-01	-4.97E-01	-3.98E+00	-4.01E+00	4.20E+00	4.15E+00

	Real(S11)	Real(S11)	Imag(S11)	Imag(S11)	Real(S21)	Real(S21)	Imag(S21)	Imag(S21)
Freq (Hz)	measured	simulated	measured	simulated	measured	simulated	measured	simulated
5.80E+09	9.60E-02	9.54E-02	-4.92E-01	-4.97E-01	-3.83E+00	-3.86E+00	4.21E+00	4.16E+00
6.00E+09	7.90E-02	7.85E-02	-4.92E-01	-4.97E-01	-3.68E+00	-3.71E+00	4.22E+00	4.17E+00
6.20E+09	6.10E-02	6.06E-02	-4.91E-01	-4.96E-01	-3.54E+00	-3.57E+00	4.22E+00	4.17E+00
6.40E+09	4.40E-02	4.37E-02	-4.89E-01	-4.94E-01	-3.41E+00	-3.44E+00	4.22E+00	4.17E+00
6.60E+09	2.80E-02	2.78E-02	-4.87E-01	-4.92E-01	-3.28E+00	-3.30E+00	4.21E+00	4.16E+00
6.80E+09	1.30E-02	1.29E-02	-4.85E-01	-4.90E-01	-3.15E+00	-3.17E+00	4.20E+00	4.15E+00
7.00E+09	-2.62E-03	-2.64E-03	-4.82E-01	-4.87E-01	-3.03E+00	-3.05E+00	4.19E+00	4.16E+00
7.20E+09	-1.70E-02	-1.71E-02	-4.79E-01	-4.84E-01	-2.91E+00	-2.93E+00	4.17E+00	4.14E+00
7.40E+09	-3.10E-02	-3.12E-02	-4.75E-01	-4.80E-01	-2.80E+00	-2.82E+00	4.15E+00	4.13E+00
7.60E+09	-4.50E-02	-4.53E-02	-4.71E-01	-4.76E-01	-2.69E+00	-2.71E+00	4.13E+00	4.11E+00
7.80E+09	-5.80E-02	-5.84E-02	-4.67E-01	-4.73E-01	-2.59E+00	-2.61E+00	4.11E+00	4.09E+00
8.00E+09	-7.10E-02	-7.15E-02	-4.63E-01	-4.69E-01	-2.49E+00	-2.51E+00	4.08E+00	4.06E+00
8.20E+09	-8.30E-02	-8.36E-02	-4.58E-01	-4.64E-01	-2.39E+00	-2.41E+00	4.05E+00	4.03E+00
8.40E+09	-9.40E-02	-9.47E-02	-4.53E-01	-4.59E-01	-2.29E+00	-2.31E+00	4.03E+00	4.01E+00
8.60E+09	-1.06E-01	-1.07E-01	-4.49E-01	-4.55E-01	-2.20E+00	-2.22E+00	4.00E+00	3.98E+00
8.80E+09	-1.16E-01	-1.17E-01	-4.44E-01	-4.50E-01	-2.12E+00	-2.14E+00	3.96E+00	3.94E+00
9.00E+09	-1.27E-01	-1.28E-01	-4.38E-01	-4.44E-01	-2.03E+00	-2.02E+00	3.93E+00	3.91E+00
9.20E+09	-1.37E-01	-1.38E-01	-4.33E-01	-4.39E-01	-1.95E+00	-1.92E+00	3.90E+00	3.88E+00
9.40E+09	-1.46E-01	-1.47E-01	-4.28E-01	-4.34E-01	-1.87E+00	-1.85E+00	3.87E+00	3.85E+00
9.60E+09	-1.56E-01	-1.57E-01	-4.23E-01	-4.28E-01	-1.80E+00	-1.78E+00	3.83E+00	3.81E+00
9.80E+09	-1.65E-01	-1.66E-01	-4.17E-01	-4.22E-01	-1.73E+00	-1.71E+00	3.80E+00	3.78E+00
1.00E+10	-1.73E-01	-1.74E-01	-4.12E-01	-4.17E-01	-1.66E+00	-1.64E+00	3.76E+00	3.74E+00
1.02E+10	-1.81E-01	-1.82E-01	-4.06E-01	-4.11E-01	-1.59E+00	-1.57E+00	3.73E+00	3.71E+00
1.04E+10	-1.89E-01	-1.90E-01	-4.01E-01	-4.06E-01	-1.53E+00	-1.51E+00	3.70E+00	3.68E+00
1.06E+10	-1.97E-01	-1.98E-01	-3.95E-01	-4.00E-01	-1.46E+00	-1.44E+00	3.66E+00	3.64E+00
1.08E+10	-2.04E-01	-2.05E-01	-3.89E-01	-3.94E-01	-1.40E+00	-1.38E+00	3.63E+00	3.61E+00
1.10E+10	-2.12E-01	-2.13E-01	-3.84E-01	-3.89E-01	-1.35E+00	-1.33E+00	3.59E+00	3.57E+00
1.12E+10	-2.18E-01	-2.20E-01	-3.78E-01	-3.83E-01	-1.29E+00	-1.27E+00	3.56E+00	3.54E+00

	Real(S11)	Real(S11)	Imag(S11)	Imag(S11)	Real(S21)	Real(S21)	Imag(S21)	Imag(S21)
Freq (Hz)	measured	simulated	measured	simulated	measured	simulated	measured	simulated
1.14E+10	-2.25E-01	-2.27E-01	-3.73E-01	-3.78E-01	-1.24E+00	-1.22E+00	3.52E+00	3.50E+00
1.16E+10	-2.31E-01	-2.33E-01	-3.67E-01	-3.72E-01	-1.19E+00	-1.17E+00	3.49E+00	3.47E+00
1.18E+10	-2.37E-01	-2.39E-01	-3.62E-01	-3.67E-01	-1.14E+00	-1.13E+00	3.45E+00	3.43E+00
1.20E+10	-2.43E-01	-2.45E-01	-3.56E-01	-3.61E-01	-1.09E+00	-1.08E+00	3.42E+00	3.40E+00
1.22E+10	-2.49E-01	-2.51E-01	-3.51E-01	-3.47E-01	-1.04E+00	-1.03E+00	3.38E+00	3.36E+00
1.24E+10	-2.54E-01	-2.56E-01	-3.46E-01	-3.42E-01	-9.97E-01	-9.84E-01	3.35E+00	3.33E+00
1.26E+10	-2.60E-01	-2.62E-01	-3.40E-01	-3.36E-01	-9.55E-01	-9.43E-01	3.32E+00	3.35E+00
1.28E+10	-2.65E-01	-2.67E-01	-3.35E-01	-3.31E-01	-9.13E-01	-9.01E-01	3.28E+00	3.31E+00
1.30E+10	-2.70E-01	-2.72E-01	-3.30E-01	-3.26E-01	-8.73E-01	-8.62E-01	3.25E+00	3.28E+00
1.32E+10	-2.74E-01	-2.76E-01	-3.24E-01	-3.20E-01	-8.34E-01	-8.23E-01	3.22E+00	3.25E+00
1.34E+10	-2.79E-01	-2.81E-01	-3.19E-01	-3.15E-01	-7.97E-01	-7.87E-01	3.18E+00	3.21E+00
1.36E+10	-2.83E-01	-2.85E-01	-3.14E-01	-3.10E-01	-7.61E-01	-7.51E-01	3.15E+00	3.18E+00
1.38E+10	-2.87E-01	-2.89E-01	-3.09E-01	-3.05E-01	-7.26E-01	-7.32E-01	3.12E+00	3.15E+00
1.40E+10	-2.92E-01	-2.94E-01	-3.04E-01	-3.00E-01	-6.92E-01	-6.98E-01	3.09E+00	3.12E+00
1.42E+10	-2.95E-01	-2.97E-01	-2.99E-01	-2.95E-01	-6.60E-01	-6.66E-01	3.06E+00	3.09E+00
1.44E+10	-2.99E-01	-3.01E-01	-2.94E-01	-2.90E-01	-6.28E-01	-6.34E-01	3.03E+00	3.06E+00
1.46E+10	-3.03E-01	-3.05E-01	-2.89E-01	-2.86E-01	-5.98E-01	-6.03E-01	3.00E+00	3.03E+00
1.48E+10	-3.07E-01	-3.09E-01	-2.84E-01	-2.81E-01	-5.68E-01	-5.73E-01	2.97E+00	3.00E+00
1.50E+10	-3.10E-01	-3.12E-01	-2.79E-01	-2.76E-01	-5.40E-01	-5.45E-01	2.94E+00	2.97E+00
1.52E+10	-3.13E-01	-3.15E-01	-2.75E-01	-2.72E-01	-5.12E-01	-5.17E-01	2.91E+00	2.94E+00
1.54E+10	-3.17E-01	-3.19E-01	-2.70E-01	-2.67E-01	-4.85E-01	-4.89E-01	2.88E+00	2.91E+00
1.56E+10	-3.20E-01	-3.22E-01	-2.65E-01	-2.62E-01	-4.59E-01	-4.63E-01	2.85E+00	2.88E+00
1.58E+10	-3.23E-01	-3.25E-01	-2.61E-01	-2.58E-01	-4.34E-01	-4.38E-01	2.83E+00	2.86E+00
1.60E+10	-3.26E-01	-3.28E-01	-2.56E-01	-2.53E-01	-4.10E-01	-4.14E-01	2.80E+00	2.83E+00
1.62E+10	-3.28E-01	-3.30E-01	-2.51E-01	-2.48E-01	-3.86E-01	-3.89E-01	2.77E+00	2.80E+00
1.64E+10	-3.31E-01	-3.33E-01	-2.47E-01	-2.44E-01	-3.63E-01	-3.66E-01	2.74E+00	2.77E+00
1.66E+10	-3.34E-01	-3.33E-01	-2.42E-01	-2.41E-01	-3.41E-01	-3.44E-01	2.72E+00	2.70E+00
1.68E+10	-3.36E-01	-3.35E-01	-2.38E-01	-2.37E-01	-3.19E-01	-3.22E-01	2.69E+00	2.67E+00
1.70E+10	-3.39E-01	-3.38E-01	-2.34E-01	-2.33E-01	-2.99E-01	-3.02E-01	2.67E+00	2.65E+00
1.72E+10	-3.41E-01	-3.40E-01	-2.29E-01	-2.28E-01	-2.78E-01	-2.80E-01	2.64E+00	2.62E+00
1.74E+10	-3.43E-01	-3.42E-01	-2.25E-01	-2.24E-01	-2.58E-01	-2.60E-01	2.62E+00	2.60E+00
1.76E+10	-3.46E-01	-3.45E-01	-2.21E-01	-2.20E-01	-2.39E-01	-2.41E-01	2.59E+00	2.57E+00
1.78E+10	-3.48E-01	-3.47E-01	-2.17E-01	-2.16E-01	-2.21E-01	-2.23E-01	2.57E+00	2.55E+00
1.80E+10	-3.50E-01	-3.49E-01	-2.13E-01	-2.12E-01	-2.03E-01	-2.05E-01	2.54E+00	2.52E+00

	Real(S12)	Real(S12)	Imag(S12)	Imag(S12)	Real(S22)	Real(S22)	Imag(S22)	Imag(S22)
Freq (Hz)	measured	simulated	measured	simulated	measured	simulated	measured	simulated
2.00E+08	2.07E-04	2.09E-04	6.23E-03	6.17E-03	9.98E-01	9.82E-01	-5.00E-02	-5.08E-02
4.00E+08	8.26E-04	8.36E-04	1.20E-02	1.19E-02	9.93E-01	9.77E-01	-1.00E-01	-1.02E-01
6.00E+08	1.85E-03	1.87E-03	1.90E-02	1.88E-02	9.85E-01	9.70E-01	-1.48E-01	-1.50E-01
8.00E+08	3.26E-03	3.30E-03	2.50E-02	2.47E-02	9.74E-01	9.59E-01	-1.96E-01	-1.99E-01
1.00E+09	5.05E-03	5.11E-03	3.00E-02	2.96E-02	9.59E-01	9.44E-01	-2.43E-01	-2.47E-01
1.20E+09	7.19E-03	7.28E-03	3.60E-02	3.55E-02	9.42E-01	9.27E-01	-2.89E-01	-2.94E-01
1.40E+09	9.67E-03	9.79E-03	4.10E-02	4.04E-02	9.22E-01	9.08E-01	-3.32E-01	-3.37E-01
1.60E+09	1.20E-02	1.21E-02	4.70E-02	4.63E-02	9.00E-01	8.86E-01	-3.74E-01	-3.80E-01
1.80E+09	1.50E-02	1.52E-02	5.20E-02	5.13E-02	8.76E-01	8.62E-01	-4.14E-01	-4.21E-01
2.00E+09	1.90E-02	1.92E-02	5.60E-02	5.52E-02	8.49E-01	8.36E-01	-4.51E-01	-4.58E-01
2.20E+09	2.20E-02	2.23E-02	6.10E-02	6.01E-02	8.21E-01	8.08E-01	-4.86E-01	-4.94E-01
2.40E+09	2.60E-02	2.63E-02	6.50E-02	6.41E-02	7.92E-01	7.80E-01	-5.19E-01	-5.27E-01
2.60E+09	3.00E-02	3.04E-02	6.80E-02	6.70E-02	7.61E-01	7.49E-01	-5.49E-01	-5.58E-01
2.80E+09	3.40E-02	3.44E-02	7.20E-02	7.10E-02	7.29E-01	7.18E-01	-5.77E-01	-5.86E-01
3.00E+09	3.80E-02	3.85E-02	7.50E-02	7.40E-02	6.96E-01	6.85E-01	-6.03E-01	-6.13E-01
3.20E+09	4.20E-02	4.27E-02	7.80E-02	7.69E-02	6.63E-01	6.53E-01	-6.26E-01	-6.36E-01
3.40E+09	4.60E-02	4.68E-02	8.10E-02	7.99E-02	6.30E-01	6.20E-01	-6.47E-01	-6.57E-01
3.60E+09	5.00E-02	5.09E-02	8.30E-02	8.18E-02	5.97E-01	5.88E-01	-6.65E-01	-6.76E-01
3.80E+09	5.40E-02	5.49E-02	8.50E-02	8.38E-02	5.63E-01	5.54E-01	-6.81E-01	-6.92E-01
4.00E+09	5.90E-02	6.00E-02	8.70E-02	8.58E-02	5.30E-01	5.38E-01	-6.96E-01	-7.07E-01
4.20E+09	6.30E-02	6.41E-02	8.80E-02	8.68E-02	4.97E-01	5.04E-01	-7.08E-01	-7.19E-01
4.40E+09	6.70E-02	6.81E-02	9.00E-02	8.87E-02	4.64E-01	4.71E-01	-7.19E-01	-7.31E-01
4.60E+09	7.10E-02	7.22E-02	9.10E-02	8.97E-02	4.32E-01	4.38E-01	-7.28E-01	-7.40E-01
4.80E+09	7.50E-02	7.63E-02	9.20E-02	9.07E-02	4.00E-01	4.06E-01	-7.35E-01	-7.25E-01
5.00E+09	7.80E-02	7.93E-02	9.20E-02	9.07E-02	3.70E-01	3.76E-01	-7.40E-01	-7.30E-01
5.20E+09	8.20E-02	8.34E-02	9.30E-02	9.17E-02	3.39E-01	3.44E-01	-7.45E-01	-7.35E-01
5.40E+09	8.60E-02	8.75E-02	9.30E-02	9.17E-02	3.10E-01	3.15E-01	-7.48E-01	-7.38E-01
5.60E+09	8.90E-02	9.05E-02	9.30E-02	9.17E-02	2.81E-01	2.85E-01	-7.49E-01	-7.39E-01

	Real(S12)	Real(S12)	Imag(S12)	Imag(S12)	Real(S22)	Real(S22)	Imag(S22)	Imag(S22)
Freq (Hz)	measured	simulated	measured	simulated	measured	simulated	measured	simulated
5.80E+09	9.30E-02	9.46E-02	9.30E-02	9.45E-02	2.53E-01	2.57E-01	-7.50E-01	-7.40E-01
6.00E+09	9.60E-02	9.76E-02	9.30E-02	9.45E-02	2.26E-01	2.29E-01	-7.50E-01	-7.40E-01
6.20E+09	9.90E-02	9.70E-02	9.30E-02	9.45E-02	2.00E-01	2.03E-01	-7.48E-01	-7.38E-01
6.40E+09	1.03E-01	1.01E-01	9.30E-02	9.45E-02	1.75E-01	1.78E-01	-7.46E-01	-7.36E-01
6.60E+09	1.06E-01	1.04E-01	9.30E-02	9.45E-02	1.50E-01	1.52E-01	-7.43E-01	-7.33E-01
6.80E+09	1.08E-01	1.06E-01	9.20E-02	9.35E-02	1.27E-01	1.29E-01	-7.40E-01	-7.30E-01
7.00E+09	1.11E-01	1.09E-01	9.20E-02	9.35E-02	1.04E-01	1.06E-01	-7.36E-01	-7.26E-01
7.20E+09	1.14E-01	1.12E-01	9.10E-02	9.25E-02	8.20E-02	8.32E-02	-7.31E-01	-7.21E-01
7.40E+09	1.17E-01	1.15E-01	9.00E-02	9.14E-02	6.00E-02	6.09E-02	-7.26E-01	-7.17E-01
7.60E+09	1.19E-01	1.17E-01	9.00E-02	9.14E-02	4.00E-02	4.06E-02	-7.20E-01	-7.11E-01
7.80E+09	1.22E-01	1.20E-01	8.90E-02	9.04E-02	2.00E-02	2.03E-02	-7.14E-01	-7.05E-01
8.00E+09	1.24E-01	1.22E-01	8.80E-02	8.94E-02	1.09E-03	1.11E-03	-7.08E-01	-6.99E-01
8.20E+09	1.26E-01	1.23E-01	8.70E-02	8.84E-02	-1.70E-02	-1.73E-02	-7.01E-01	-6.92E-01
8.40E+09	1.28E-01	1.25E-01	8.70E-02	8.84E-02	-3.50E-02	-3.55E-02	-6.94E-01	-6.85E-01
8.60E+09	1.30E-01	1.27E-01	8.60E-02	8.74E-02	-5.20E-02	-5.28E-02	-6.87E-01	-6.78E-01
8.80E+09	1.32E-01	1.29E-01	8.50E-02	8.64E-02	-6.80E-02	-6.90E-02	-6.79E-01	-6.70E-01
9.00E+09	1.34E-01	1.31E-01	8.40E-02	8.53E-02	-8.40E-02	-8.53E-02	-6.72E-01	-6.63E-01
9.20E+09	1.36E-01	1.33E-01	8.30E-02	8.43E-02	-9.90E-02	-1.01E-01	-6.64E-01	-6.55E-01
9.40E+09	1.38E-01	1.35E-01	8.20E-02	8.33E-02	-1.14E-01	-1.16E-01	-6.56E-01	-6.47E-01
9.60E+09	1.40E-01	1.37E-01	8.10E-02	8.23E-02	-1.28E-01	-1.31E-01	-6.48E-01	-6.40E-01
9.80E+09	1.41E-01	1.38E-01	8.00E-02	8.13E-02	-1.41E-01	-1.44E-01	-6.40E-01	-6.32E-01
1.00E+10	1.43E-01	1.40E-01	7.90E-02	8.03E-02	-1.54E-01	-1.57E-01	-6.32E-01	-6.24E-01
1.02E+10	1.44E-01	1.41E-01	7.80E-02	7.92E-02	-1.66E-01	-1.69E-01	-6.24E-01	-6.16E-01
1.04E+10	1.46E-01	1.43E-01	7.70E-02	7.82E-02	-1.79E-01	-1.83E-01	-6.16E-01	-6.08E-01
1.06E+10	1.47E-01	1.44E-01	7.60E-02	7.72E-02	-1.90E-01	-1.94E-01	-6.08E-01	-6.00E-01
1.08E+10	1.49E-01	1.53E-01	7.50E-02	7.62E-02	-2.01E-01	-2.05E-01	-6.00E-01	-5.92E-01
1.10E+10	1.50E-01	1.55E-01	7.40E-02	7.52E-02	-2.12E-01	-2.16E-01	-5.91E-01	-5.83E-01
1.12E+10	1.51E-01	1.56E-01	7.30E-02	7.23E-02	-2.22E-01	-2.26E-01	-5.83E-01	-5.75E-01

	Real(S12)	Real(S12)	Imag(S12)	Imag(S12)	Real(S22)	Real(S22)	Imag(S22)	Imag(S22)
Freq (Hz)	measured	simulated	measured	simulated	measured	simulated	measured	simulated
1.14E+10	1.52E-01	1.57E-01	7.20E-02	7.13E-02	-2.32E-01	-2.37E-01	-5.75E-01	-5.68E-01
1.16E+10	1.53E-01	1.58E-01	7.10E-02	7.03E-02	-2.42E-01	-2.47E-01	-5.67E-01	-5.60E-01
1.18E+10	1.54E-01	1.59E-01	7.00E-02	6.93E-02	-2.51E-01	-2.56E-01	-5.59E-01	-5.52E-01
1.20E+10	1.56E-01	1.61E-01	6.90E-02	6.83E-02	-2.60E-01	-2.65E-01	-5.51E-01	-5.44E-01
1.22E+10	1.57E-01	1.62E-01	6.80E-02	6.73E-02	-2.68E-01	-2.73E-01	-5.43E-01	-5.36E-01
1.24E+10	1.57E-01	1.62E-01	6.70E-02	6.63E-02	-2.76E-01	-2.82E-01	-5.35E-01	-5.28E-01
1.26E+10	1.58E-01	1.63E-01	6.60E-02	6.53E-02	-2.84E-01	-2.90E-01	-5.27E-01	-5.20E-01
1.28E+10	1.59E-01	1.64E-01	6.50E-02	6.44E-02	-2.92E-01	-2.98E-01	-5.19E-01	-5.30E-01
1.30E+10	1.60E-01	1.65E-01	6.40E-02	6.34E-02	-2.99E-01	-3.05E-01	-5.11E-01	-5.22E-01
1.32E+10	1.61E-01	1.66E-01	6.30E-02	6.24E-02	-3.07E-01	-3.05E-01	-5.03E-01	-5.14E-01
1.34E+10	1.62E-01	1.67E-01	6.20E-02	6.14E-02	-3.13E-01	-3.11E-01	-4.96E-01	-5.06E-01
1.36E+10	1.63E-01	1.68E-01	6.10E-02	6.04E-02	-3.20E-01	-3.18E-01	-4.88E-01	-4.98E-01
1.38E+10	1.63E-01	1.68E-01	6.00E-02	5.94E-02	-3.26E-01	-3.24E-01	-4.81E-01	-4.91E-01
1.40E+10	1.64E-01	1.69E-01	5.90E-02	5.84E-02	-3.33E-01	-3.31E-01	-4.73E-01	-4.83E-01
1.42E+10	1.65E-01	1.70E-01	5.80E-02	5.74E-02	-3.39E-01	-3.37E-01	-4.66E-01	-4.76E-01
1.44E+10	1.65E-01	1.70E-01	5.80E-02	5.74E-02	-3.44E-01	-3.42E-01	-4.59E-01	-4.69E-01
1.46E+10	1.66E-01	1.71E-01	5.70E-02	5.64E-02	-3.50E-01	-3.48E-01	-4.51E-01	-4.60E-01
1.48E+10	1.67E-01	1.72E-01	5.60E-02	5.54E-02	-3.55E-01	-3.53E-01	-4.44E-01	-4.53E-01
1.50E+10	1.67E-01	1.72E-01	5.50E-02	5.45E-02	-3.60E-01	-3.57E-01	-4.37E-01	-4.46E-01
1.52E+10	1.68E-01	1.73E-01	5.40E-02	5.35E-02	-3.65E-01	-3.62E-01	-4.30E-01	-4.39E-01
1.54E+10	1.68E-01	1.73E-01	5.30E-02	5.25E-02	-3.70E-01	-3.67E-01	-4.23E-01	-4.32E-01
1.56E+10	1.69E-01	1.74E-01	5.20E-02	5.15E-02	-3.75E-01	-3.72E-01	-4.16E-01	-4.25E-01
1.58E+10	1.69E-01	1.74E-01	5.20E-02	5.15E-02	-3.79E-01	-3.76E-01	-4.09E-01	-4.18E-01
1.60E+10	1.70E-01	1.75E-01	5.10E-02	5.05E-02	-3.84E-01	-3.81E-01	-4.03E-01	-4.11E-01
1.62E+10	1.70E-01	1.75E-01	5.00E-02	4.95E-02	-3.88E-01	-3.85E-01	-3.96E-01	-4.04E-01
1.64E+10	1.71E-01	1.74E-01	4.90E-02	4.85E-02	-3.92E-01	-3.89E-01	-3.89E-01	-3.97E-01
1.66E+10	1.71E-01	1.74E-01	4.80E-02	4.75E-02	-3.96E-01	-3.93E-01	-3.83E-01	-3.91E-01
1.68E+10	1.71E-01	1.74E-01	4.80E-02	4.75E-02	-4.00E-01	-3.97E-01	-3.76E-01	-3.84E-01
1.70E+10	1.72E-01	1.75E-01	4.70E-02	4.65E-02	-4.04E-01	-4.01E-01	-3.70E-01	-3.78E-01
1.72E+10	1.72E-01	1.75E-01	4.60E-02	4.55E-02	-4.07E-01	-4.04E-01	-3.64E-01	-3.72E-01
1.74E+10	1.73E-01	1.76E-01	4.50E-02	4.46E-02	-4.11E-01	-4.08E-01	-3.57E-01	-3.64E-01
1.76E+10	1.73E-01	1.76E-01	4.50E-02	4.46E-02	-4.14E-01	-4.11E-01	-3.51E-01	-3.58E-01
1.78E+10	1.73E-01	1.76E-01	4.40E-02	4.36E-02	-4.17E-01	-4.14E-01	-3.45E-01	-3.52E-01
1.80E+10	1.74E-01	1.77E-01	4.30E-02	4.26E-02	-4.20E-01	-4.17E-01	-3.39E-01	-3.46E-01